GEOSPATIAL PROCESSING OF

AIRBORNE FULL WAVEFORM LIDAR DATA

A Dissertation

Submitted to the Faculty

of

Purdue University

by

Qinghua Li

In Partial Fulfillment of the

Requirements for the Degree

of

Doctor of Philosophy

December 2018

Purdue University

West Lafayette, Indiana

THE PURDUE UNIVERSITY GRADUATE SCHOOL
STATEMENT OF DISSERTATION APPROVAL

Dr. Jie Shan, Chair

 Lyles School of Civil Engineering

Dr. James S. Bethel

 Lyles School of Civil Engineering

Dr. Melba M. Crawford

 Lyles School of Civil Engineering

Dr. Guofan Shao

 Department of Forestry and Natural Resources

Approved by:

 Dr. Dulcy M. Abraham

  Lyles School of Civil Engineering

To my son,

One beautiful day,

when you find this page,

you will receive the secret gift

that I prepared for you

when you first came into this world.

(Everybody else: shhhhhhh)

ACKNOWLEDGMENTS

This doctoral journey would not have been possible without the encouragement and backing of my family, professors, colleagues, and friends. Now that I am at the end of this journey, I would like to thank all the people who have contributed in different ways to help achieve this accomplishment.

To my family, thank you for being there with your loving, understanding, and patient support. My parents have always given me the very best they could, and today I am especially grateful to them. For all the interest he has shown in my education ever since I was a child, I want to thank my father, Li Xiyuan, and for the unconditional trust and belief she has always had in me, I want to thank my mother, Wang Wenfeng. My lovely and amazing wife, Dr. Wanqing Zhang, has continually provided both the motivation to finish my degree with expediency and the requisite breaks from my research. For this and her ongoing support, I am forever grateful. In addition, my wife and I are both grateful to my mother-in-law, Wu Jing, and my parents for taking such wonderful care of our son.

For his supervision, advice, and guidance, from the very early stages of my research, I would like to express my gratitude to Professor Jie Shan. His own curiosity and zeal for scientific exploration and experimentation has always pushed me and motivated me to do more. His honest feedback and suggestions during our discussions enriched my work in countless ways.

In addition, I am very grateful to the members of my thesis advisory and exam committee: Professors James Bethel, Melba Crawford, and Guofan Shao. They generously gave of their time to offer me valuable comments which improved my thesis.

My sincere thanks must also go to my colleagues and co-authors Dr. Serkan Ural, Yue Li, and Yuchi Ma for our many meaningful discussions and a fruitful collaboration. Special thanks to my CE colleague, ECE classmate, and CRCS officemate

Ke Liu, with whom I shared a very pleasurable working atmosphere and studying experience.

To all the professors, senior members, and student members of Purdue Buddhist Society, I want to express my sincere and humble gratitude. They were always by my side during the happy and hard moments to inspire me and enlighten me.

And what would these last few years be like without all the laughter and good times I have shared with my colleagues, roommates, and friends, who have stayed with us or visited our home. Big thanks to the guys who helped me with yard work, garage work, and home improvement projects.

TABLE OF CONTENTS

Page

LIST OF TABLES

LIST OF FIGURES

ABSTRACT

Qinghua Li Ph.D., Purdue University, December 2018.
GEOSPATIAL PROCESSING OF AIRBORNE FULL WAVEFORM LIDAR DATA.
Major Professor: Jie Shan.

This thesis focuses on the comprehensive and thorough studies on the geospatial processing of airborne (full) waveform lidar data, including waveform modeling, direct georeferencing, and precise georeferencing with self-calibration.

Both parametric and nonparametric approaches of waveform decomposition are studied. The traditional parametric approach assumes that the returned waveforms follow a Gaussian mixture model where each component is a Gaussian. However, many real examples show that the waveform components can be neither Gaussian nor symmetric. To address the problem, this thesis proposes a nonparametric mixture model to represent lidar waveforms without any constraints on the shape of the waveform components. To decompose the waveforms, a fuzzy mean-shift algorithm is then developed. This approach has the following properties: 1) it does not assume that the waveforms follow any parametric or functional distributions; 2) the waveform decomposition is treated as a fuzzy data clustering problem and the number of components is determined during the process of decomposition; 3) neither peak selection nor noise floor filtering prior to the decomposition is needed; and 4) the range measurement is not affected by the process of noise filtering. In addition, the fuzzy mean-shift approach is about three times faster than the conventional expectation-maximization algorithm and tends to lead to fewer artifacts in the resultant digital elevation model.

This thesis also develops a framework and methodology of self-calibration that simultaneously determines the waveform geospatial position and boresight angles.

Besides using the flight trajectory and plane attitude recorded by the onboard GPS receiver and inertial measurement unit, the framework makes use of the publically accessible digital elevation models as control over the study area. Compared to the conventional calibration and georeferencing method, the new development has minimum requirements on ground truth: no extra ground control, no planar objects, and no overlap flight strips are needed. Furthermore, it can also solve the problem of clock synchronization and boresight calibration simultaneously. Through a developed two-stage optimization strategy, the self-calibration approach can resolve both the time synchronization bias and boresight misalignment angles to achieve a stable and correct solution. As a result, a consistency of 0.8662 meter is achieved between the waveform derived digital elevation model and the reference one without systematic trend. Such experiments demonstrate the developed method is a necessary and more economic alternative to the conventional, high demanding georeferencing and calibration approach, especially when no or limited ground control is available.

1. INTRODUCTION

Lidar (Light Detection and Ranging) is a direct 3-D geospatial data collection technique and is extensively used in routine topographic mapping (Shan and Toth, 2018). Lidar systems can be classified into four categories according to the carrying platforms. They are static terrestrial laser scanning (TLS), mobile laser scanning (MLS), airborne laser scanning (ALS), and spaceborne laser scanning (SLS) (Popescu et al., 2011; Bye et al., 2017). Lidar systems can also be classified in other ways: from the temporal behavior of the laser signal, it can be classified as pulse lidar and continuous lidar; from the aspect of operation mode, it can be classified as Geiger mode, single-photon lidar, or linear lidar; from the aspect of the laser beam divergence, it can be classified as small-footprint and large-footprint lidar; from the aspect of digitizer format, it can be classified as discrete and full waveform lidar, etc.

Exploring information with higher accuracy and higher resolution has been the main effort of lidar industries and academic societies. On one hand, software engineers and academic researchers have been working on the algorithms for lidar data processing: lidar waveform decomposition (Hofton et al., 2000; Mallet et al., 2010), filtering and classification (Reitberger et al., 2009; Meng, et al., 2010; Hovi et al., 2016), DEM generation (Liu, 2008), etc. On the other hand, recent advanced development on the hardware leads to new lidar systems: full waveform lidar, Geiger-mode lidar (Stoker, 2016), single-photon lidar (Li et al., 2016), adaptive lidar, etc. The focus of this thesis is to develop geoprocessing algorithms and methodology that can take advantage of the new features of modern lidar systems for scientific and engineering applications.

1.1 Research Context

1.1.1 Full Waveform Lidar

Among the advanced lidar systems, the most noticeable common technique is the full waveform lidar (Mallet and Bretar, 2009; Pirotti, 2011). The system is named full waveform lidar as contrary to the discrete lidar system (Sumnall, et al., 2016). The difference between the discrete lidar and the waveform lidar can be seen in Fig. 1.1. In Fig. 1.1(a), the time that the laser light is emitted is recorded by a discrete time t_{in}; similarly, the time that the laser light is returned will be recorded by a discrete time t_{out}. The difference between the two times will be utilized to calculate the range between the lidar platform and the target. In practice, however, the emitted signal is realized by a continuous wave with duration from a few picoseconds to several nanoseconds. Instead of recording the discrete emitted/returned time, a full waveform lidar system samples and records the entire backscattered signal at a temporal resolution of nanoseconds or sub-nanoseconds. The recorded signal, referred to as a (returned) waveform, consists of a series of temporal waves, with or without overlap, where each corresponds to an individual reflection from an object (Wang, et al., 2015). Some system even provides the whole emitted signal at the same temporal resolution. Example of an emitted signal from a full waveform recorder is shown in Fig. 1.1(b).

Besides the sampled waveforms, the full waveform lidar data also provides a series of systematic parameters. In the airborne full waveform lidar system, such information includes: (1) the start time of each waveform; (2) the temporal trajectory and orientation of the airplane; (3) the temporal position and orientation of the sensors. They are collected by the laser scanner and GPS/INS system aboard. A lidar point cloud or other relative lidar product can be obtained by integrating and processing all these measured data. In most cases, working with the full waveform lidar data needs more effort than directly working on the lidar point cloud.

(a) The emitted time recorded by discrete lidar.

(b) The emitted signal recorded by full waveform lidar.
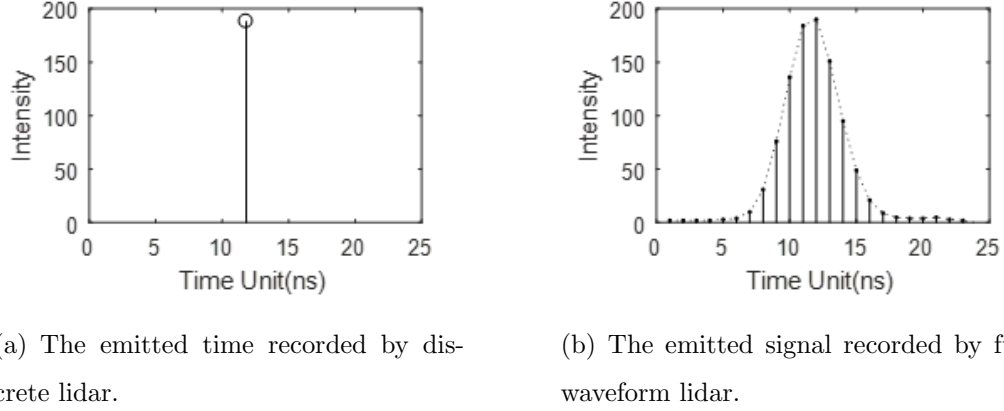
Fig. 1.1. The emitted lidar signals.

The existence and extent of the advantages of the full waveform lidar is a frequently discussed topic (Anderson et al., 2016; Sumnall, et al., 2016). Such discussion exists because the prototype of waveform processing is not standardized. It is also because that most existing methods may not take full advantages of the full waveform data. To date, the full waveform lidar is mainly applied in forestry and natural resources related fields (Bretar et al., 2008; Mücke et al., 2013; Hancock et al., 2015). For example, the features of waveforms have the potential to estimate ecological and environmental parameters. The usefulness of full waveform in general scenarios is rarely mentioned (Tran et al., 2015). At the same time, the cost of the full waveform lidar system is higher than the traditional discrete lidar. Taking these factors into consideration, it may be intuitive to choose a discrete lidar system if the study area is free of canopy coverage or the ecological parameters are of no interest. As a result, the potentials of the full waveform lidar are far from being exploited.

Can we use the full waveform data to improve the quality of a general lidar product? Will the waveform data output a point cloud that matches the ground truth better? Can we use the waveform data to improve the efficiency of topographic investigation? These are the questions we would like to discuss in this dissertation. Specifically, this thesis focuses on the comprehensive and thorough study of the airborne full waveform lidar data. We intend to answer these questions by exploring the

main steps of the airborne full waveform data processing, namely, waveform decomposition, georeferencing and calibration.

1.1.2 Waveform Decomposition

The range between the sensor and the target is derived from a procedure called waveform decomposition. As the name suggests, it decomposes the original waveform to one or a few waveform components. Each of the significant components corresponds to a point in the point clouds.

Waveform decomposition plays a very important role in generating high quality lidar products (Parrish et al., 2011). Researchers proposed many different approaches to deal with the problem. Most of them assume the waveform is generated from a parametric function and design algorithms to solve the parameters of the function. A Gaussian mixture model (GMM) is used in this part of the work, and a minimum description constrained EM (Expectation-Maximization) algorithm is proposed to decompose the waveforms. We will study this topic in Chapter 4.

We also propose a nonparametric approach to model and decompose the waveforms. One of the main features of this approach is that the limitation of parametric functions is removed. We will introduce a nonparametric mixture model (NMM) and a fuzzy mean-shift (FMS) algorithm. The results and the performance of both approaches will be compared in Chapter 5.

1.1.3 Georeferencing and Calibration

People can calibrate the lidar system before or after the data is collected. Conventionally, the manufacturer or data provider will pre-calibrate the systematic parameters prior to data collection. The pre-calibration needs hardware, on-site measurement and ground truth (Skaloud and Lichti, 2006). The cost of such calibration is usually very high, so it is difficult to routinely re-conduct after the first calibration. Fur-

thermore, results from lab calibration may considerably vary during flight. As such in-flight or post-calibration is necessary.

On the other hand, researchers developed algorithms to calibrate the system after the point cloud data is delivered (Pfeifer et al., 2005). Post-calibration is desired because the quality of the data may be significantly improved through this process. However, the conventional calibration has a few limitations. For example, multiple strips of lidar points acquired from the same platform are needed to conduct the point cloud-based calibration. It becomes challenging when no exact correspondence for ground control points exists.

This thesis discusses the possibility of calibrating systematic parameters with full waveform lidar data. It models the calibration as an optimization problem that minimizes the difference between the lidar-generated DEM and a reference DEM. Working with DEM relieves the need of ground control points and multiple strips. Plus, it can be routinely re-conducted. In the experiments, both particle swarm optimization and convex optimization are used in solving the problem.

1.2   Related Works

Many algorithms are proposed to decompose full waveform lidar data. They can be classified into three categories: peak/edge detection (Bretar et al., 2008; Wagner et al., 2007), deconvolution (Wu et al., 2011; Azadbakht et al., 2016; Shen et al., 2017; Zhou et al., 2017), least-square optimization (Hofton et al., 2011; Xu et al., 2016; Wang et al., 2017; Zhao et al., 2018) and statistical method (Hernandez-Marin et al., 2007; Zhou and Popescu, 2017).

The peak/edge detection method is the simplest and fastest algorithm for waveform decomposition. It is attractive because the waveform components can simply be detected by applying a threshold. However, peak/edge detection method does not take mixture into consideration. As a result, it sacrifices the high accuracy and fidelity which come with advanced lidar systems.

Deconvolution methods improve the accuracy, but they are sensitive to the noise level (Li et al., 2014). Some deconvolution methods require the system impulse response to be known (Wu et al., 2011), which is often not provided by the data vendors.

Statistical method models lidar waveforms as the histogram of samples of a random variable (Parrish et al., 2014) so that many clustering algorithms can be applied to classify those samples. In the statistical approaches, a Gaussian mixture model (GMM) and corresponding algorithms are among the most popular waveform decomposition methods (Parrish and Nowak, 2009; Wagner et al., 2006; Jung and Crawford, 2008; Wang, 2012; Wang et al., 2013; Qin et al., 2015). They are supposed to be more accurate since they consider the mixture of waveform components. However, the Gaussian mixture model is unable to precisely model non-Gaussian waveform components, especially asymmetric waveform components that have been frequently reported by researchers.

GMM can also be solved by Levenberg-Marquardt algorithm (Hofton et al., 2000; Xu et al., 2016; Zhao et al., 2018), a nonlinear least-square method. The main challenge of such nonlinear optimization approach is its convergence being sensitive to the initial values of the unknown parameters.

Some other works consider modeling the waveforms with more complex distributions (Hernandez-Marin, et al., 2007; Mallet et al., 2010). They build a library of models and choose the most suitable ones with Bayesian analysis. However, their effectiveness is constrained by the creation of a comprehensive model library and the complexity in selecting one or more best models for a specific application. As a result, such methods are not practical to handle large volume of lidar data and meet the need of diverse applications.

1.3   Structure of the Thesis

The rest of this thesis is organized in the following way. Chapter 2 introduces the basic concepts of laser scanners and the data structure that is used in our research.

Chapter 3 introduces the theoretical framework of processing full waveform data. Chapter 4 discusses the parametric waveform decomposition algorithms. Chapter 5 proposes a nonparametric waveform decomposition approach. Chapter 6 studies georeferencing and a self-calibration method. In the end, the work will be summarized in Chapter 7.

2. AIRBORNE LIDAR SYSTEMS

An isolated lidar cannot obtain valid surveying results. We use the phrase "lidar system" to describe the set of functional units during lidar surveying. A typical airborne lidar system includes:

- Lidar;

- Position and orientation system (POS) that usually contains an onboard INS (Inertial Navigation System), an airborne GPS, and ground GPS reference stations;

- Airborne platform that carries the onboard instruments.

Correspondingly, the full waveform lidar data of the airborne lidar systems includes the following independently collected and sampled datasets: (1) the time-tagged, digitized waveforms, (2) the coordinate and direction of the sensor in the lidar coordinate system, and (3) the temporal trajectory and orientation of the airplane.

This chapter will briefly introduce each component of an airborne lidar system. The system used in this thesis will be introduced at the end of the chapter.

2.1 Laser Scanner

The ranging unit of a lidar system is a laser scanner (LS), or a laser rangefinder (LRF). It is a major component in the entire lidar system. It emits a light signal, illuminates the target and measures the slant range between the target and the sensor. As a matter of fact, this is where the name "lidar", light detecting and ranging, comes from.

2.1.1 Laser in Lidar Systems

A laser is a device that emits light through a process of optical amplification based on the stimulated emission of electromagnetic radiation. In general, the input of a laser could be either electrical or optical. For lidar sensors, the power source is electrical power. The output of the laser could be a continuous wave (CW) or a pulse wave. The continuous-wave lasers produce a continuous, uninterrupted beam of light. They can be utilized to determine the range with the phase shift of the signal. Higher resolution can be obtained with continuous-wave lasers. However, such systems suffer the limitation of high power consumption and phase ambiguity; thus, they are used more in terrestrial lidar sensors. A pulsed laser sensor produces laser pulses with a limited time duration. High energy can be realized in short intervals (Wehr and Lohl, 1999), which is desirable for far range surveying. Hence, most airborne lidar systems fall in the category of pulse wave.

The pulsed lasers are mainly generated from two different optics cavities: a mode locked cavity and a Q-switched cavity (Milonni and Eberly, 2010), where "Q" means the Q factor, or quality factor, which is a dimensionless parameter that characterizes a resonator's bandwidth relative to its center frequency. The mode locked cavity has an extremely high Q factor, and it can produce an ultrafast laser with the duration of 5fs to 100ps. On the other hand, the Q-switched cavity can increase its Q factor rapidly by actively or passively reducing the losses of the cavity. Its pulses bandwidth has a range from 0.5 to 500 nanoseconds. Compared to mode-locked lasers, Q-switched laser have lower pulse repetition rate, higher pulse energy, and longer pulse duration, so it is widely utilized in the airborne lidar systems. (https://ocw.mit.edu/courses/electrical-engineering-and-computer-science/6-977-ultrafast-optics-spring-2005/lecture-notes/)

From publically accessible sources, many airborne lidar systems applied the Q-switched laser pulses. Examples are NASA's research laser scanners in Laser Vegetation Imaging Sensor (LVIS), Geoscience Laser Altimeter System (GLAS), Shuttle Laser Altimeter (SLA), Scanning Lidar Imager of Canopies by Echo Recovery

(SLICER), and Raster Scanning Airborne Laser (RASCAL). It also includes the experimental laser scanner developed by Bridger Photonics.
(https://sbir.nasa.gov/SBIR/abstracts/16/sbir/phase2/SBIR-16-2-S1.01-7662.html)

2.1.2   Emitted Signals

A typical pulse from actively and passively Q-switched laser is plotted in Fig. 2.1(a) and (b) (https://www.rp-photonics.com/q_switching.html on 9/19/2018). The left part of the peak value is proportional to the net gain after the Q factor of the cavity is switched to a high value and the right part mostly depends on the cavity decay time. Since the arising time and the decreasing time depend on different characteristics of the cavity, the shape of the pulse may or may not be symmetric.

Although the main commercial lidar system manufacturers, such as Riegl, Optech, and Leica, do not provide technical details about their products, the digitized emitted signal and/or the returned waveform are available in the delivered raw data (Pirottia, et al., 2012). Fig. 2.2. shows an emitted signal of Riegl Q680i. It shares the same characteristics as the Q-switched laser signals: first, the duration time is around 10-20 nanoseconds; second, the emitted signal is asymmetric. These features will be further addressed in the chapters of waveform decomposition.

2.2   Positioning and Orientation Systems (POS)

The positioning and orientation systems (POS) use positioning technology (GPS, GNSS) and INS to determine the position and orientation of the aircraft that carries the laser scanner. The ground reference GPS, onboard GPS/GNSS and INS are the main components of POS.

The ground GPS stations provide references to the GPS measurement of the airborne platform. They are usually required to be located within 25km of the flight line (Shan and Toth, 2018). During flight mission, the ground stations collect GPS carrier phases at known positions. At the same time, the onboard POS records the
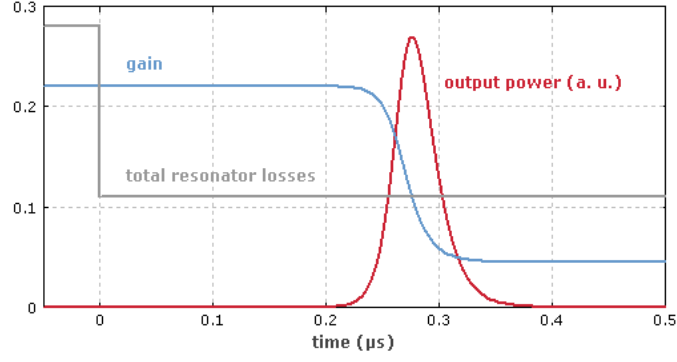
(a)
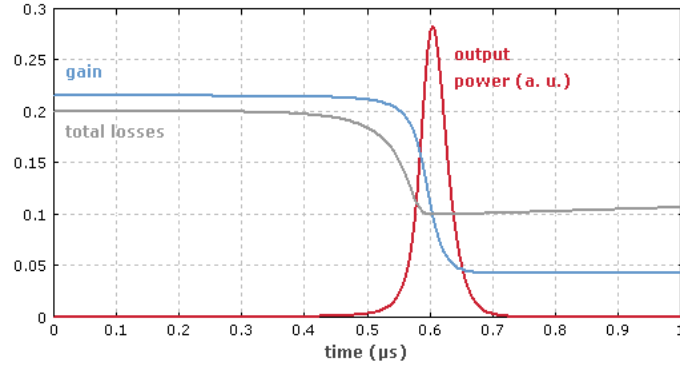
(b)

Fig. 2.1. The pulse shape of an (a) active (b) passive Q-switched laser.

GPS carrier phases and the INS orientation data on the airborne platform. With differential GPS (DGPS), the trajectory of the airborne platform can be obtained with centimeter to decimeter accuracy.

Each of the on-board instruments (GPS antenna, IMU box, and the lidar scanner) has its own coordinate system and its own sampling rate. The measurements are transformed to one common coordinate system and aligned with the same time interval. Temporally, the data with low sampling rate is usually interpolated before being aligned to the data with high sampling rate. Spatially, the relative distances between the GPS, IMU, and laser scanner should be measured. These distances are called lever arms and the user must input them into the POS processing software (Shan and Toth, 2018).
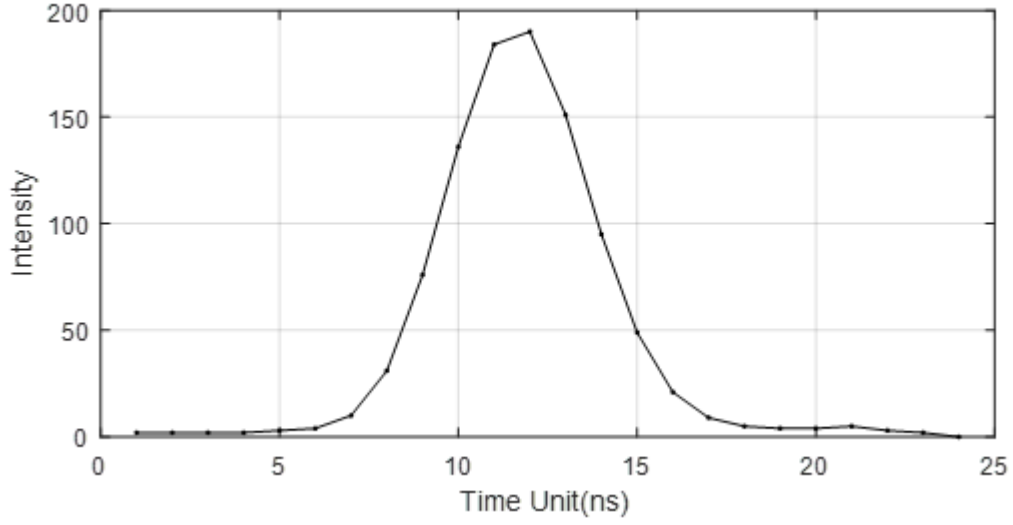
Fig. 2.2. An emitted signal of Riegl waveform lidar scanner.

After the POS data is interpolated, time-registered, and transformed, the coordinates of the target can be determined by incorporating all the measurements from the lidar system:

1. the sampled position and orientation of the platform, which is obtained by POS;

2. the sampled pointing direction of the sensor, which is directly measured by laser scanner;

3. the range between the laser scanner and the target, which is measured by the laser scanner and derived from waveform decomposition algorithms.

2.3 Airborne Platform

The flight platform of the airborne lidar system is the aircraft that carries all the on-board components. Flight altitude and speed should be determined according to the specification of the mission.

2.3.1 Flight Height and Multiple-Time-Around (MTA)

The flight height is one of the important factors that control the acquisition range and point density along the scan direction. Increasing the flight height will expand the scan range but the accuracy will be degraded. More importantly, the multiple-time-around (MTA) will appear when the slant range is higher than $c/(2 \cdot prr)$, where c is the speed of light and prr pulse repetition rate of the laser scanner.

MTA occurs because the emitted signals and the returned waveforms are not registered. A second-time-around return can be received after a time delay exceeding one pulse repetition interval but less than two pulse repetition intervals. Similarly, a third- or a fourth-time-around return may happen, too. MTA will inevitably introduce the problem of range ambiguity (Rieger, 2014; Sitar, 2015). Without appropriate processing, some ranges of the lidar points can be miscalculated. In such cases, a ghost patch may appear either high in the sky or far beneath the ground, as is shown in Fig. 2.3.

In Fig. 2.3., the laser signals are emitted with a constant time interval after the initialization stage ($t <$2675.059192 sec). Due to the high pulse repetition rate of the system, the returned waveform may not be associated to the closest emitted signal ahead of it. An effort for matching the return waveform to the corresponding emitted signal is required for the correct calculation of ranges and point locations.

2.3.2 Aircraft Speed and Ground Point Density

Aircraft speed affects the point density along the flight direction. It is usually desired that the points can be evenly distributed in directions both parallel and perpendicular to the flight lines. After the point density on the scan line is determined by the flight height and the pulse repetition rate of the scanner, the flight speed can then be determined.
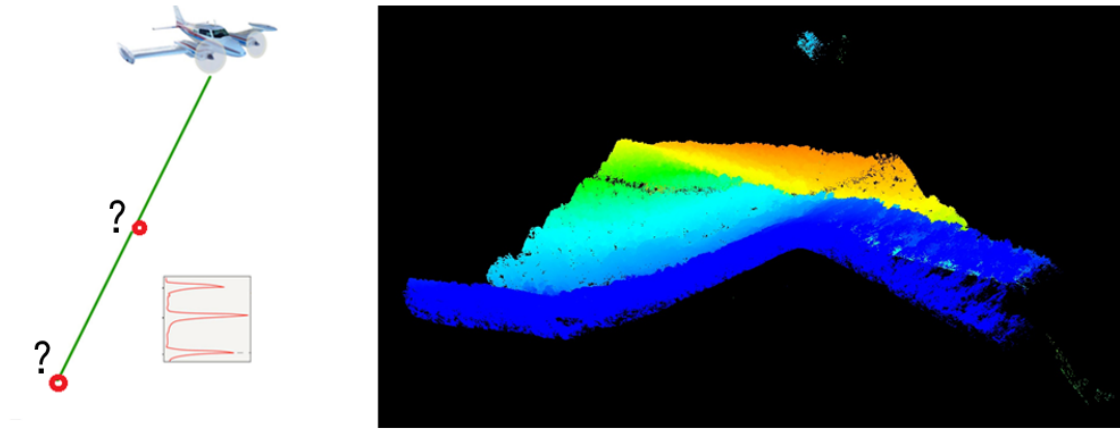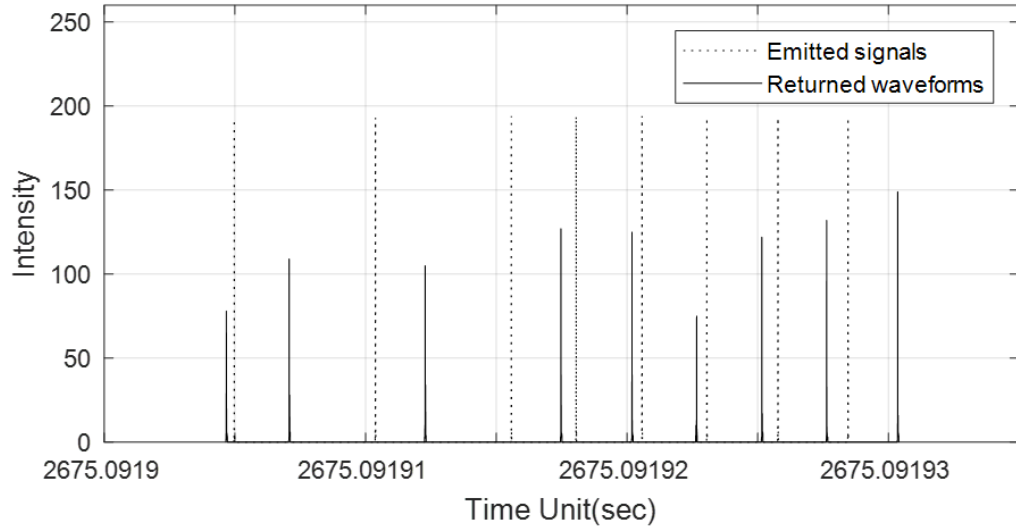
Fig. 2.3. An example of miscalculated point locations due to MTA.

2.4   An Example System

The main algorithms and methodologies developed in this thesis will be tested by the full waveform lidar data collected by the airborne lidar system with the laser scanner of Riegl Q680i.

2.4.1 Characteristics of the Laser Scanner

The photo of the sensor and one of the emitted signals are shown in Fig. 2.4(a) and (b), respectively. From Fig. 2.4(b), the signal is right skewed. Its duration is around 10 nanoseconds.

(a)   (b)
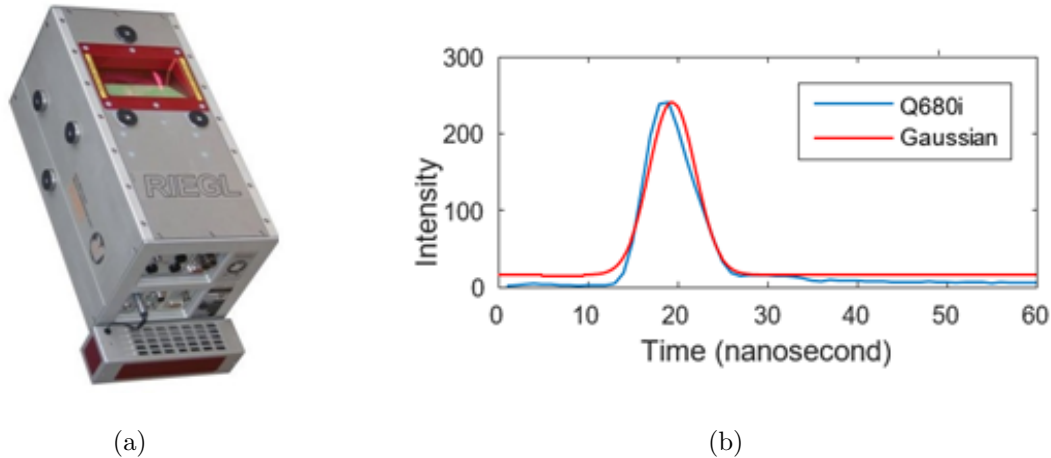
Fig. 2.4. (a)Riegl Q680i; (b)An emitted pulse of Riegl Q680i.

The specifications that are released by Riegl are listed in Table 2.1. Among them, the accuracy is defined as the degree of conformity of a measured quantity to its actual (true) value, and precision is the degree to which further measurements show the same result (Datasheet of Riegl Q680i).

2.4.2 Data Structure of the Laser Scanner

In the experiment, the waveform data contains approximately 50,000,000 recorded waveforms and is about 8 GB in size. The full waveform binary file is accessible via the RiWaveLib C++ waveform extraction library provided by Riegl as an interface to extract information from the waveform data. One record of the full waveform lidar data mainly consists of the following information:

1. index information such as record number, internal time, and external time.
2. spatial information such as the vector of sensor origin and sensor orientation.

Table 2.1.
Specifications of the Riegl Q680i

Parameter	Value
Laser Beam Divergence	≤ 0.5 mrad
Scan Angle Range	$\pm 30° = 60°$ total
Angular Step Width	$\geq 0.002°(0.03°$ in our data)
Pulse Repetition Rate (PRR)	80/200/300/400kHz
Maximum Operating Flight Altitude	800m@400kHz PRR
Time Interval of Sampling	10^{-9} second
Accuracy	20mm
Precision (reproducibility, repeatability)	20mm

3. reference time or the sampled emitted signal.

4. the sampled returned waveform.

The structure of a record is listed in Table 2.2. A specific waveform dataset consists of all sample blocks of the waveforms detected by the receiver and additional information, e.g., the beam direction. Both the emitted signals and the returned waveforms (not necessarily corresponds to the emitted signal in the same block) are sampled and recorded. A time stamp for the start of each sample block is recorded, which allows to determine the time of all samples in the same sample block using the sample interval.

2.4.3 Platform Trajectory

The GPS and IMU measurements are integrated in a binary SBET (Smoothed Best Estimate of Trajectory) file in .out format. The file contains a 136 byte standard navigation record, which stores the trajectory and flight dynamics of the airplane: the time, position, speed, orientation, platform heading, etc. We access this binary file by

Table 2.2.
Data structure of Riegl Q680i

Name	Type	Length
Record index	Int	1
Internal time	Float	1
External time	Float	1
Vector of sensor origin	float	3
Vector of sensor direction	float	3
# of samples of emitted pulse	int	24
# of samples of the returned waveform	int	60, 120 or 240

using the *IceBridge Applanix SBET file Perl reader* provided by the National Snow and Ice Data Center (NSIDC).

The lidar data was collected in a forest area of Shenandoah National Park, VA, USA. The flight trajectory of the sensor platform together with its location is extracted from the .out file and is plotted in Fig. 2.6. In the figure, the black lines are the trajectory of the airplane and the single orange line in the middle highlights the section where the lidar sensor collected the data. The part of the trajectory file that corresponds to the acquisition of this laser scan dataset consists of approximately 45,000 trajectory points and other related records, e.g., speed and orientation of the platform for each trajectory point.

2.4.4   Ground Density of the Waveforms

The altitude and the speed of the airplane should be carefully designed to match the pulse repetition rate of the laser scanner and generate an evenly distributed point cloud with a desired point density.
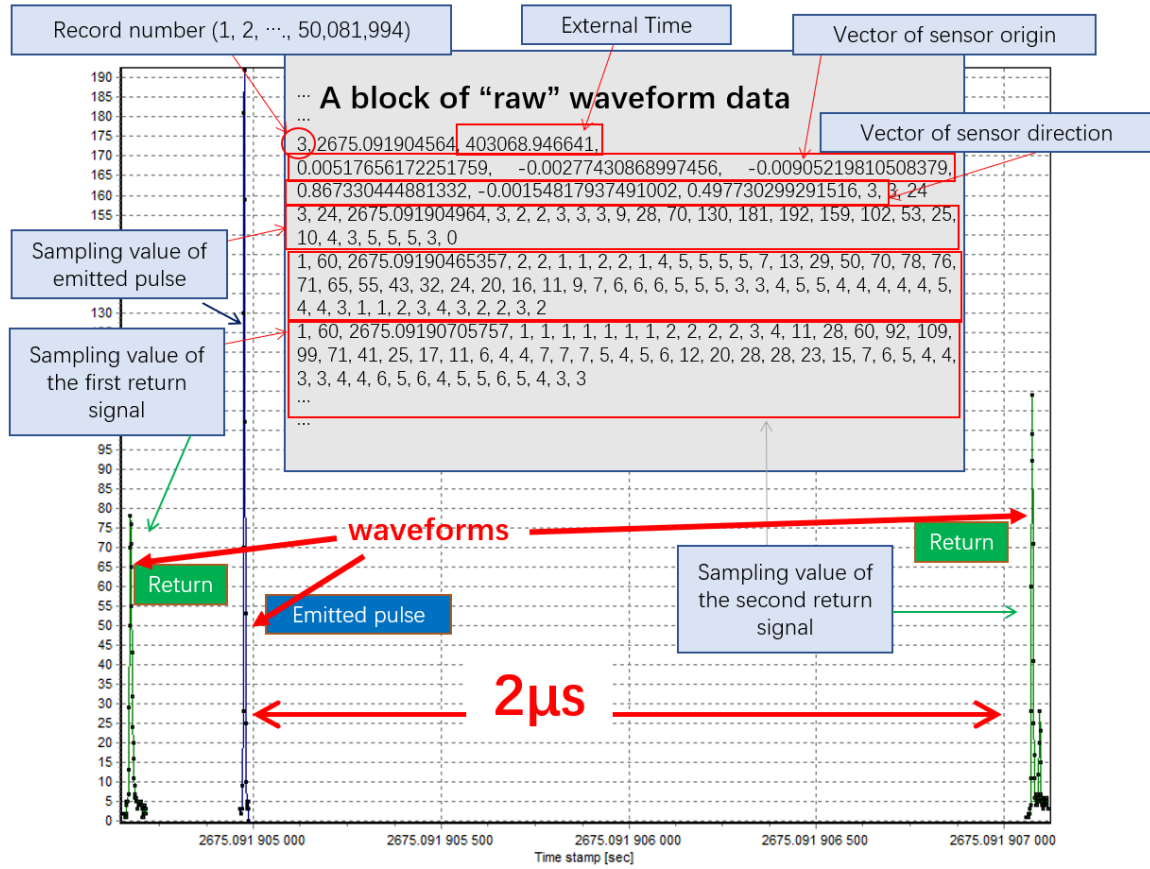
Fig. 2.5. An example of data structure of Riegl Q680i.

The laser scanner works with a pulse repetition rate of 400kHz. This can also be verified from the fact that there are around 1,570 emitted pulses per scan line. The line repetition rate is then 255 lines per second. The speed of the aircraft is around 80 meters per second, which leads to the scan line density of 400k/1570/80=3.2 lines per meter.

The flight height above ground is about 500 meters and the scan angle is 60 degrees. The point density along the scan line is approximately $1570/60/500/\sin(1°)$ = 3.0 points per meter.

The point distribution can be examined from a section of ground points as is shown in Fig. 2.7. In the figure, one 3×3 m^2 ground square and two 1×1 m^2 ground
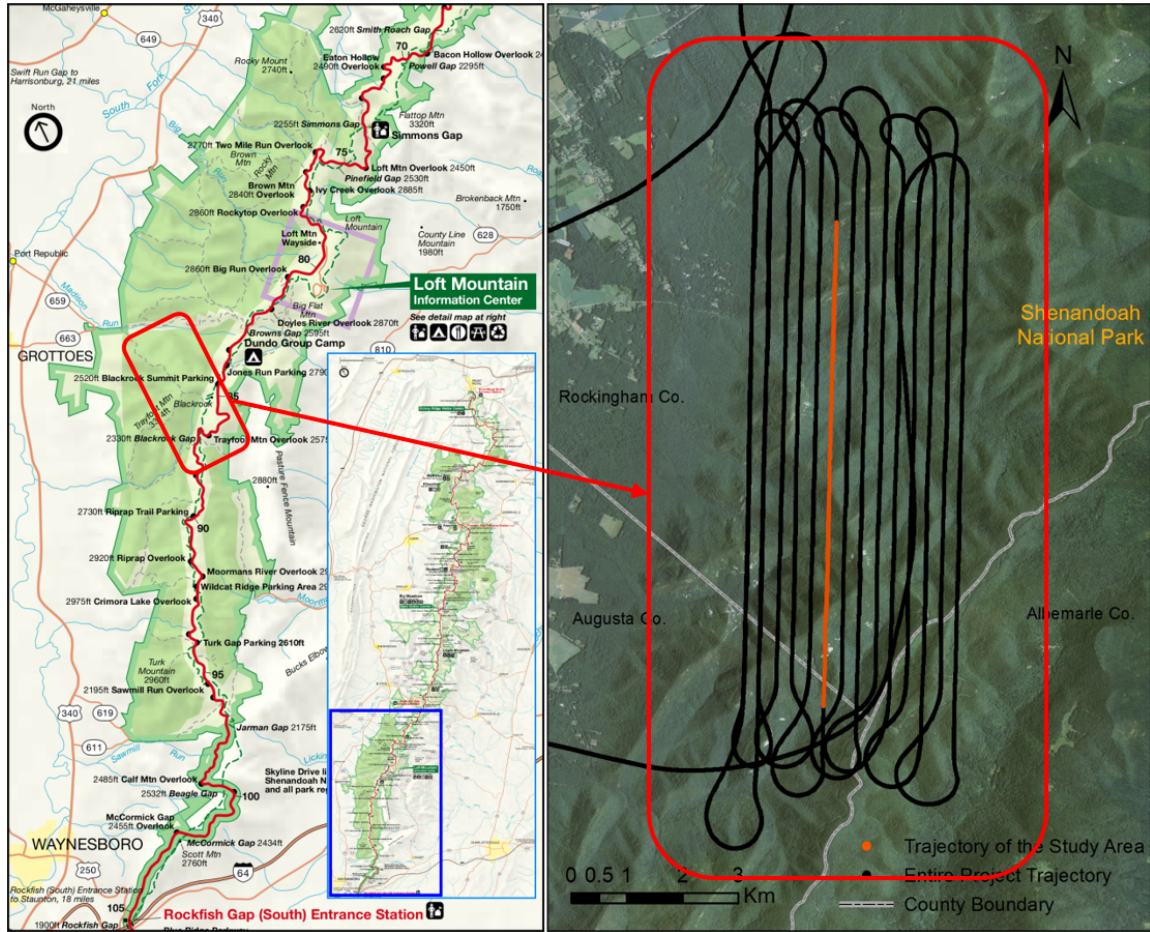
Fig. 2.6. Flight trajectory over the Shenandoah National Park. (Left) The park map (http://www.nps.gov/shen/planyourvisit/maps.htm by National Park Services) and (Right) flight trajectory of the sensor platform over the study area.

squares are highlighted in red. It can be observed that the ground point density is around 10 points per square meter. Furthermore, the points can be regarded as evenly distributed along the scan line and the flight direction.
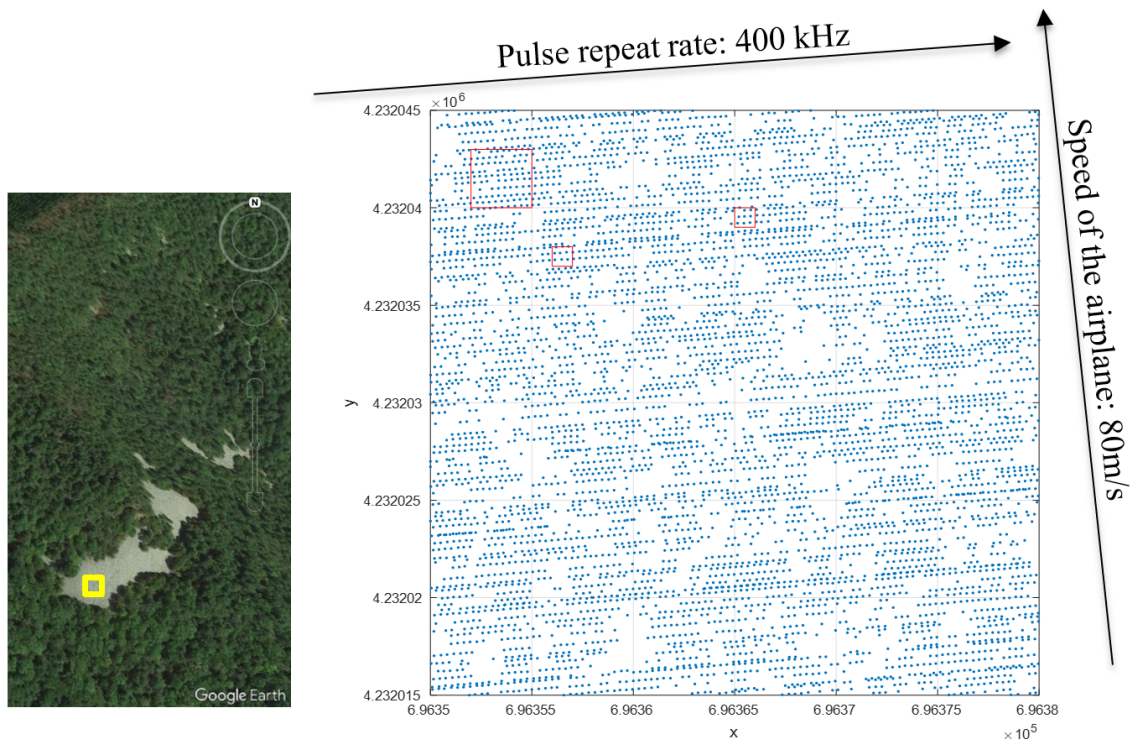
Fig. 2.7. Ground point distribution of the example lidar system.

3. THEORETICAL FRAMEWORK

The raw digitized lidar waveform and the position and orientation of the aircraft should be processed and integrated to output final lidar products such as point cloud and digital elevation model (DEM). Waveform decomposition, georeferencing and calibration are the common steps of processing the waveform data. During waveform decomposition, the algorithm determines the accuracy of the range measurement between the lidar scanner and the detected object. During georeferencing, the calibration results determine the estimated position of the target. Developing or choosing an appropriate method in each step is crucial to the quality of the final product. Accuracy, cost, efficiency, repeatability, and complexity are the factors to be considered in designing a processing protocol.

Depending on the specific applications, the exact steps of geospatial processing of airborne waveform lidar data may be different case by case. Generally, they include the following steps:

- Waveform decomposition. This step deals with the recorded waveform acquired by the laser scanner. Each waveform will be decomposed into one or several components, each of which in turn corresponds to a detected target. These waveform components can be used to determine the ranges between the laser scanner and the targets.

- Direct georeferencing. The purpose of georeferencing is to calculate the coordinates in the mapping frame of all the range measurements from the laser scanner. The GPS/INS measurements together with the orientation measurements recorded by the laser scanner will be integrated in this step. During the process, either the laser scanner and the INS unit are assumed to be perfectly aligned, or the relative position and orientation of the components are given.

- Calibration. The angular displacement between the laser scanner and the IMU unit exists, and it is difficult to determine from direct measurements in the lab. Such angular displacement, usually referred to as boresight misalignment or boresight angle, is estimated in a calibration process. In many cases, a specially designed flight plan will be conducted to estimate the boresight angles. Such flight is called boresight flight. Usually, the one-time boresight flight is conducted before the data acquisition.

- Classification of lidar point cloud. Classification is a conventional technique in analyzing the digitized lidar data. This step is also included in the full waveform lidar processing because many calibration schemes use specific building points. In our work, the study area is a forest area where buildings or similar control points are absent. In such case, the ground points that are obtained by ground filtering will be used for calibration.

In this chapter, the methodology of each main step will be discussed. The framework of our work will be summarized at the end of this chapter.

3.1 Waveform Modeling and Decomposition

Waveform modeling and decomposition are the common steps for exploitation of full waveform lidar data. There are several alternative approaches to detect and estimate the characteristics of each return from the digitized waveform signal. Examples are peak detection, leading edge detection, constant fraction detection, center of gravity detection, deconvolution, etc. (Shan and Toth, 2018)

3.1.1 Peak Detection

An effective waveform decomposition needs both simplicity and accuracy. The simplest and most widely adopted decomposition method is peak detection (Bretar, et al., 2008; Wagner, et al., 2007). It is attractive because the waveform components

can simply be detected by applying a threshold. It has the desired high efficiency for coping with large volumes of lidar data but does not take mixtures into consideration. As a result, it sacrifices the intrinsic high accuracy and fidelity of advanced lidar systems in exchange for such simplicity.

3.1.2   Parametric Waveform Decomposition

Parametric waveform decomposition first models the returned waveform as a mixture function of several parametric components. Different functions, including Gaussian, generalized Gaussian, lognormal, Weibull, Nakagami, Burr, have been proposed to model lidar waveforms (Mallet, et al., 2010; Słota, 2014). Among them, the Gaussian Mixture Model (GMM) has prevailed for many years and is widely adopted (Parrish and Nowak, 2009; Hofton et al., 2000; Wagner et al., 2006; Jung and Crawford, 2008; Wang, 2012; Wang et al., 2013). It models the returned waveform $y(t)$ as a weighted sum of several Gaussian components,

$$y(t) = \sum_{j=1}^{J} y_j(t) = \sum_{j=1}^{J} w_j \cdot \exp[-\frac{(t - \mu_j)^2}{2\sigma_j^2}] \tag{3.1}$$

where t is the sampling time, y the intensity of the waveform, $(\mu_j,\ \sigma_j)$ the mean and the standard deviation of the j-th Gaussian component, and J the total number of Gaussian components. Both J and $\theta = [\mu_1, \sigma_1, w_1, \mu_2, \sigma_2, w_2, \ldots, \mu_J, \sigma_J, w_J]$ are parameters to be estimated.

Many algorithms were proposed to decompose the waveform data based on GMM. For example, Hofton et al. (2000) used the Levenberg-Marquardt optimization algorithm. The main challenge of such a nonlinear optimization approach is its convergence being sensitive to the initial values of the unknown parameters. Another widely used and cited approach is the Expectation-Maximization (EM) method (Dempster, et al, 1977; Jung and Crawford, 2008; Pan, et al., 2015). In both approaches, the number of waveform components needs to be predefined and may vary from waveform

to waveform. To cope with this problem, we will introduce a minimum description length (MDL) constrained waveform decomposition in the next chapter.

3.1.3 Nonparametric Waveform Decomposition

In the framework of a nonparametric mixture model, lidar waveform is the sum of data clusters. Each cluster is composed of a collection of data samples x_n:

$$y\left(t\right) = \sum_{j=1}^{J} y_j\left(t\right) = \sum_{j=1}^{J} \left[\frac{1}{N_j \times h} \sum_{n_j=1}^{N_j} w_{n_j} \cdot k \left(\frac{t - x_{n_j}}{h} \right) \right] \tag{3.2}$$

where $k(\cdot)$ is a kernel function of the model and h is the bandwidth (Fukunaga and Hostetler, 1975).

The nonparametric clustering problem is solvable with a fuzzy mean-shift algorithm, where it determines the modes in the data and clusters all the data samples accordingly. The implementation details of FMS will be introduced in Chapter 5.

3.2 Range Determination

3.2.1 Range Calculation

Once the decomposition is complete, the range between the target and the sensor is calculated by using the time the laser signal takes to travel to and from the target and the speed of light

$$\rho = \frac{c}{2}\left(t_{in} - t_{out}\right) \tag{3.3}$$

where ρ the range between the sensor and the target, and c the speed of light. t_{out} and t_{in} are the time that the signal is emitted and returned from the target, both of which can be determined from the result of waveform decomposition. For EM approach, the mean value of the Gaussian component of the emitted signal corresponds to t_{out}, and the mean value of each Gaussian component in the returned waveform is $t_i n$.

For FMS, we can take the peak or the mass center of each waveform component to determine its time. The mass center is calculated by

$$t_{in} = \frac{\sum_{n=1}^{N_j} w_n \cdot x_n}{\sum_{n=1}^{N_j} w_n} \tag{3.4}$$

Similarly, for the corresponding emitted signal, its outgoing time by mass center is

$$t_{out} = \frac{\sum_{n=1}^{N_{out}} z_n}{N_{out}} \tag{3.5}$$

where z_n is defined the same way as we define x_n except that z_n is for the emitted signal. N_j and N_{out} are respectively the number of samples within the j-th waveform component and the emitted signal.

3.2.2 Solution to Range Ambiguity

In cases where both high repetition rate and high flight height are desired, and where MTA exists, the range ambiguity should be solved either by the software toolkit provided by the manufacturer or by some specially designed algorithms (Krichel, et al., 2010; Rieger and Ullrich, 2011; Rieger, 2014).

In our work, the very first scan strip was visually examined and adjusted to allow the unambiguous calculation of the first measurement range. Based on this initial value, each further consecutively received waveform will be associated to the emitted signal with the least difference in distance between successive range measurements. The ranges that are already resolved in the previous scan line become the new initial values for the allocation of ranges of the subsequent scan line. The iteration continues until all the returned waveforms are associated with an appropriate MTA zone.

3.3 Direct Georeferencing

The GPS, INS, and the laser scanner all have their respective coordinate frames, as is shown in Fig. 3.1. Calculating the coordinates of the target points in the mapping

coordinate system using the calculated ranges, beam direction, and the trajectory information requires dealing with different coordinate systems of the involved components. This process is commonly referred as direct georeferencing, where GPS/IMU provides the necessary position and orientation information and no additional ground control is needed. Often it is the first step towards final, precise georeferencing (Shan and Toth, 2018).

The direct georeferencing process has the following main steps. The first step is to determine the ranges between the laser scanner and the targets. The second step is to calculate coordinates of the targets in the sensor's (laser scanner's) frame. The third step is to incorporate the data collected by ground GPS, onboard GPS and INS component, and to generate a trajectory file that includes the GPS time, the position and orientation of the aircraft. These three steps are independent, so they can be separately conducted with a customer-designed algorithm or a given software package. However, the results are in their own coordinates: the lidar data is in a sensor frame, the GPS data in the mapping frame, and the IMU data in the airplane frame.

The final step of direct georeferencing is to incorporate all the results from previous stages and to output the point cloud in the mapping frame. A series of coordinate conversions are required in this step.

3.3.1   Point Coordinate Calculation in the Scanner Frame

The scanner frame is the airborne laser scanner's own coordinate system (SOCS). Let $\boldsymbol{o}^S(t_S)$ be the position vector of the laser scanner at the instant t_S, $\boldsymbol{d}^S(t_S)$ the direction of the laser beam. As is shown in Fig. 3.1., the target location $\mathbf{r}^S_{target}(t_S)$ is calculated in the lidar frame by

$$\boldsymbol{r}^S_{target}(t_S) = \boldsymbol{o}^S(t_S) + \boldsymbol{d}^S(t_S) \cdot \rho(t_S) \qquad (3.6)$$

where $\rho(t_S)$ is the frame-independent range between the sensor and the target.

GPS
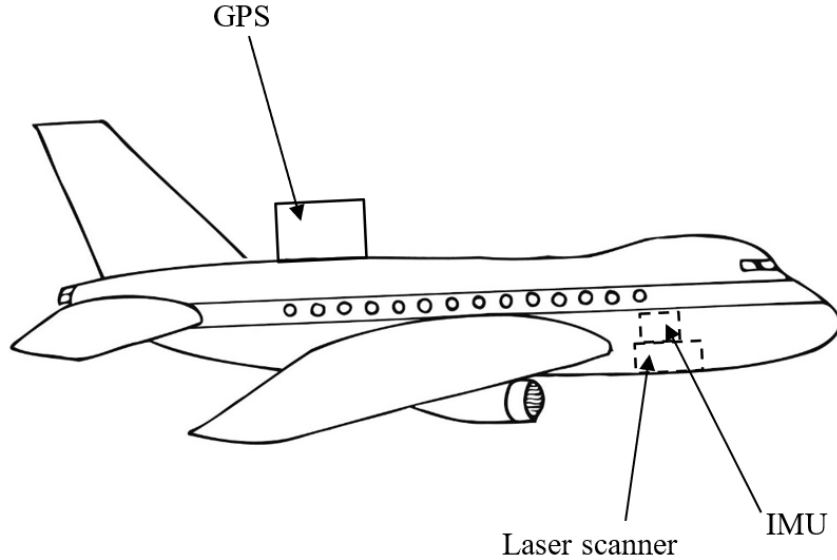
Laser scanner IMU

Fig. 3.1. Laser scanner, GPS, and IMU are amounted at different positions of the aircraft. Each of them has its own coordinate system.

As is mentioned in Section 3.2, there are several alternative approaches to detect and estimate the returns from the digitized waveform signal. If not otherwise stated, the ranges in this thesis are all generated with the nonparametric mixture model and the fuzzy mean-shift algorithm described in Section 3.2.3. Details will be discussed in Chapter 4.

3.3.2 GPS/IMU Incorporation and Conversion

The GPS and the IMU are measured at different sampling rate, and they will be integrated and interpolated. At the same time, the integrated results are converted to the laser frame, i.e. the body frame. The conversion requires the knowledge of the two distances between the origin of the body frame and the local frames. Specifically, the distance between the GPS antenna and the laser scanner is defined as the GPS lever arm; the distance between the IMU instrument and the laser scanner is the IMU lever arm.
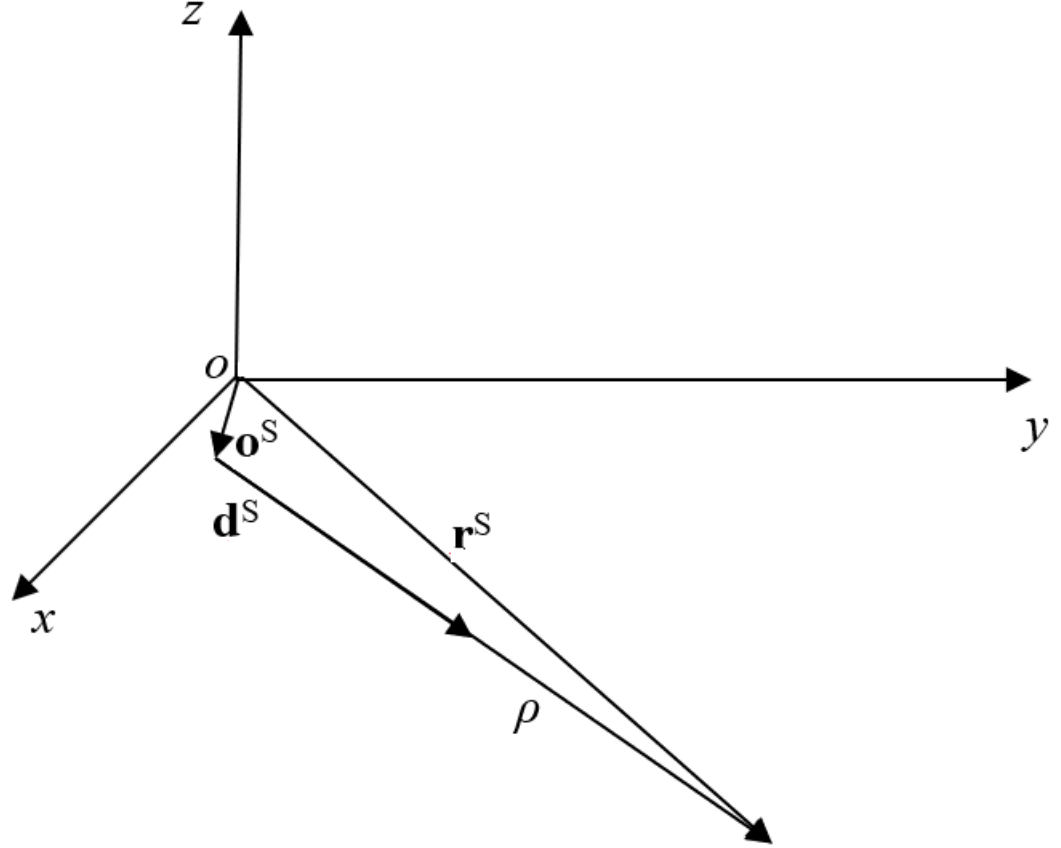
Fig. 3.2. Target location in the sensor's coordinate system.

Usually, it is difficult to place the GPS antenna close to the lidar sensor because the GPS antenna should be placed on the top of the airplane so that the LOS (line of sight) signals can be received, while the lidar sensor is usually placed on the floor of the aircraft facing the ground below the plane.

On the other hand, the IMU measurement unit could be directly attached to the lidar sensor for maximum stability. The axes of the scanner's coordinate frame should exactly coincide with the IMU coordinate frame, but it cannot be guaranteed. As a result, the mounting misalignment angles $\delta\omega, \delta\phi, \delta\kappa$ for roll, pitch and yaw,
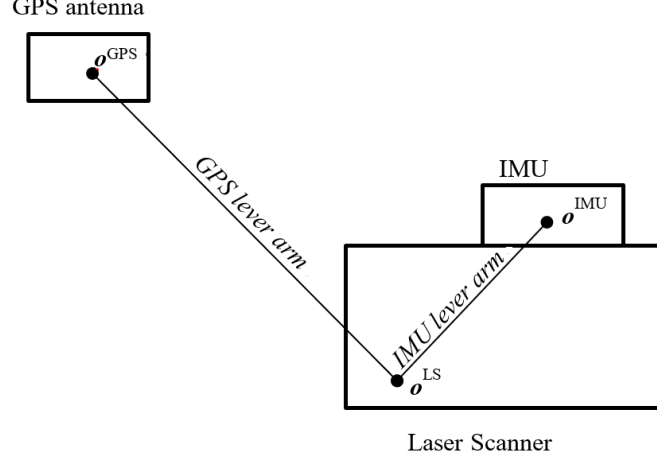
Fig. 3.3. Lever arm offsets. $\boldsymbol{o}^{\mathrm{GPS}}$, $\boldsymbol{o}^{\mathrm{IMU}}$ and $\boldsymbol{o}^{\mathrm{LS}}$ are the origins of the GPS frame, IMU frame, and laser scanner frame, respectively.

exist. These misalignment angles are called boresight misalignments. They will be determined in the calibration stage.

3.3.3 Coordinate Transformation to the Mapping Frame

There are a series of transformations to be applied for georeferencing the calculated target positions into the ground coordinate system (mapping frame). Fig. 3.4. shows a graphical representation of the transformations that need to be performed. After the lever arm offsets are incorporated in the GPS/INS integration, $\mathbf{a}^b$ can be omitted. The sequence of transformations may be represented by multiple rotation and translation operations on the initial position vector in matrix notation as

$$\mathbf{r}^m_{target}(t_S, t_{IMU}) = \mathbf{r}^m_{platform}\left(t_{IMU}\right) + \mathbf{R}^m_H\left(t_{IMU}\right) \cdot \mathbf{R}^H_{IMU}\left(t_{IMU}\right) \cdot \mathbf{R}^{IMU}_S \cdot \mathbf{r}^S_{target}\left(t_S\right) \quad (3.7)$$

where $\mathbf{r}^S_{target}\left(t_S\right)$ is the position vector of the target point in the scanner frame, $\mathbf{r}^m_{platform}\left(t_{IMU}\right)$ is the interpolated coordinates of the GPS/INS integrated solution for trajectory in the mapping frame and $\mathbf{r}^m_{target}(t_S, t_{IMU})$ is the position vector of the target point in the mapping frame. $\mathbf{R}^m_H$, $\mathbf{R}^H_{IMU}$, $\mathbf{R}^{IMU}_S$ are matrices that transform the coordinates from the sensor frame to the IMU frame, from the IMU frame to

the horizontal frame (Shan and Toth, 2018), and from the horizontal frame to the mapping frame, respectively.
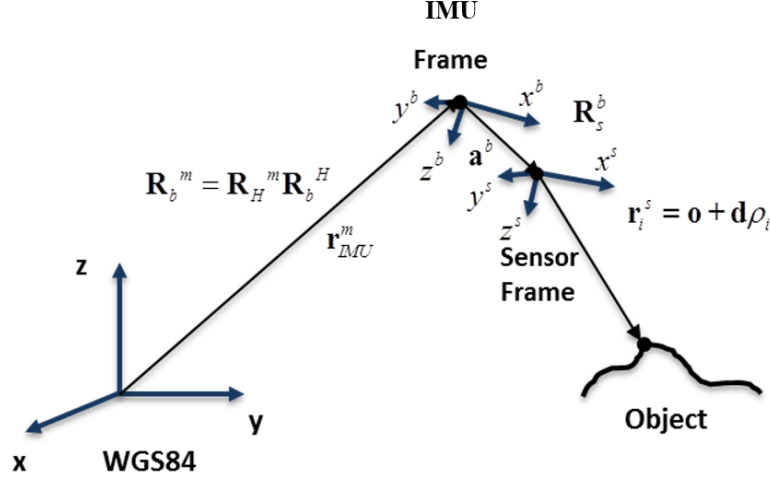
Fig. 3.4. Transformations for georeferencing the position vectors of the targets. (Shan and Toth, 2018)

The first transformation to be applied for georeferencing the target positions is the transformation of the target's position vector calculated in the scanner's coordinate frame to the IMU frame represented by a rotation as $\mathbf{R}_S^{IMU} \cdot \mathbf{r}_{target}^S(t_S)$.

The transformation from the IMU frame to the mapping frame $\mathbf{R}_{IMU}^m$ consists of two consecutive rotations. The first one is the rotation from the IMU frame to the local horizontal NED (North-East-Down) frame and then to the WGS84 geocentric ECEF (earth-centered, earth-fixed) mapping frame. The matrix $\mathbf{R}_{IMU}^m(t_{IMU})$ can be written as

$$\mathbf{R}_{IMU}^m(t_{IMU}) = \mathbf{R}_H^m(t_{IMU}) \cdot \mathbf{R}_{IMU}^H(t_{IMU}) \qquad (3.8)$$

$\mathbf{R}_{IMU}^H(t_{IMU})$ is the rotation matrix established with the roll, pitch, and yaw angles represented by $\omega(t_{IMU})$, $\phi(t_{IMU})$, and $\kappa(t_{IMU})$. For convenience, we omit the t variable in the entry of the matrix:

$$\mathbf{R}_{IMU}^{H}\left(t_{IMU}\right) = \begin{bmatrix} m_{11} & m_{12} & m_{13} \\ m_{21} & m_{22} & m_{23} \\ m_{31} & m_{32} & m_{33} \end{bmatrix} \tag{3.9}$$

$$\begin{bmatrix} m_{11} \\ m_{21} \\ m_{31} \end{bmatrix} = \begin{bmatrix} cos\left(\kappa\right)cos\left(\phi\right) \\ sin\left(\kappa\right)cos\left(\phi\right) \\ -sin\left(\phi\right) \end{bmatrix}$$

$$\begin{bmatrix} m_{12} \\ m_{22} \\ m_{32} \end{bmatrix} = \begin{bmatrix} cos\left(\kappa\right)sin\left(\phi\right)sin\left(\omega\right) - sin\left(\kappa\right)cos\left(\omega\right) \\ sin\left(\kappa\right)sin\left(\phi\right)sin\left(\omega\right) + cos\left(\kappa\right)cos\left(\omega\right) \\ cos\left(\phi\right)sin\left(\omega\right) \end{bmatrix}$$

$$\begin{bmatrix} m_{31} \\ m_{32} \\ m_{33} \end{bmatrix} = \begin{bmatrix} cos\left(\kappa\right)sin\left(\phi\right)cos\left(\omega\right) + sin\left(\kappa\right)sin\left(\omega\right) \\ sin\left(\kappa\right)sin\left(\phi\right)cos\left(\omega\right) - cos\left(\kappa\right)sin\left(\omega\right) \\ cos\left(\phi\right)cos\left(\omega\right) \end{bmatrix}$$

The latter rotation matrix $\mathbf{R}_{H}^{m}\left(t_{\text{IMU}}\right)$ is defined by the geographic latitude, $\Phi_0\left(t_{\text{IMU}}\right)$, and longitude, $\Lambda_0\left(t_{\text{IMU}}\right)$, which is established as

$$R_{H}^{m}\left(t_{IMU}\right) = \begin{bmatrix} -\cos\Lambda_0\sin\Phi_0 & -\sin\Lambda_0 & -\cos\Lambda_0\cos\Phi_0 \\ -\sin\Lambda_0\sin\Phi_0 & \cos\Lambda_0 & -\sin\Lambda_0\cos\Phi_0 \\ \cos\Phi_0 & 0 & -\sin\Phi_0 \end{bmatrix} \tag{3.10}$$

Again, the time variance is omitted for all the entries in the matrix.

3.4 Calibration

The result of direct georeferencing is usually not satisfying such that considerable displacement between overlapping strips can be observed. Thus, we need to consider the error sources during the direct georeferencing and develop calibration schemes to correct the main error sources.

The error sources of a lidar system can be grouped as intrinsic and extrinsic ones. Examples of the intrinsic errors are the inherent INS drift, the noise of scanner

mirror, etc. Extrinsic errors include boresight misalignment, lever arm offsets, and the synchronization among GPS, INS, and laser scanner. In this thesis we assume that the intrinsic errors of the lidar system are minimized by the manufacturer, so we focus mainly on the determination of the extrinsic errors.

Among the extrinsic errors, the lever arm offsets are constant regardless of the range. Once the system is assembled, the lever arm offsets can be determined by surveying instrument or design drawing (Vallet and Skaloud, 2004; Skaloud and Lichti, 2006; Bender et al., 2013). Generally, the accuracy is sufficient so that the remaining errors are negligible compared to other influences (Hebel and Stilla, 2012). On the contrary, the impact of the boresight misalignment to the measurements raises with the increased range. For example, an angular error of only 0.1 degree can result in measurement errors of over 1m at a flight height of 600m. In airborne lidar systems, the platform usually operates at an altitude of hundreds of meters. The boresight misalignment can therefore be substantial.

The boresight angles $\delta\omega$, $\delta\phi$, $\delta\kappa$ for roll, pitch, and yaw are difficult to obtain from direct laboratory measurement. They can only be calculated indirectly (estimated by least squares calibration) (Chan, 2011). Traditionally, they can be solved by a calibration process prior to data acquisition or an adjustment after the data is acquired.

The pre-calibration process needs calibration toolkit, ground truth, and a specially designed flight plan. Such a flight plan is referred to as boresight flight. The requirement of the boresight flight includes the configuration of opposing flight directions, crossing flight lines, different flight heights, and multiple flight strips with significant overlapping. Furthermore, the selected area for the boresight flight should have large numbers of control points such as houses with shingle roof tops (Fowler and Kadatskiy, 2010).

The data users usually have little control over the pre-calibration process unless they closely work with the data provider. Instead, the post-adjustment could be conducted after the data is collected and delivered, under the condition that the data

is collected with overlapped strips and large amounts of regularly shaped objects (Rentsch and Krzystek, 2012). In such cases, an algorithm can be developed to determine the extrinsic errors by co-registering the buildings in different lidar strips.

As a new development, a single flight strip calibration is proposed in this dissertation. The novel approach makes use of the full waveform data together with the publicly accessible DEM to estimate the boresight angles by solving an optimization problem

$$(\delta\omega, \delta\phi, \delta\kappa)^* = \underset{(\delta\omega,\delta\phi,\delta\kappa)}{argmin} ||DEM_{lidar}(\delta\omega,\ \delta\phi, \delta\kappa) - DEM_{ref}|| \qquad (3.11)$$

where $DEM_{lidar}(\delta\omega, \delta\phi, \delta\kappa)$ is the DEM model obtained from the full waveform lidar data with the given values of $(\delta\omega, \delta\phi, \delta\kappa)$ and DEM_{ref} is the reference DEM.

With the proposed calibration approach, the boresight parameters can be solved with a single strip of waveform data. Furthermore, the new approach can be applied with the data obtained over the areas such as mountains, forests, where the regularly shaped objects can be rarely found.

3.5   Processing Flowchart

The flowchart of waveform geospatial processing is shown in Fig. 3.5. Having the ranges and the directions of the emitted laser signals, we can calculate the coordinates of the targets in the sensor coordinate frame. Using the positions of the platform recorded in the SBET file, a series of coordinate transformations described in Section 3.3 are then carried out to calculate the coordinates of the targets. It should be noted that the flight trajectory is not available at the same frequency as the pulse repetition rate of the lidar sensor. The pulse repetition rate of the lidar system is 400 kHz while the trajectory is available at 200 Hz. Only one trajectory position is available for approximately every 2,000 laser pulses due to this difference in data frequency. The position and the orientation of the sensor platform are calculated by interpolation of the trajectory at each time instance of laser pulse emission. As is mentioned, the

boresight angles will be estimated by comparing the lidar point cloud with a reference DEM through an optimization procedure.
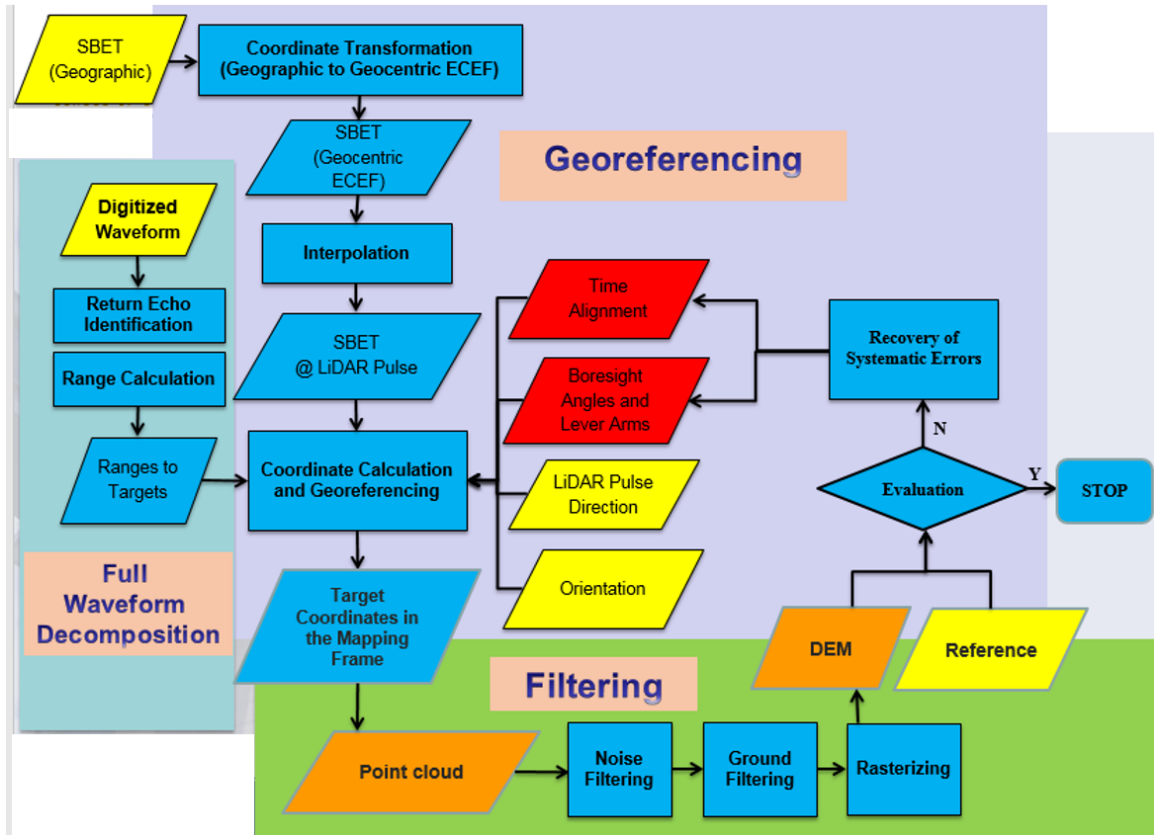
Fig. 3.5. Flowchart of waveform lidar data processing.

4. PARAMETRIC WAVEFORM DECOMPOSITION

In lidar measurement, the distance between the laser scanner and the target is derived from the waveform decomposition result. A suitable waveform model and decomposition algorithm is indispensable to assure the accuracy and quality of lidar products.

The emitted signal from the laser scanner is continuous wave. In many airborne lidar systems, the duration of emitted signal is several nanoseconds. The duration of the returned waveform is usually at the similar length or longer. The waveform can be modelled with parametric approach or with nonparametric approach (Hartzell et al., 2015; Li et al., 2016). Correspondingly, waveform decomposition is a common step for exploitation of full waveform lidar data. Much effort has been focused on designing algorithms based on the assumption that the returned waveforms follow a Gaussian Mixture Model (GMM) where each component is a Gaussian.

As is observed from Chapter 2, the emitted signal usually has a bell-shaped main component and a noise floor. The parametric approach models the bell-shaped main component as a parametric function. The simplest example is a Gaussian function. As a sequence, the returned waveform will become a mixture of several parametric functions, e.g., Gaussian functions. Gaussian-mixture model and corresponding algorithms have been the dominant approach for parametric waveform decomposition. Their principle and the performance will be studied in this chapter.

4.1 Gaussian Mixture Model (GMM)

The Gaussian mixture model (GMM) is the most widely adopted model for lidar waveforms. First, it assumes that the emitted signal has the Gaussian form of

$$y_{emitted}(t) = Y \cdot \exp\left[-\frac{(t-\mu)^2}{2\sigma^2}\right] \tag{4.1}$$

where the emitted signal $y(t)$ is a variable of t, the sampling time. Y is a constant, μ corresponds to the emitted time, and σ models the width of the waveform.

When the emitted signal hits an object and reflects towards the lidar sensor, a returned waveform will be received. The returned waveform also has a noise floor and a main component that is bell-shaped as the emitted signal. When more than one object is encountered, there will be multiple bell-shaped components in the returned waveform and some of them may be convoluted or mixed. This phenomenon is described by a mixture model:

$$y_{returned}(t) = \sum_{j=1}^{J} w_j \cdot y_j(t) \tag{4.2}$$

where $y_j(t)$ is the curve function of the j-th component, and w_j is its weight. J is the total number of components, or the number of detected targets.

The bell-shaped components in the returned waveform are then approximated by Gaussian curves as well. Under this assumption, the returned waveform can be expressed as a Gaussian mixture model:

$$
\begin{aligned}
y_{returned}(t) &= \sum_{j=1}^{J} w_j \cdot y_j(t) \\
&= \sum_{j=1}^{J} w_j \cdot \exp\left[-\frac{(t-\mu_j)^2}{2\sigma_j^2}\right]
\end{aligned}
\tag{4.3}
$$

where μ_i and σ_i model the position and the width of each Gaussian component. J is also called the order of the Gaussian mixture model.

4.2 Expectation-Maximization (EM) algorithm

The waveform decomposition problem under GMM is to find the parameters $\theta = [J, \theta_J]$ where $\theta_J = [w_1, \mu_1, \sigma_1, \ldots, w_J, \mu_J, \sigma_J]$. Many algorithms are proposed to

decompose the waveform data based on GMM. The most widely used and cited parametric approach to decompose the waveform is the Expectation-Maximization (EM) method (Dempster et al., 1977; Vlassis et al., 2002). It is an algorithm that classifies a group of random variables at the same time of estimating the sufficient statistics with maximization likelihood method. The first step of applying EM to waveform decomposition is to model the waveform as the histogram of a random variable. Let a (returned) waveform be collected along time t from tag 1 to T. We regard the waveform $Y = \{y(t) : y(t) \geq 0, 1 \leq t \leq T\}$ as the histogram of samples of a random variable x, $X = \{x_n : 0 \leq x_n \leq T, 1 \leq n \leq N\}$, where n is the sample index and N the total number of samples. The total number of samples will be $N = \sum_{t=1}^{T} y(t)$. Each observation xn is classified as one or more of the clusters $j = [1, \ldots, J]$ with weight $w = [w_1, \ldots, w_J]$ and $\sum_{i=1}^{J} w_j = 1$. If each cluster follows a Gaussian distribution $N(\mu_j, \sigma_j^2)$, the likelihood of x_n in cluster j will be $\frac{1}{\left(2\pi\sigma_j^2\right)^{\frac{1}{2}}} \exp\left[-\frac{(x_n - \mu_j)^2}{2\sigma_j^2}\right]$.

Under the framework of EM, the following likelihood function should be maximized:

$$p(x|\theta_J, \ J) = \prod_{n=1}^{N} \sum_{j=1}^{J} \frac{w_j}{\left(2\pi\sigma_j^2\right)^{\frac{1}{2}}} \exp\left[-\frac{(x_n - \mu_j)^2}{2\sigma_j^2}\right] \tag{4.4}$$

where the parameter vector of the J-mixture distribution is given by $\theta_J = [w_1, \ \mu_1, \sigma_1, \ldots, w_J, \ \mu_J, \sigma_J]$. J is assumed known for EM. The expected sufficient statistics of this distribution, when θ is given, can be computed for the j-th component as

$$N_j = \sum_{n=1}^{N} P\left\{x_n \in \text{the } j - \text{th component}|\widehat{\theta}_J\right\}$$

$$t_{1,j} = \sum_{n=1}^{N} x_n \cdot P\left\{x_n \in \text{the j} - \text{th component}|\widehat{\theta}_J\right\} \tag{4.5}$$

$$t_{2,j} = \sum_{n=1}^{N} x_n^2 \cdot P\left\{x_n \in \text{the j} - \text{th component}|\widehat{\theta}_J\right\}$$

The maximum likelihood (ML) estimate of θ_J, given (4.5), is

$$\hat{\mu}_j = \frac{x_{1,j}}{N_j},$$

$$\hat{\sigma}_j^2 = \frac{x_{2,j}}{N_j} - \frac{x_{1,j}^2}{N_j^2}, \tag{4.6}$$

$$\hat{w}_j = \frac{N_j}{N}.$$

The expected statistics and the parameter estimation will be iteratively calculated until the likelihood function described in (4.4) converged or the maximum number of iteration is reached.

4.3   Method of Model Selection

The number of clusters J in a waveform cannot be directly estimated with the EM approach. The problem of estimating J, the order of a model, is called order identification. Order identification methods generally require the addition of a penalty term in the log likelihood to account for the over-fitting of high order models.

There exist different approaches to determine the optimal value of J, such as Akaike information criterion (Akaike, 1974), Bayesian Information Criterion (Schwarz, 1978), Minimum Description Length (Rissanen, 1983). The comparison of different model selection methods is beyond the scope of this study. In our work, we arbitrarily employ an order identification/model selection method based on the Minimum Description Length (MDL) principle to choose J. The MDL criterion tries to find the optimal model order, which minimizes the number of bits that would be required to code both the data samples x_n and the parameter vector θ. It is given by

$$MDL\left(\theta_J, \ J\right) = -\log p_x\left(x|\theta_J, \ J\right) + \frac{1}{2}L\log\left(N \cdot D\right) \tag{4.7}$$

where L is the number of continuously valued real numbers required to specify the parameter θ_J, and D is the dimension of the data. It can be observed that the $MDL(J)$ is essentially the negative log-likelihood function $NLL(J) = -\log p_x\left(x|\theta_J, \ J\right)$ with an addition of a linear penalty term $\frac{1}{2}L\log\left(N \cdot D\right)$.

In the case of lidar waveform decomposition, we have $L=3J-1$ and $D=1$. Under the MDL criterion, J is chosen by

$$\hat{J} = \arg\min_{J} MDL\left(\hat{\theta}_J, J\right) = \arg\min_{J} \left[-\log p_x\left(x|\hat{\theta}_J, J\right) + \frac{1}{2}L\log\left(N \cdot D\right)\right] \quad (4.8)$$

Rigorously, it requires all the values of $MDL\left(\hat{\theta}_J, J\right)$, J=1,2, ..., to be calculated. Since the calculation of $MDL\left(\hat{\theta}_J, J\right)$ involves the value of estimated $\hat{\theta}_J$, all θ_J, J=1,2,..., need to be estimated in order to optimize J.

4.4 Experiments

In this section, the mechanism of EM will be demonstrated with the data that is described in Section 2.4.

4.4.1 Noise Filtering

The first step of processing waveform data usually is to filter out its noise. Since the waveform components in our study are smooth enough, the effort of further smoothing is not necessary. Instead, the noise can be filtered out by simply applying a noise threshold (Fig. 4.1.). However, the waveform decomposition result may be sensitive to the selection of this threshold. This phenomenal can be shown by a waveform decomposition example. Fig. 4.1. shows the original waveform. The decomposed results under different noise thresholds are summarized in Table 4.1. In the table, not only the parameters θ_J but also the number of waveform components J vary as the noise threshold changes.

An ideal threshold should be right above the noise floor so that it can keep the main information embedded in the waveform at the same time of filtering out the noises. Over-filtering will make the result deviate from the correct value or lose points, while under-filtering will introduce noise points. In our experiment, a threshold of 15 is applied to all the original waveforms.

Table 4.1.

Decomposition result of a sample waveform with different noise thresholds

Noise threshold	J	θ_J								
		μ			σ			w		
		μ_1	μ_2	μ_3	σ_1	σ_2	σ_3	w_1	w_2	w_3
5	3	17.87	23.34	31.42	1.94	2.28	2.40	0.33	0.60	0.07
6	3	17.88	23.34	31.04	1.94	2.28	2.14	0.33	0.61	0.06
7	3	17.87	23.35	31.12	1.94	2.30	2.31	0.34	0.62	0.05
8-9	2	17.86	23.40	-	1.95	2.40	-	0.34	0.66	-
10-11	2	17.84	23.31	-	1.73	2.44	-	0.31	0.69	-
12-18	2	17.94	23.33	-	1.76	2.22	-	0.34	0.66	-
19-20	2	17.99	23.25	-	1.76	1.99	-	0.36	0.64	-
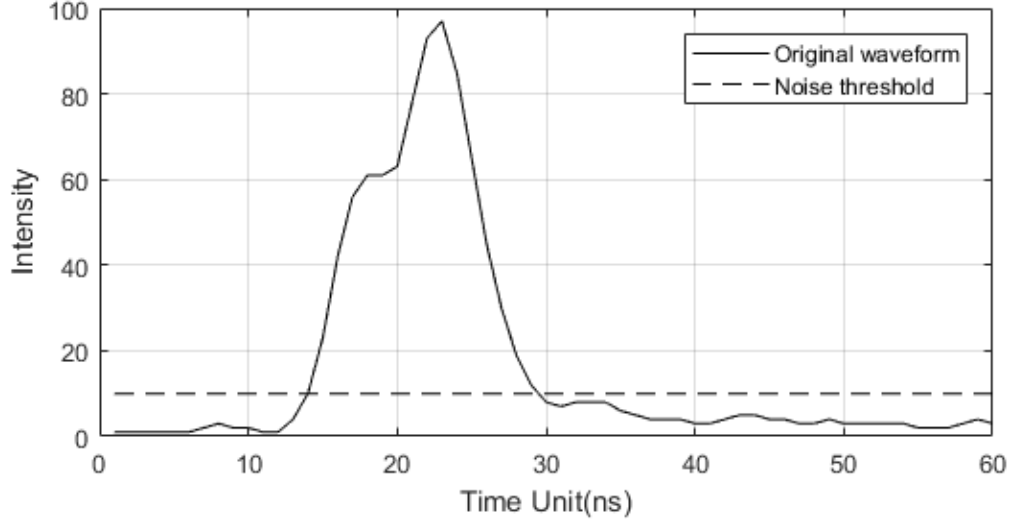
Fig. 4.1. Noise filtering with a threshold.

4.4.2 Determine the Number of Clusters

We applied the MDL to the EM-decomposed lidar waveforms. One of the sample results is presented in Fig. 4.2. The initial guess of the number of Gaussian components is 4, as illustrated in Fig. 4.2(a). By minimizing the MDL curve, the number of components is determined to be 5, as is shown in Fig. 4.2(b). We observe that a missing component located at the left shoulder of the first pulse is found. It is noted from Fig. 4.2(c) that the search range of J is [1, 30], meaning that EM was conducted 30 times to search for a global minimum point. This conservative search range is determined by the fact that the minimal value of J could be 1 (at least 1 target detected) and the maximal value of J could be $\lfloor((N+1))/3\rfloor$, where $\lfloor \cdot \rfloor$ denotes round down. In our data, there are 120 samples in each block and only 91 of them are non-zero samples, meaning that $\max \hat{J} = \lfloor((91+1))/3\rfloor = 30$. In other words, the possible range of J is [1, 30]. We observed from Fig. 4.2(c) that $MDL(J)$ behaves like a convex function. This can be explained by the observation that the $MDL(J)$ is the sum of the negative log-likelihood function $NLL(J)$ and an addition of a linear

penalty term. A convex-like $MDL(J)$ implies a convex-like $NLL(J)$. $NLL(J)$ will be convex if its first derivative is negative and its second derivative is positive. Since the performance of $J+1$ components are always no worse than that of J components, $NLL(J)$ therefore has a negative first derivative. On the other hand, the improvement of likelihood given by a further increasing J usually becomes less, meaning that the second derivative of $NLL(J)$ is ideally negative. Based on the above evaluation, we search for the local minimum of $MDL(J)$ from J_0, which is determined by simply detecting local peaks in the waveform.

Using this strategy, we analyzed the sample waveform in Fig. 4.3(a). The MDL criterion was applied in such a way that it searched for a local minimum at both sides of the initial value of J. The initial guess of the number of Gaussian components was 5 and the number of components determined by EM-MDL was 3. Only four EM-MDL iterations were applied to determine the local minimum.

4.4.3   Results

We applied the EM-MDL method to estimate the number of Gaussian components for the entire data. In most cases, three iterations are sufficient to find out the local minimum. When there is single Gaussian component, only two iterations are necessary. The histogram for the number of iterations is shown in Fig. 4.4(a), from which it is clear that 88% of the data can be converged within three iterations.

We can see from Fig. 4.4(b) that 88% of the waveforms have 1-4 Gaussian components. Even though our test data has a small footprint of 2.5cm, 12% of returned waveforms have 5-12 components.

4.5   Discussion

The GMM-based waveform decomposition method is based on two assumptions: (1) the emitted lidar signal is a Gaussian waveform; (2) the returned waveform is also a sum of Gaussian, though its mean (intensity), standard deviation, and the
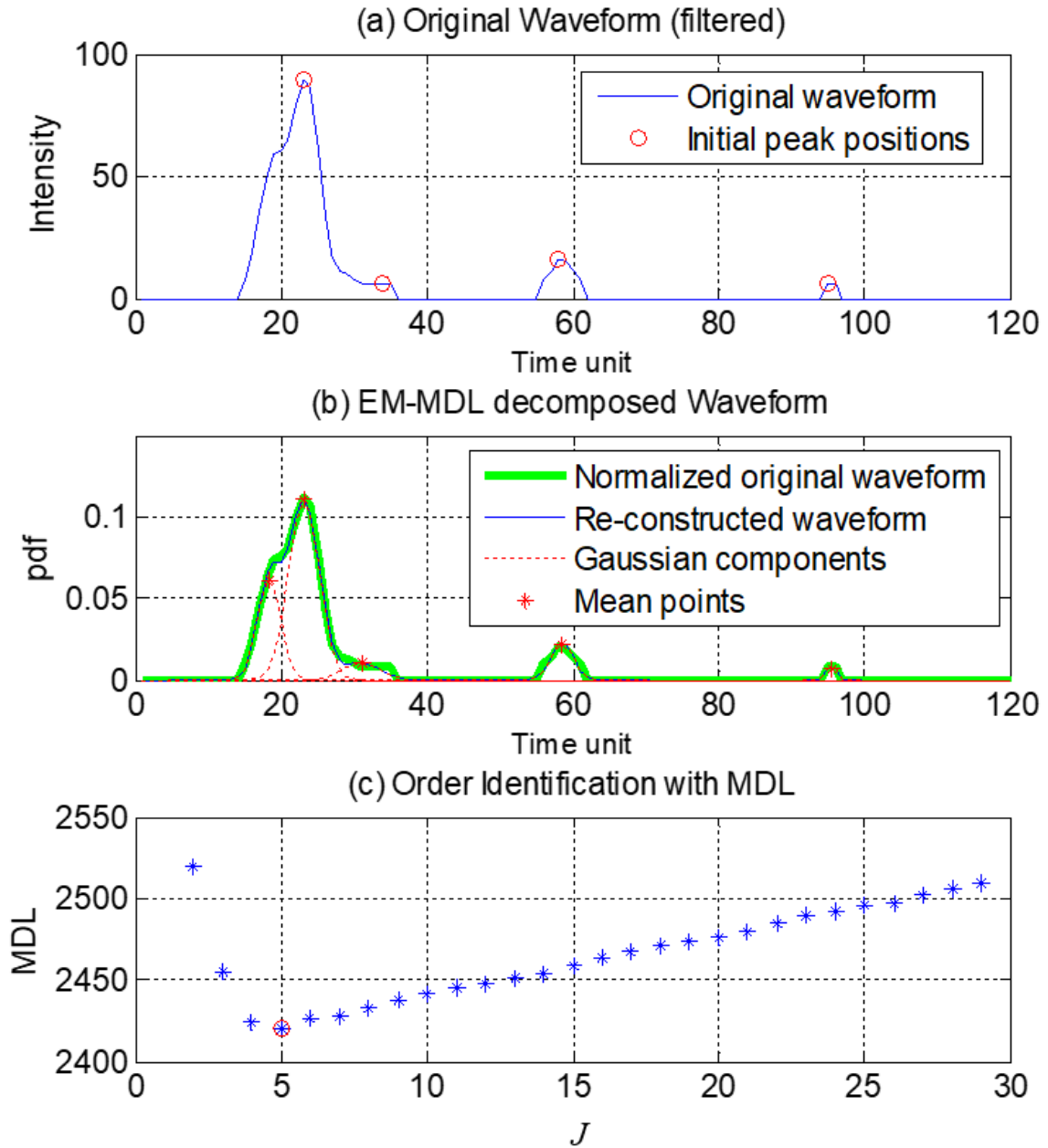
Fig. 4.2. EM-MDL decomposition results with global search. The optimal point is circled in red in (c).

number of Gaussian waveform components may vary from waveforms to waveforms. However, these assumptions are not always true. First, the emitted signal of the
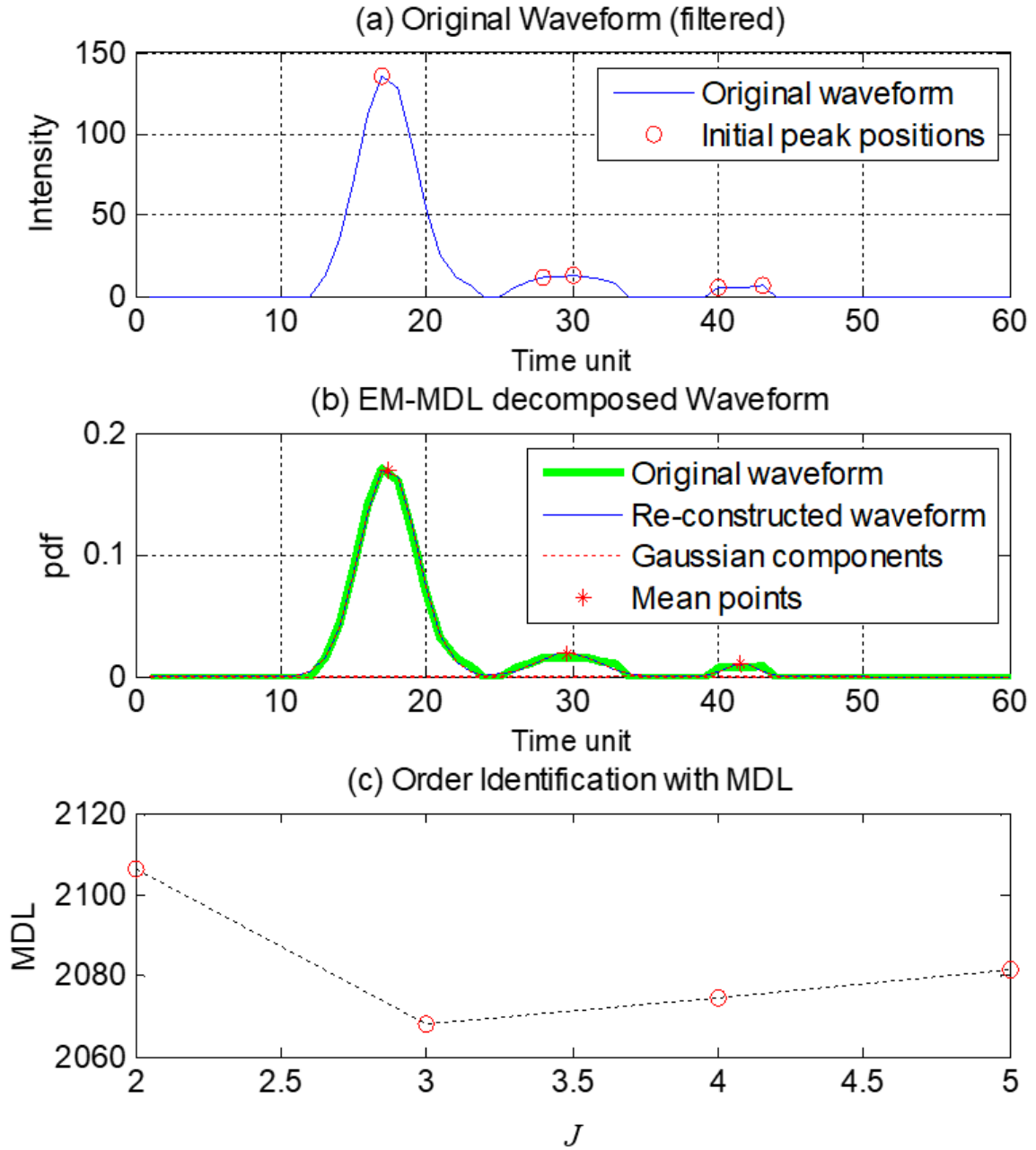
Fig. 4.3. EM-MDL decomposition results with local search.

widely adopted Q-switched laser scanner usually exhibits asymmetric non-Gaussian curves, as can be seen in Section 2.1. Even though the laser sensors can generate an
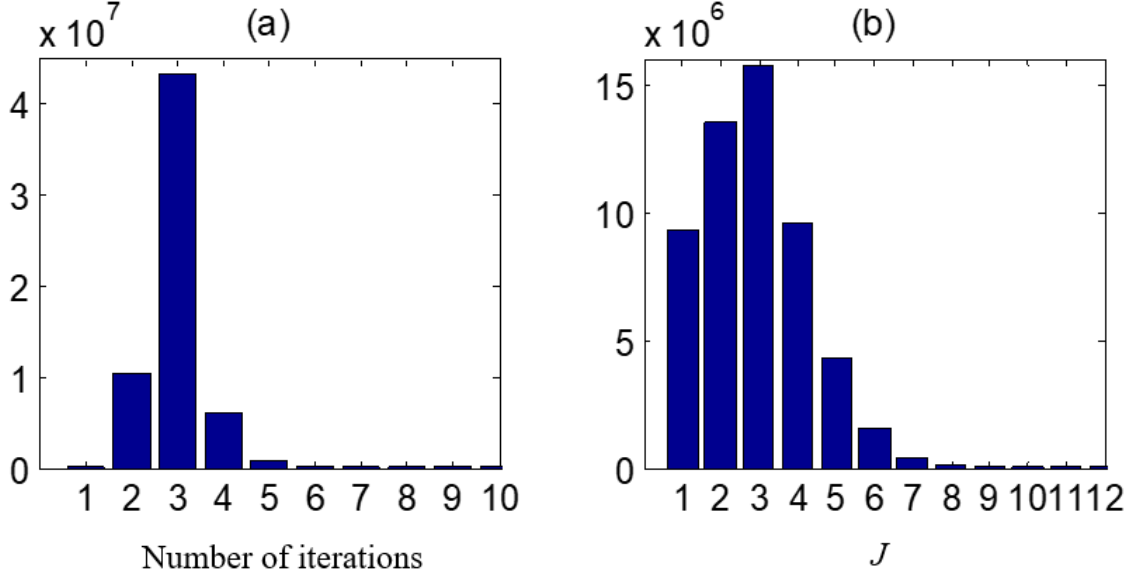
Fig. 4.4. Histograms of MDL-based estimation of J: (a) Number of iterations; (b) Number of Gaussian components.

electromagnetic wave that leads the intensity of emitted signals close to a Gaussian, the intrinsic noise in the electrical device will introduce flat tails to the actual signal, as is shown in Fig. 4.6(a). The tails make the curve look more like a Cauchy curve than a Gaussian (Casella and Berger, 2001). Moreover, the transmission path and/or the reflectance of a target can also alternate the signal in a way that further deviates from Gaussian. It is common for a single waveform component to be asymmetric, skewed and non-Gaussian, as is shown in Fig. 4.6(b). As a result, the GMM is unable to precisely model non-Gaussian waveform components, particularly asymmetric waveform components that have been frequently reported by researchers (Słota, 2014; Chauve, et al., 2007; Montes-Hugo, et al., 2014).

Besides this unrealistic GMM assumption, most parametric decomposition techniques, e.g., EM and Levenberg-Marquardt methods have the following limitations: (1) the number of total decomposed components, J, should be prescribed in the stage of initialization. To determine the optimal J, peak detection could be applied and
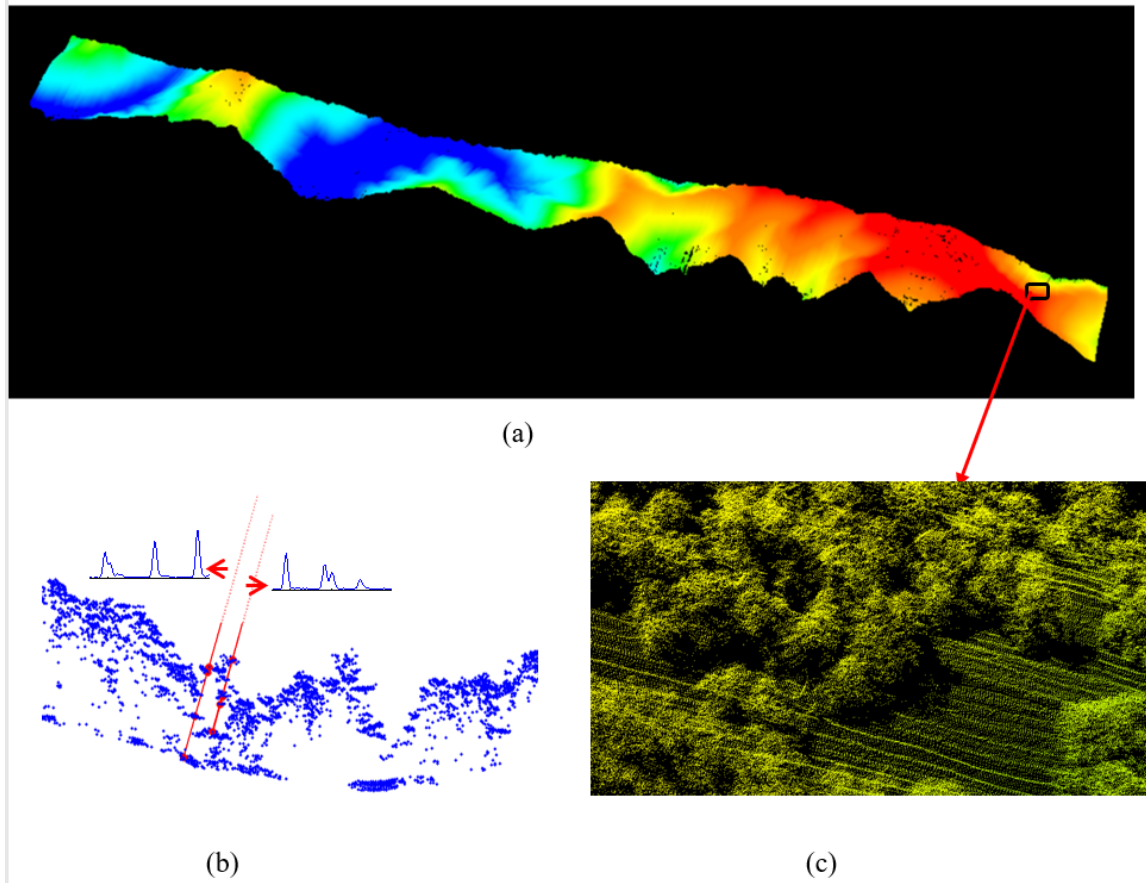
Fig. 4.5. Point clouds generated in our work: (a) the entire profile of the point cloud; (b) Two sample waveforms, each with four components, corresponding to four points (in red dots); (c) a zoom-in view of the point cloud.

the algorithms need to run multiple times to compare the results from different J's; (2) a filtering process is desired prior to waveform decomposition because the involvement of noise will deteriorate the performance of decomposition. However, there is no standard way to filter out the noise floor (Page-Jones, 2003) in the waveform. In our experiment, the simple and popular way of a constant noise threshold is applied. As a result, the parametric algorithms are sensitive to the threshold value and the waveform is often either over filtered or under filtered. Furthermore, the complexity of the parametric algorithms is greatly increased not only because the algorithms
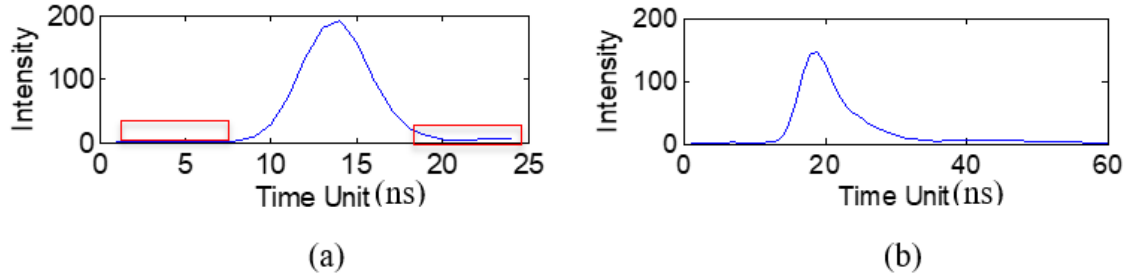
Fig. 4.6. Non-Gaussian signal in lidar. (a) An emitted lidar signal of Riegl Q680i. The flat tails (non-informative) are highlighted in boxes. (b) The right-skewed returned waveform of (a).

themselves are iterative but because a preprocessing for estimating the number of components and/or a postprocessing for optimizing this number are often needed. In lidar waveform decomposition, any additional preprocessing and/or postprocessing are computationally expensive because they ought to apply to each and every individual waveform.

5. NONPARAMETRIC WAVEFORM DECOMPOSITION

Since GMM is not capable of modeling the asymmetric lidar waveforms and other parametric models are also constrained by the pre-defined library, it is necessary to explore the possibility of new models to describe lidar waveforms. The objective of the new model is: (1) takes possible asymmetric waveform components into account; (2) allows the popular GMM model to be its special case; and (3) yields a high-quality, high-efficiency decomposition. To address the first two properties, we introduce a nonparametric mixture model (NMM); whereas, for achieving the third property, we propose a fuzzy mean-shift (FMS) clustering algorithm.

The nonparametric model does not restrict the shape of the waveform components so that asymmetric, non-Gaussian waveform components can be included. Specifically, we model a waveform as a histogram of a collection of random samples of x, $X = \{x_n : 0 \leq x_n \leq T, 1 \leq n \leq N\}$. Under this nonparametric model, the procedure of waveform decomposition will be realized by clustering techniques. Considering the number of waveform components, J, as an unknown parameter besides the waveform components themselves, we introduce a fuzzy mean-shift (FMS) algorithm so that this number can be simultaneously estimated during the process of waveform decomposition. As a result, the waveform is decomposed into several clusters, either symmetric or asymmetric, either informative (useful signal) or non-informative (noise). Comparing with existing methods, the significant advantages of this development is that it assumes neither the waveform components be a Gaussian or of any parametric form, nor the number of waveform components be known beforehand. Moreover, the noise floor can be filtered out at the same time of waveform decomposition.

5.1 Nonparametric Mixture Model (NMM)

The waveform $y(t)$ can be modeled by a nonparametric function as

$$y\left(t\right) = \frac{1}{N \times h} \sum_{n=1}^{N} k\left(\frac{t - x_n}{h}\right) \tag{5.1}$$

A function with the form of equation (5.1) is called nonparametric because it is not assumed to follow any specific distribution. Instead, each sample of x contributes to the waveform through a kernel function $k(\cdot)$, which satisfies

$$\begin{aligned} &\sup \left|k\left(x\right)\right| < \infty \\ &\int_R \left|k\left(x\right)\right| < \infty \\ &\lim_{\left|x\right|\to\infty} \left|x\right| \cdot k\left(x\right) = 0 \\ &\int_R \left|k\left(x\right)\right| dx = 1 \end{aligned} \tag{5.2}$$

and the parameter h is the bandwidth of the kernel function, which determines the density of the lidar point cloud to be generated through this decomposition. Examples of the kernel functions include a rectangle function, a triangle function, or a Gaussian function. A complex kernel function like a Gaussian can make the histogram smoother, while a simple kernel function like a rectangle may consume less computation time.

When more than one target is encountered by an emitted lidar signal, there will be multiple components $y_1(t), y_2(t), ..., y_J(t)$ in the (returned) waveform. Each waveform component $y_i(t)$ is a cluster of x samples. It can be described by a mixture model as

$$y\left(t\right) = \sum_{j=1}^{J} y_j\left(t\right) = \sum_{j=1}^{J} \left[\frac{1}{N_j \times h} \sum_{n_j=1}^{N_j} k\left(\frac{t - x_{n_j}}{h}\right)\right] \tag{5.3}$$

where $y_j(t)$ is the j-th component. Here $y_j(t)$ is modeled as a summation of a number of kernel functions evaluated at each point in cluster j. Depending on the clustering result, $y_j(t)$ could fit a Gaussian or any other forms, either symmetric or asymmetric. It is noted that the $y_j(t)$ could be either informative laser energy or non-informative

noise, as is depicted in Fig. 5.1. It is desired that an algorithm can determine and filter the noise levels at the same time as decomposing the waveforms.
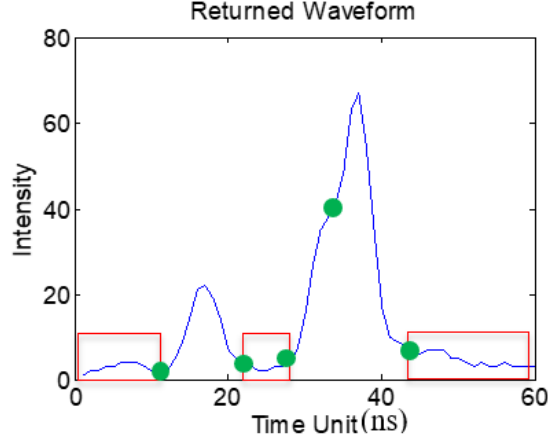
Fig. 5.1. In a returned waveform, the non-informative noise is high-lighted in boxes and the possible mixture positions of two clusters are in dots.

In (5.3), the samples of x are clustered in a way that each sample belongs to a single component y_j; therefore, all the waveform components are separated without overlap. However, in most cases, lidar waveform components do convolute and are mixed. For example, the waveform intensity at the dots in Fig. 5.1. is contributed by two adjacent, mixed waveform components. To model such phenomenon as GMM does, a mixture weight w_n is introduced and (5.3) is evolved to a mixture model, i.e.,

$$y\left(t\right) = \sum_{j=1}^{J} y_j\left(t\right) = \sum_{j=1}^{J} \left[\frac{1}{N_j \times h} \sum_{n_j=1}^{N_j} w_{n_j} \cdot k\left(\frac{t - x_{n_j}}{h}\right)\right] \tag{5.4}$$

where a sample x_n can be assigned to multiple clusters with the weight w_{n_j}. The nonparametric mixture model (NMM) in (5.4) is the one we introduce for waveform decomposition. We will design an algorithm to determine J, w_{n_j}, and $y_j(t)$, with a preset bandwidth h.

5.2 Fuzzy Mean-Shift (FMS) Algorithm

With NMM, the problem of waveform decomposition becomes a kernel-based clustering problem. Some popular kernel-based clustering methods include the kernel k-means (Dhillon et al., 2004), spectral clustering (Shi and Malik, 2000), support vector machine clustering (Ben-Hur, et al., 2001), and mean-shift clustering (Fukunaga and Hostetler, 1975). Among the different clustering methods, the mean-shift algorithm offers the advantage of being simple and able to estimate the number of clusters at the same time the clustering is performed. This is a desired property for waveform decomposition because the number of waveform components is unknown, varying from waveform to waveform, and most of the existing methods have to put extra effort to estimate it. Moreover, the traditional mean-shift algorithm is a "hard" clustering algorithm suitable for problems described by (5.3), but not suitable for the mixture problems defined in (5.4). Here, we will adapt the traditional mean-shift algorithm to a fuzzy mean-shift (FMS) so that it can be utilized to decompose waveforms with NMM.

The traditional mean-shift algorithm estimates the local modes of the histogram from a random variable x, as we described in (5.1) and (5.3). At any t, the gradient of the waveform function (5.1) and (5.3) can be calculated using the following:

$$\frac{\partial y\left(t\right)}{\partial t} = \sum_{j=1}^{J} \left[\frac{1}{N_j \times h^2} \sum_{n_j=1}^{N_j} k'\left(\frac{t - x_{n_j}}{h}\right) \right] \tag{5.5}$$

Next, we define $\vec{m}\left(t\right)$ as the mean-shift vector shown in (5.6). Its sign indicates the direction of the gradient of the waveform function, i.e., it points towards the region where the majority points of a waveform component reside. In practice, the kernel function $k(\cdot)$ is chosen in such a way that only the data points within the neighborhood (∂t) of x_n contribute to $\vec{m}\left(t\right)$. Thus, $\vec{m}\left(t\right)$ can be written as

$$\vec{m}\left(t\right) = \frac{\sum_{x_n \in \partial t} x_n k\left(\frac{t - x_n}{h}\right)}{\sum_{x_n \in \partial t} k\left(\frac{t - x_n}{h}\right)} - t \tag{5.6}$$

The algorithm starts from an initial point x_0 and moves along the mean-shift vector until it converges at $\vec{m}(t) = 0$. The center of the first waveform component (either informative or noise) is found at this point. During the process, all the data points of x_n that are once located within the search neighborhood will contribute to the vector $\vec{m}(t)$ and form the first waveform component $y_1(t)$. After that the process will be conducted on the rest of the data points and search for the second waveform component $y_2(t)$. The algorithm continues until all the x_n samples are used to form one of the waveform components. In the end, the algorithm returns all the waveform components $y_1(t)$, ..., $y_J(t)$ together with J, the number of found components.

As pointed earlier, the traditional mean-shift algorithm conducts a hard clustering by assigning each data point x_n to a single component and returns a result where all the waveform components are separated without overlap or mixture. To resolve the mixture of waveform components, we adapt the traditional mean-shift to an FMS to conduct "soft" clustering. We notice that the sample points at the border of adjacent waveform components are visited multiple times by different clusters during the mean-shift process. We define such a point as a mixture point and assign it through a fuzzy weight function to all the clusters that once visited the point, i.e.,

$$w_i(x_n) = \frac{v_i}{\sum_{j=1}^{J} v_j} \tag{5.7}$$

where v_i is the number of times that x_n is visited by cluster i. In most cases, a mixture point will be visited by only two adjacent components.

5.3 Experiments

This section will examine the asymmetric properties of the waveform, discuss the selection of bandwidth h of the kernel function, explore the mixture of waveform components, and evaluate the waveform decomposition by comparing its resultant DEM with reference to the USGS National Elevation Dataset (NED) 1/3" DEM.

5.3.1 Skewness of the Emitted Signals and the Returned Waveforms

Since both the sampled emitted pulse and the returned waveform are provided, their symmetry can be evaluated. Let t be the time stamp from 1 to T and $y(t)$ the intensity at t, we can calculate the skewness of the signal according to the Pearson's moment coefficient of skewness γ (Parrish et al., 2014)

$$\gamma = \frac{m_3}{m_2^{3/2}} \tag{5.8}$$

where

$$\bar{t} = \frac{\sum_{t=1}^{T} t \cdot y(t)}{\sum_{t=1}^{T} y(t)}$$
$$m_l = \frac{\sum_{t=1}^{T} (t - \bar{t})^l \cdot y(t)}{\sum_{t=1}^{T} y(t)} \tag{5.9}$$

A positive γ suggests a right skewed waveform and a negative γ a left skewed one; $\gamma = 0$ represents a symmetric waveform.

As examples, two emitted signals and their returned waveforms are shown in Fig. 5.2(a)(b) and (d)(e), respectively. Fig. 5.2(c) exhibits the distribution of γ's for all the 10,000 emitted signals, while Fig. 5.2(f) is the distribution of γ's for the returned one-component waveforms. The emitted signals are slightly right-skewed, whereas their skewness has a mean 0.0563 and standard deviation 0.0194. It coincides the fact that most of the known airborne laser scanners utilize Q-switched lasers. The returned waveforms are considerably skewed with a mean 0.1489 and standard deviation=0.239. Compared to Fig. 5.2(c) for the emitted signals, Fig. 5.2(f) demonstrates that the skewness of 34% of the returned waveforms are greater than 0.15. In other words, right skewed returned waveforms dominate this subset. This demonstrates the need for the nonparametric approach.
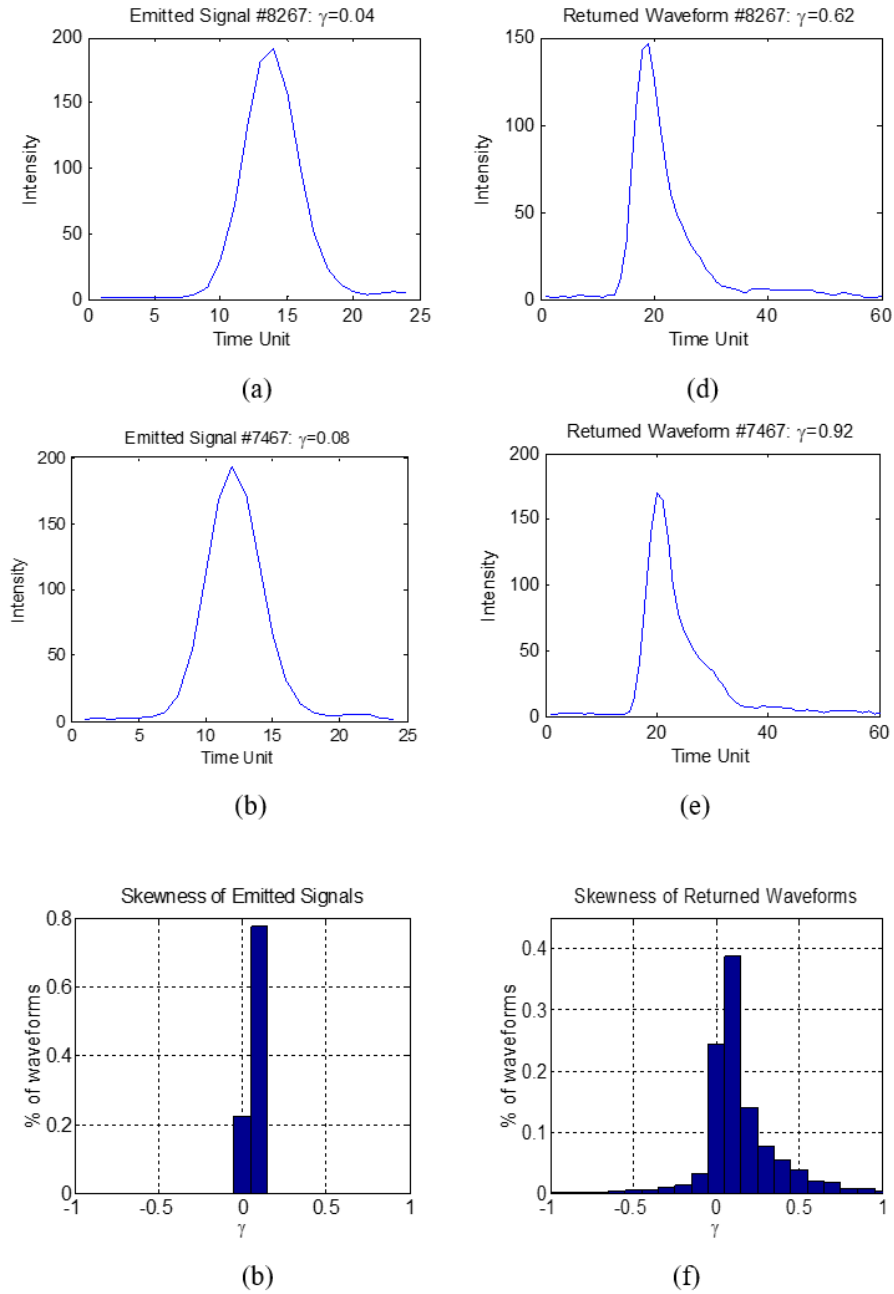
Fig. 5.2. Skewness of lidar emitted signals and returned waveforms. (a-c) Emitted signals: (a) #8267, γ=0.04; (b) #7467, γ=0.08; (c) the distribution of skewness of the emitted signals. (d-f) Returned waveforms: (d) #8267, γ=0.62; (e) #7467, γ=0.92; (f) the distribution of skewness of the returned one-component waveforms.

5.3.2   Selection of the Kernel Function

Application of the kernel density model in the waveforms starts from choosing a kernel function $k(\cdot)$. A few tests on some common kernel functions are shown in Fig. 5.3.

The role of a kernel function is to adjust the contribution of neighboring points to the mean. Based on the distances to a (tentative) mean, they may have different effect to the calculation. However, the mean in our problem is the weighted average or mass center of all data points, where the weighting is taken from the lidar intensities. The data points with higher intensities will contribute more to the final mean determination. In (5.1) we expect N is as large as hundreds, under this situation, different kernel functions are less sensitive to waveform decomposition. In the tests, we select rectangle kernel function because: (1) in our application, the data points are not only dense but also with high intensity, so different kernel functions generate similar results, as is shown in Fig. 5.3.; (2) the simplicity of rectangle kernel makes the mean-shift consume much less time than the case where complicated kernel functions are applied.

5.3.3   Selection of the Bandwidth

The kernel bandwidth, h, is another important factor that controls the density of the point clouds to be generated. Some of the techniques for bandwidth selection include asymptotic expansion (AMISE) minimization (Sheather and Jones, 1991), stability maximization, and isolation-connectivity optimization. In the application of lidar waveform processing, a larger bandwidth will yield a smaller volume of point cloud and a narrower one will lead to a denser point cloud.

In our experiment, we choose h=3.3 as the bandwidth, where h is measured by the number of sampling time intervals or data points. The following facts are considered for selecting such value: (1) the bandwidth essentially determines the minimum width of a waveform component. Since we need at least three data points to determine a
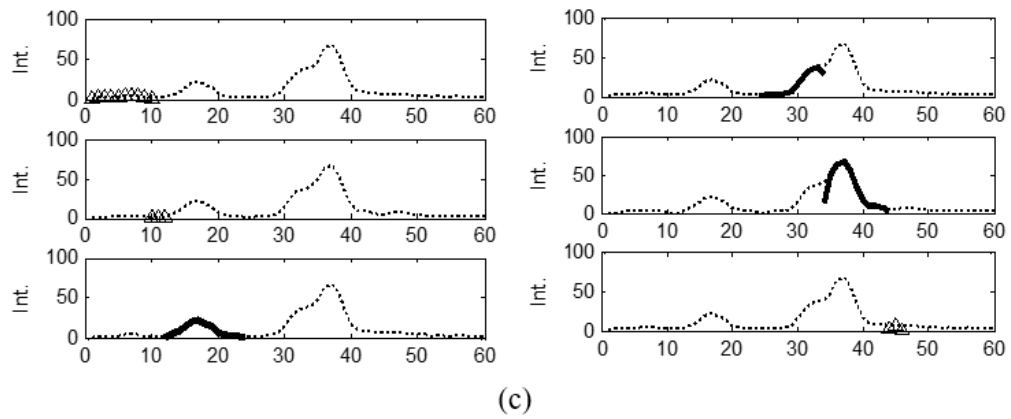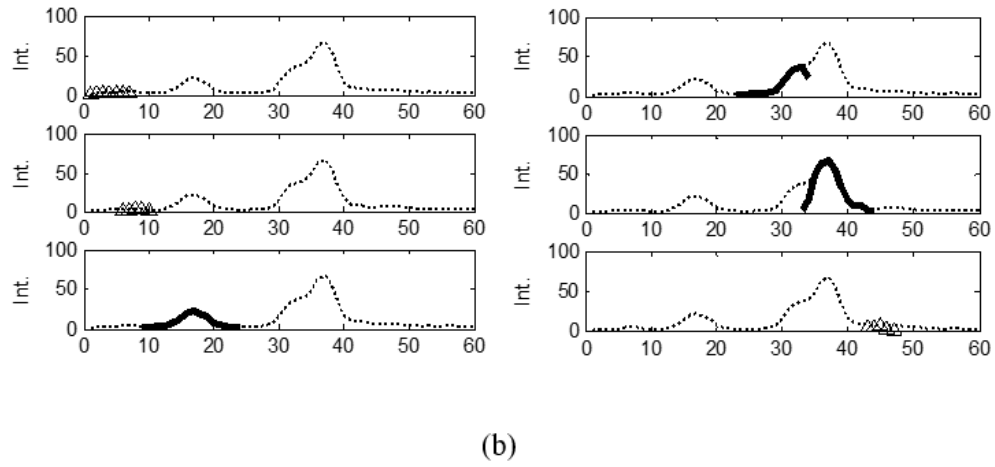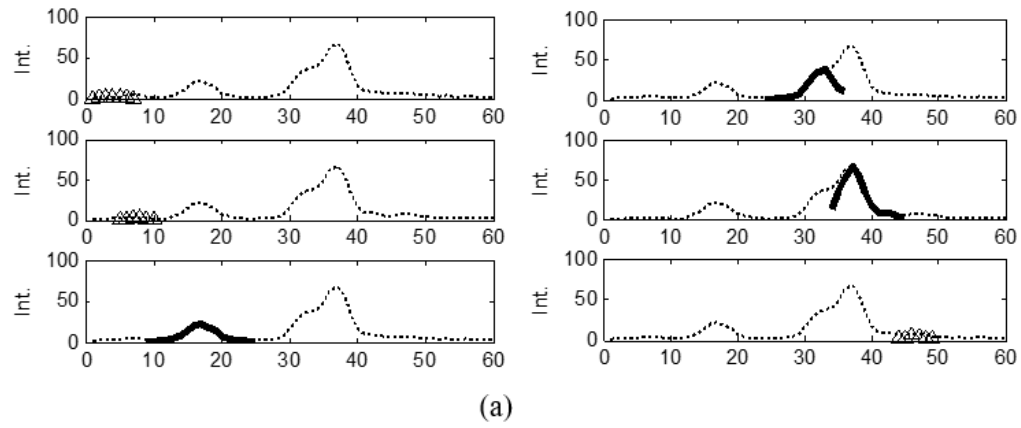
Fig. 5.3. Waveform decomposition examples with (a) rectangle kernel; (b) Gaussian kernel; (c) triangle kernel.

bell-shaped or second order waveform component so that a meaningful peak can exist, the bandwidth should satisfy $h \geq 3$, i.e. a waveform component should have minimum three data points; (2) the bandwidth also determines the minimum separable distance between targets in ranging by $\Delta r = h \times c \times \Delta t/2$, where Δr is the minimal separable distance, c is the speed of light, and $\Delta t = 1$ns is the sampling time interval. We let $\Delta r \leq 0.5$m, which leads to $h \leq 2\Delta r/(c \times \Delta t) = 3.33$; (3) an inappropriate small bandwidth may mistakenly generate artifacts. Combing all above considerations, h =3.3 is chosen.

Cautions should be taken when waveforms are stretched by the high slope of the terrain and the multipath effect. Below, we address this phenomenon by demonstrating the decomposition result of one such broadened waveform. The original waveform is illustrated in Fig. 5.2(d) and as dash-lined in Fig. 5.4. Its decomposition results under two different bandwidths are also shown in Fig. 5.4. The plot plates in Fig. 5.4 are ordered horizontally and plots within each plate are ordered vertically. It depicts the time sequence the clusters are found through the FMS algorithm. Different cluster types are shown in different line styles. In Fig. 5.4(a), a bandwidth $h=2.6$ yields 16 waveform components, among which four are informative (in solid lines) and 12 non-informative (star lines). Apparently, the algorithm mistakenly generates false components for this waveform. A more realistic decomposition result can be obtained when $h=3.3$, as is shown in Fig. 5.4(b). It is noticed that adjacent clusters often overlap, i.e., one waveform data point can belong to more than one cluster, as suggested by the principle of the FMS clustering approach.

5.3.4   FMS Clustering

The position of the initial point x_0, as described in Section 5.2, does not affect the decomposed result. We start the FMS algorithm from $t_0 = 1$. The algorithm moves towards right until the mean-shift vector equals to zero. All the points visited during the moving process are plotted as stars, as shown in the upper-left plot in Fig.

(a)

(b)
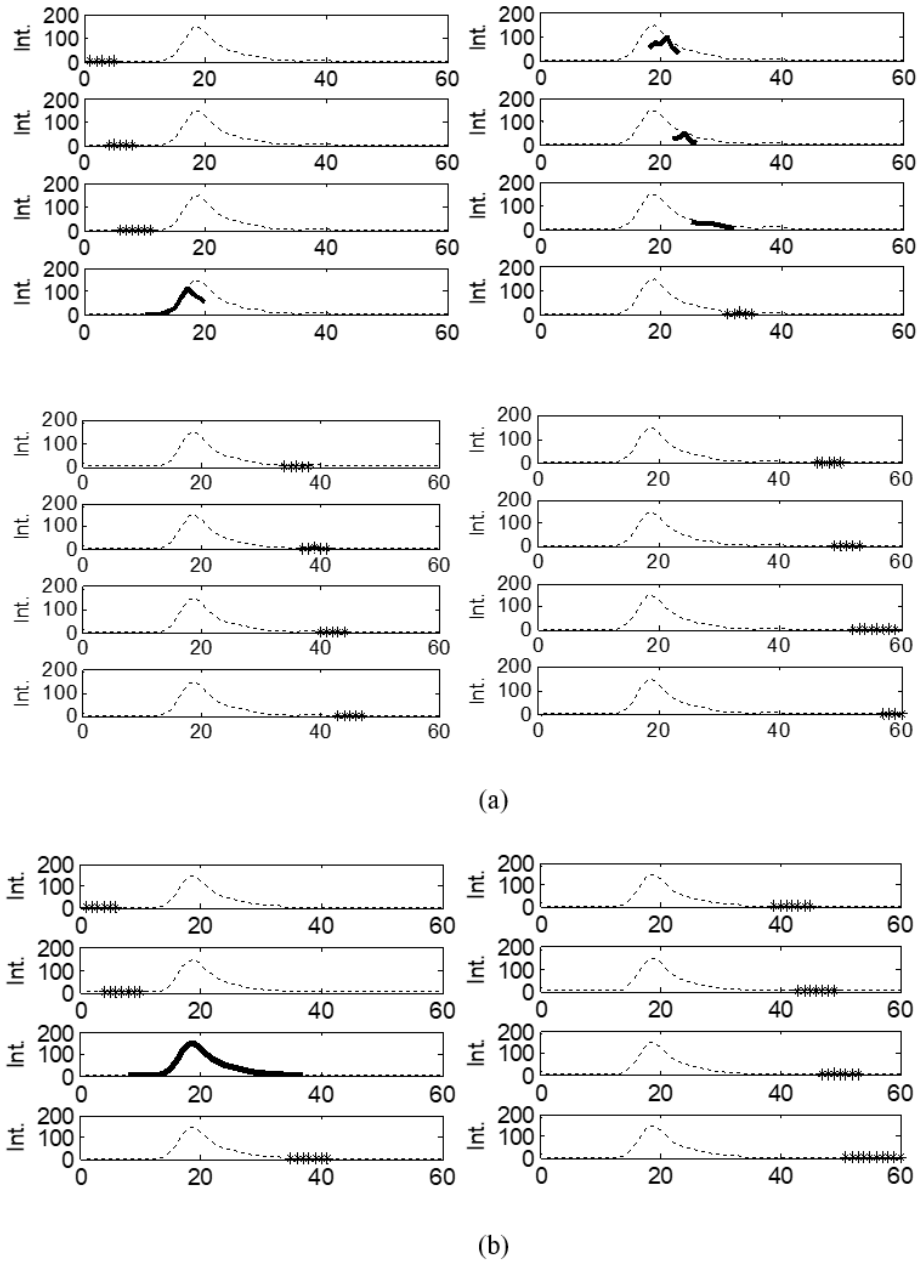
Fig. 5.4. Effects of the bandwidth of the kernel function on waveform #8267 (Fig. 5.2(d)) decomposition. (a) an inappropriately small bandwidth h=2.6 wrongly leads to four (4) informative clusters and 12 non-informative clusters; (b) a proper bandwidth h=3.3 correctly leads to one (1) informative cluster and seven (7) non-informative clusters.

5.5. FMS then restarts from the left most point of the remaining points and finds out the other clusters. We can see that there is overlap between the adjacent clusters because the point in the overlapped area contributes to the mean-shift vectors for both clusters. As an example, the decomposed waveform (#8269) is illustrated in Fig. 5.5. There are altogether eight clusters (components) as plotted in stars or solid lines. The informative (useful signal) and non-informative (noise) clusters can be distinguished by setting a threshold on the cluster size N_i in (5.4), which is chosen as 100 in this study. The informative clusters (size ≥ 100) are plotted in solid lines and the non-informative ones (size < 100) in stars.
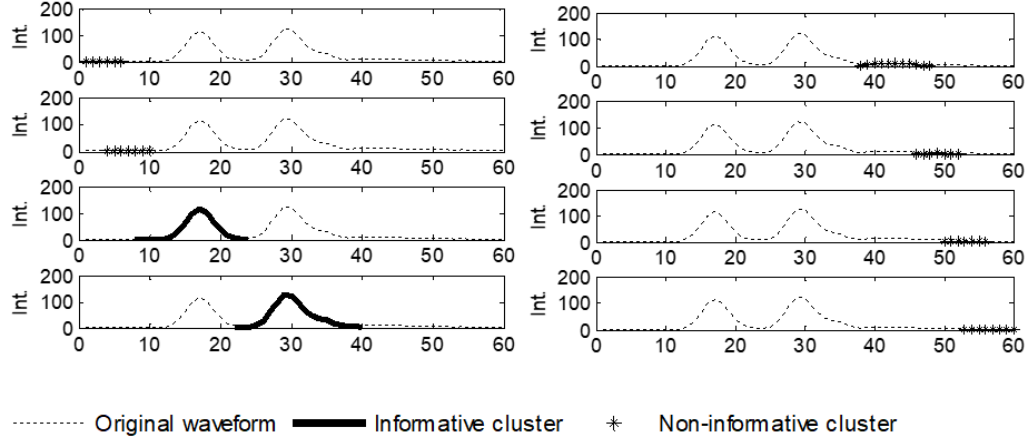
Fig. 5.5. Waveform decomposition and noise floor filtering on wave-form #8269 with the FMS method. There are eight (8) components found, starting from the upper left ordered in vertical direction first.

Decomposing a waveform where mixture exists is the most meaningful use of waveform decomposition. Here, we illustrate another example of FMS applied on such case. The original waveform is plotted in Fig. 5.6(a). There may be three waveform components, one isolated and two mixed, as would be suggested by the EM algorithm. The FMS algorithm returns the decomposed results in Fig. 5.6(b-d). The mixed component is plotted in solid bold lines in Fig. 5.6(c). Each component could be fine-tuned by applying a threshold on the intensities so that only the points above the threshold are utilized to generate the point clouds. Since the waveform

is decomposed, the threshold will be much lower than the one used in traditional pre-filtering. There are nine waveform components found by the FMS method; their weighted sum will be the original waveform.
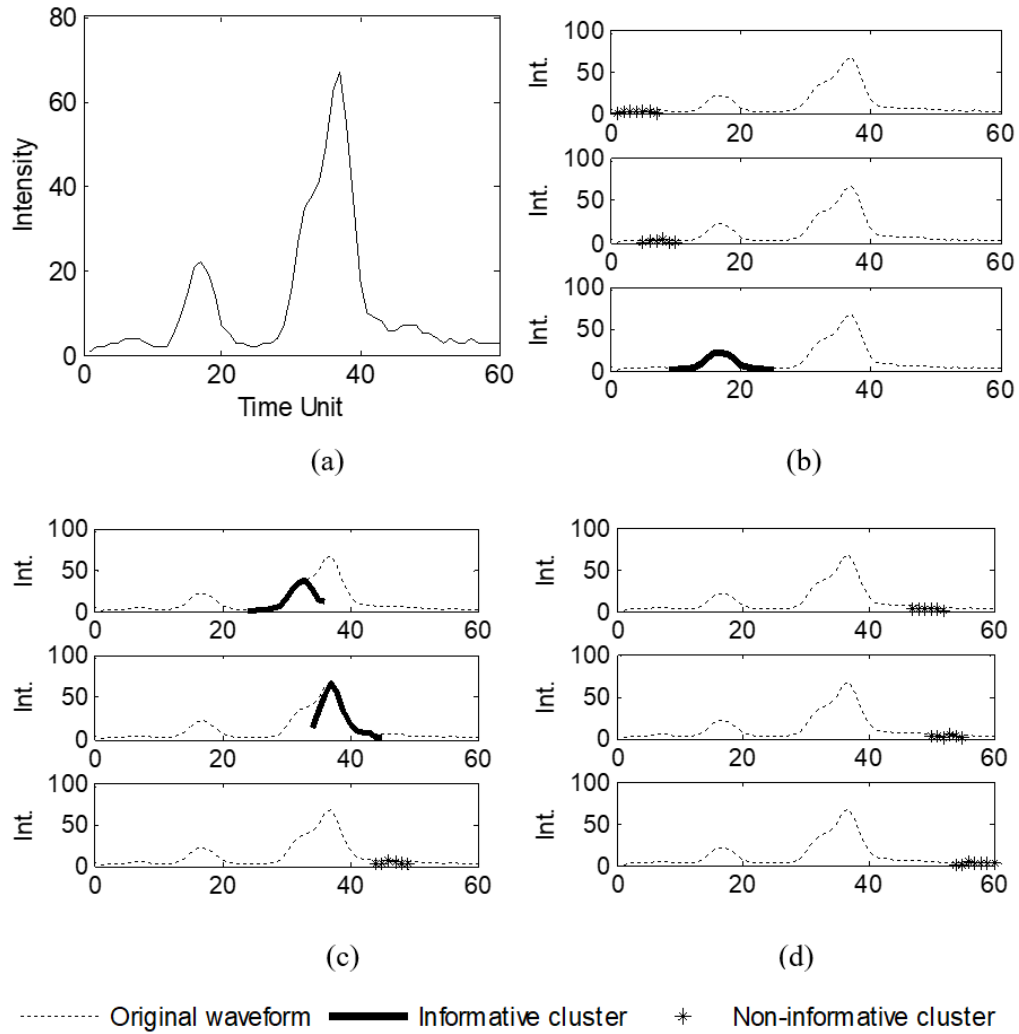
Fig. 5.6. FMS decomposition of a waveform where the mixtures exist: (a) the waveform; (b-d) the decomposed components.

5.4   Comparison of Parametric and Nonparametric Approaches

In this section, we evaluate the effectiveness of the parametric and nonparametric approaches on decomposing lidar waveforms with both simulated and real data. Firstly, GMM is used to simulate lidar waveforms. Then we apply both EM and FMS to decompose the simulated waveforms. Finally, we use both algorithms to analyze a real airborne lidar dataset.

5.4.1   Experiment with Simulated Data

We simulated lidar waveforms under the assumption of GMM since it is widely accepted in many waveform decomposition algorithms. In the simulation, J, μ, σ and w were given and the waveforms were generated according to

$$y\left(t\right) = \sum_{j=1}^{J} w_j \cdot y_j\left(t\right) = \sum_{j=1}^{J} w_j \cdot \exp\left[-\frac{\left(t - \mu_j\right)^2}{2\sigma_j^2}\right] \tag{5.10}$$

Two representative waveforms are illustrated in Fig. 5.7. There are, respectively, one (a) and two (b) Gaussian component(s) in the waveforms. The solid lines are the simulated waveforms and the dashed lines the Gaussian components. Each Gaussian component corresponds to an object detected by the lidar sensor, hence a point in the point cloud. The positions of the Gaussian components are marked as "+". The position estimates are used to calculate the ranges between the detected objects and the lidar sensor.

Firstly, we studied the case where J=1 with an experiment. In this case, there is only one single Gaussian component in the waveform. We generated 15 Gaussian waveforms, each at a random position with widths ranging from 3 to 10 in 0.5 increments. Next, we used EM and FMS to estimate the position of the waveform component. Since EM already assumes GMM, it directly estimates the Gaussian mean as the unknown position. On the other hand, FMS has no knowledge on the shape of the waveforms. It outputs the clustering result where each cluster is regarded
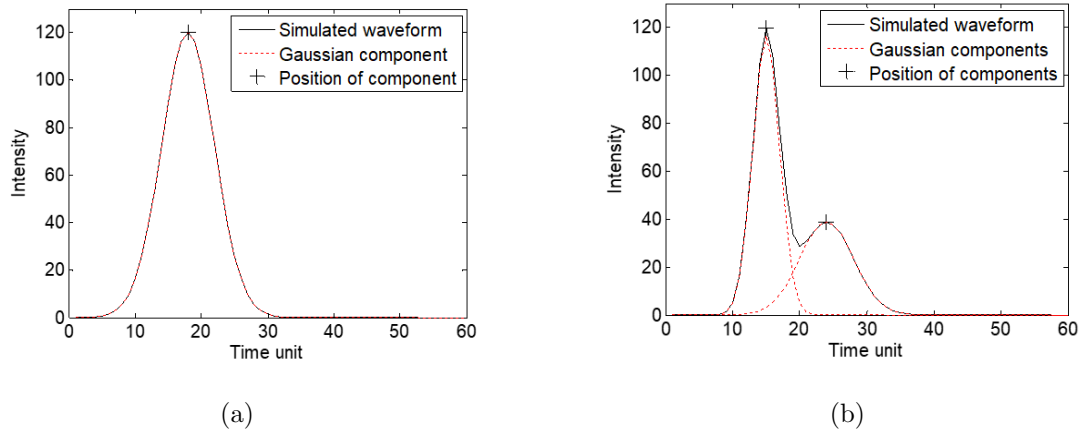
Fig. 5.7. A simulated lidar waveform with (a) one Gaussian component; (b) two Gaussian components.

as a waveform component. The position can be calculated by the mean or peak of the cluster. At this stage, we used both the cluster mean and peak indicated as NMM1 and NMM2 respectively to estimate the position. The estimation error is measured by $e = |\mu - \hat{\mu}|$, where μ and $\hat{\mu}$ are the position of the simulated Gaussian component and the estimated value, respectively. The errors from different approaches are summarized in Fig. 5.8.
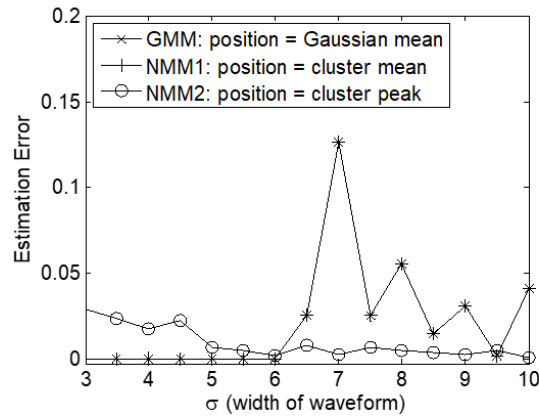
Fig. 5.8. EM and FMS comparison on simulated waveform with one Gaussian component.

In this experiment, NMM1 returned identical results with GMM. Compared with NMM2, the estimation error of NMM1 is higher and less stable for waveform widths greater than 6. Since real lidar waveforms often have a large variation on width, NMM2 should be a better solution than NMM1. In the following experiments, we exclusively used cluster peak in NMM to estimate the position of the waveform components.

In the second experiment, we generated a sequence of waveforms, each with two Gaussian components. The following cases were studied:

- The distances between the two components were varied, while their variances and weights were fixed.

- The variance of one waveform component was changed while other parameters were fixed.

- The weights of the two components were varied while their position and variance were fixed.

We generated 10 waveforms for each case. The results with GMM and NMM (cluster peak as the position) are presented in Fig. 5.9. In the figures, component 1 and 2 are the first and the second waveform components received by the sensor. For each component, the estimation error with GMM and NMM is plotted. The values of fixed parameters are also listed in the caption.

In Fig. 5.9(a) and (b), the estimation error decreases as the distance between the two components increases and the width of the component decreases. It can be explained by the fact that the two components are more separable in such cases. In Fig. 5.9(c), the estimation error of NMM decreases as the weight of the first waveform component rises. It conforms to the fact that we ran the mean-shift algorithm from the first component. In all three plots, we find that the estimation error returned by GMM has larger variation than NMM. Finally, in most scenarios, the estimation error with either model is lower than 0.4. For a lidar system with a sampling rate of one nanosecond, such estimation error will introduce a range error of less than 6cm.
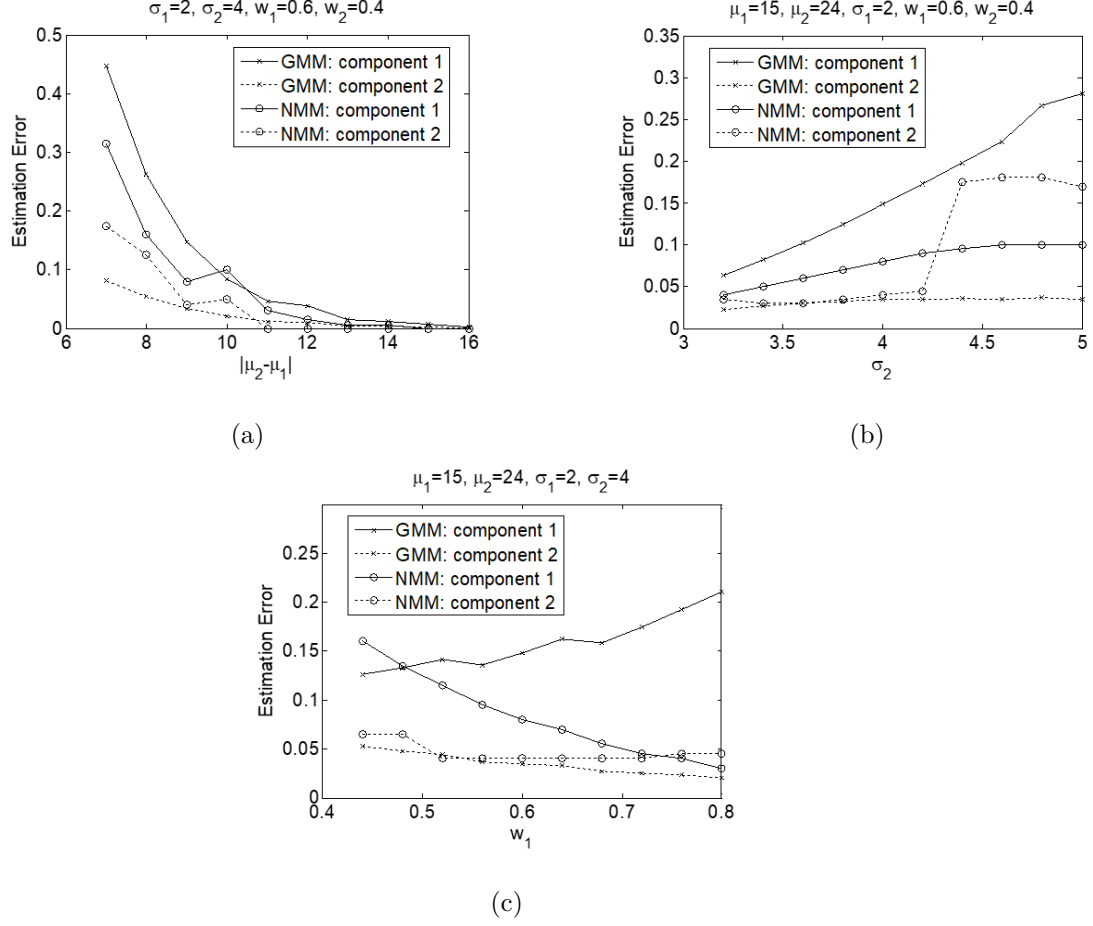
Fig. 5.9. Estimation error of GMM and NMM along (a) the distance between waveform components; (b) the width of a waveform component; (c) the weight of waveform components.

5.4.2 Experiment with Real Lidar Data

The study of algorithm comparison needs the knowledge of ground truth to some extent. The number of waveform components J may be obtained even without on-site investigation. For example, the emitted lidar signal is directly reflected by bare ground or building roof so that a single waveform component is expected in the returned waveform. In other scenario such as forests and grasses, the footprint of the lidar signal may cover multiple targets such as leaves, trunks and ground. The returned waveform could be either a single component or multiple components. As

is shown in Fig. 5.10., the whole experimental dataset is mainly composed of two classes: bare ground and forest. For bare ground, the emitted lidar signal is directly reflected by the around surface so that a single waveform component is expected in the returned waveform. For forest, the footprint of the lidar signal may cover multiple targets such as leaves, trunks, and ground. The returned waveforms could be either a single component or multiple components. In other words, the number of waveform components (J) is known to be 1 for the bare ground, but unknown for the forest area. For this reason, we performed our tests on the bare ground area only.

Fig. 5.10. The bare ground in: (Left) World Imagery of Esri, where the $10 \times 10m^2$ study area is highlighted in red; (Right) Google EarthTM Digital Globe image, where the locations of two waveform examples are marked with blue pin icons.

We selected a $10 \times 10m^2$ area from the bare ground as highlighted in Fig. 5.10(a). There are altogether 5,031 waveforms in the area, so the waveform/point density is 50 per square meter. Two waveform examples are selected to study in the following experiments as pinpointed in Fig. 5.10(b). In the experiment, we didn't use the estimation error to evaluate the algorithms since the ground truth was not available at the time of the experiment. Instead, we checked the residuals between the original

waveform and the reconstructed waveform from EM or FMS. Also, we visually checked the fitness of the two approaches.

The decomposition results of two example waveforms are plotted in Fig. 5.11. First, it is noted that the original lidar waveforms have a noise floor that is not introduced in the simulated waveforms (Fig. 5.7). Such noise may be generated by the sensor, atmosphere, or sampling, and they are inevitable in real lidar data. For EM, a threshold pre-filtering was applied to remove the noise. FMS classifies such noises as non-informative clusters and removes them after waveform decomposition.

In both Fig. 5.11(a) and (b), the decomposition results from EM is plotted on the left and the results from FMS is on the right. It can be observed that the lowest intensity of the EM decomposed component is 20, which is equivalent to the threshold in the pre-filtering process. The Gaussian component from EM obviously deviates from the original waveform, meaning that the assumption of GMM doesn't hold in
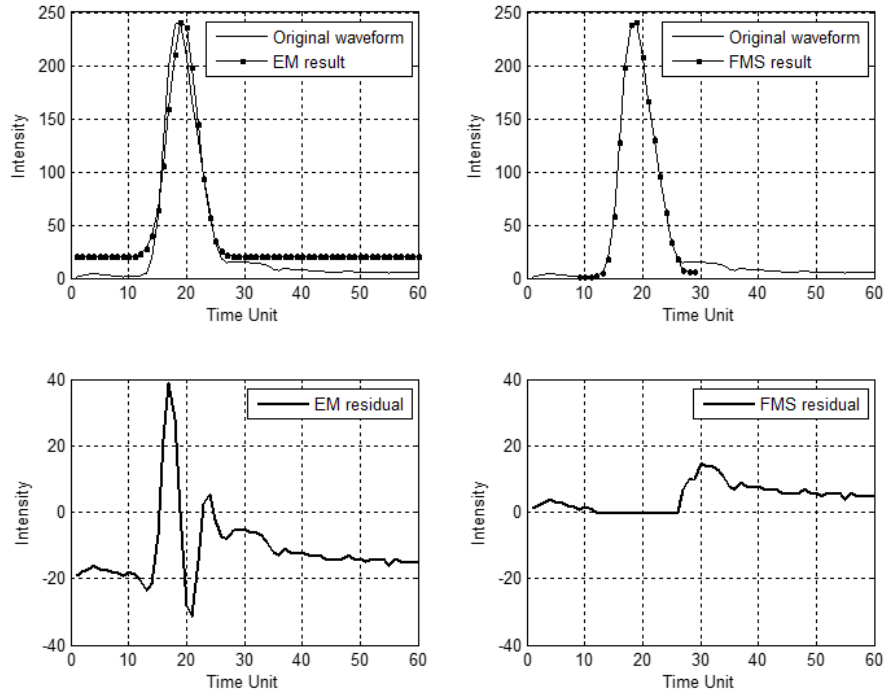
(a)
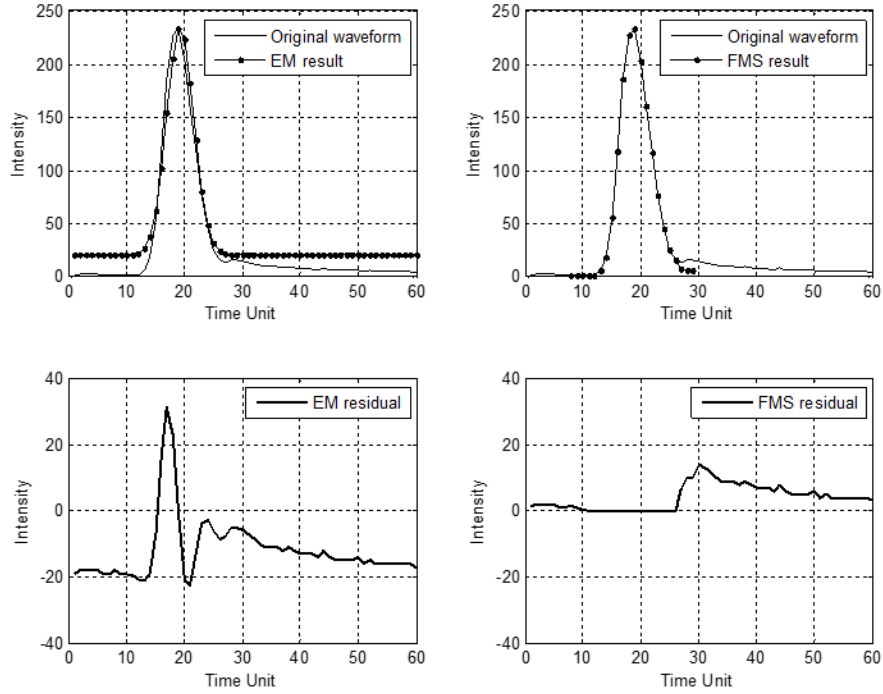
(b)

Fig. 5.11. Decomposition result of (a) waveform #1170908, and (b) waveform #1073866. The results with GMM are plotted on the left and that with NMM on the right.

this situation. As a result, the difference between the residuals of the two sides of the main component is more than 40. Increasing the number of the Gaussian components may reduce the residual deviation. However, it will generate more than one point on the ground, contradicting the fact that such waveforms are returned from the bare ground. On the right, the results from FMS are plotted. The waveform components fit the original waveforms well because most part of the signal falls into the main cluster. The residual of the informative component has the intensity in the range 0-15. Such residuals are clustered as non-informative clusters and removed thereafter. The two waveform examples are quite representative in our dataset. We ran EM on all the waveforms (5,031 in total) in the $10 \times 10m^2$ study area. For each waveform,

we refer to the residual on the left side of the peak position as $Residual_{left}$, and the residual on the right side as $Residual_{right}$. The histogram of the residual difference, $Residual_{left} - Residual_{right}$, is shown in Fig. 5.12. Among all waveforms, 1,907 have a residual difference greater than 35. We conclude that the fitness of GMM is quite limited in the dataset.
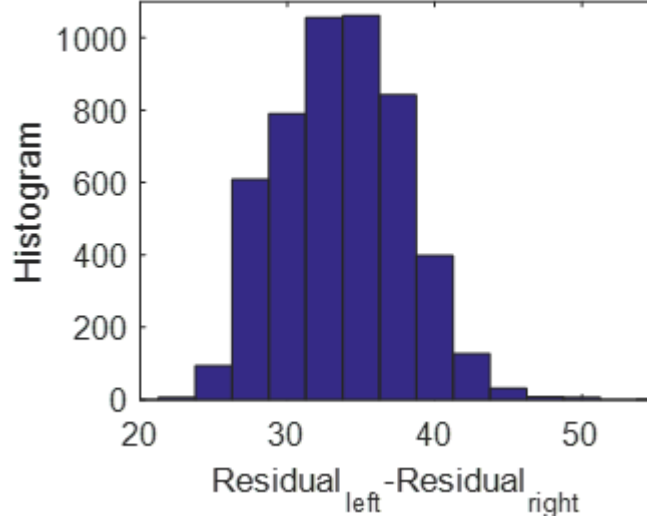
Fig. 5.12. Histogram of difference of EM residual.

5.4.3 Comparison of Computation Time

We ran both EM and FMS for the entire data and extracted the ground points using a filter implemented in the LAStools (http://rapidlasso.com/) software. It uses a variation of the Axelsson's (Axelsson, 2000) triangulated irregular network (TIN) refinement algorithm that avoids some of the trigonometry overhead. We used the default parameter settings to filter the point clouds resultant from the FMS and EM, respectively. The number of points and computing time of both EM and FMS are summarized in Table 5.1.

Notice from Table 5.1 that the ground point density after filtering is 1.5 (EM) and 1.6 (FMS) points per square meter, respectively. Both are suitable to generate

Table 5.1.
Number of points generated by waveform decomposition and the subsequent ground filtering

		EM with GMM	FMS with NMM	FMS/EM
Decomposition	Total CPU Time (sec.)	498,052.85	170,349.52	0.34
	CPU Time per waveform (ms.)	10.0	3.4	0.34
	#total points	112,769,843	115,543,824	1.02
	#points/sq. m	21.9	22.4	1.02
Filtering	#ground points	7,817,965	8,208,448	1.05
	#ground points/sq. m	1.5	1.6	1.05

(All computations were completed on a Dell Precision workstation with 8-core 3.7GHz CPU and 16GB memory.)

a DEM at one-meter resolution. DEMs at a resolution of 1 meter were then created with ArcGIS 10.3.1. The ground elevation of the DEM ranges from 422 to 1,008 meters.

5.4.4 DEM Comparison

Since one of the applications for waveform decomposition is to create digital elevation model (DEM) using the waveform-generated discrete point clouds, we generated DEMs with ground points obtained from both approaches. As shown in Fig. 5.12., hillshading of six 195×230 m^2 sites in the study area were selected to highlight the terrain details from the two decomposition methods. Circles of solid and dashed lines are respectively used to label locations of apparent artifacts in the EM and FMS results. As a general observation, the two DEMs have comparable qualities. Both can satisfactorily reflect the terrain morphology and almost all topographical details. On the other hand, both results have a few noticeable small scale pits. These artifacts, both in size and in number, are actually minimal, considering the fact that the terrain is under heavy canopy. Examining the hillshading in a closer view, the FMS approach created slightly fewer artifacts (Site 2, 3, 5 and 6) than EM. It should be noted that the artifacts in both DEMs were likely introduced by imperfect filtering. As many studies reported (Mücke et al., 2013; Langridge et al., 2014; Lin et al., 2013), high quality DEM generation under dense forest canopy is still a challenging task for lidar data processing.

As a primary study to the vertical accuracy of the resultant FMS DEM, its hillshading is stacked over the USTopo (ground) in Fig. 5.14. The waveform DEM significantly reveals more detailed terrain features. For example, a road under the forest can be successfully detected in the waveform DEM, whereas it is not visible in the NED 1/3" DEM, which has a resolution of approximate eight (8) meters. The pixel by pixel differences between the two DEM's show a very good normal distribution with a mean of 0.89 meters and a standard deviation of 6.99 meters. This result
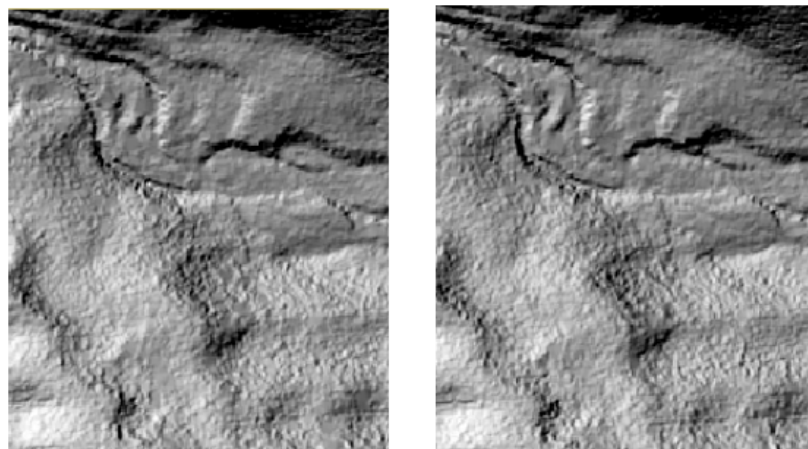
Site 1
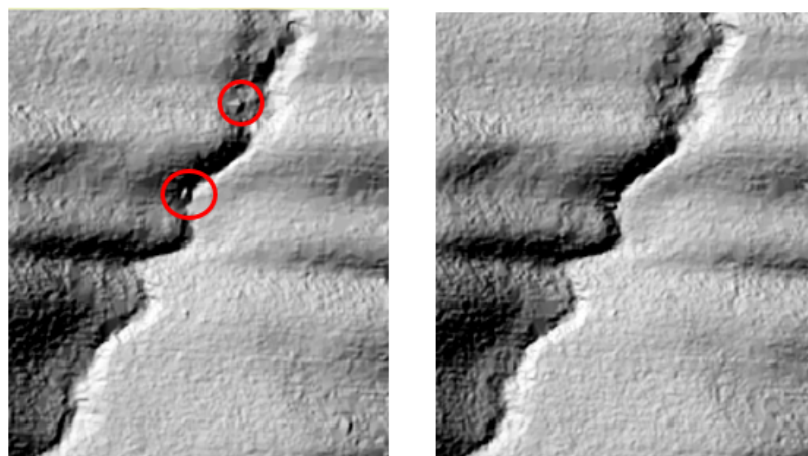
Site 2
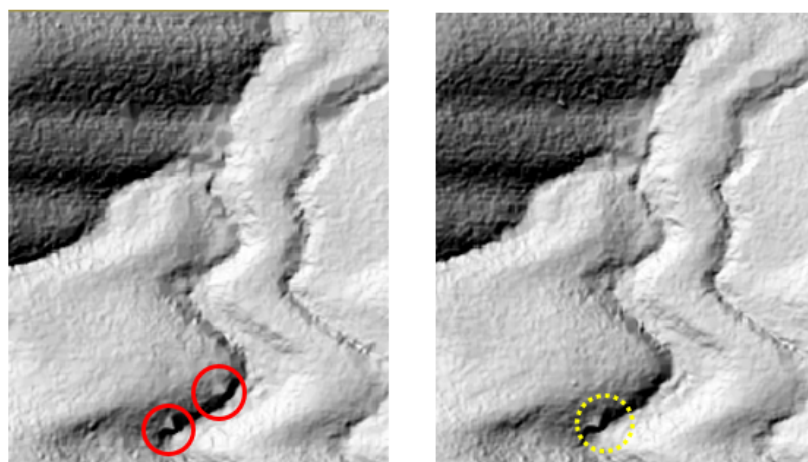
Site 3
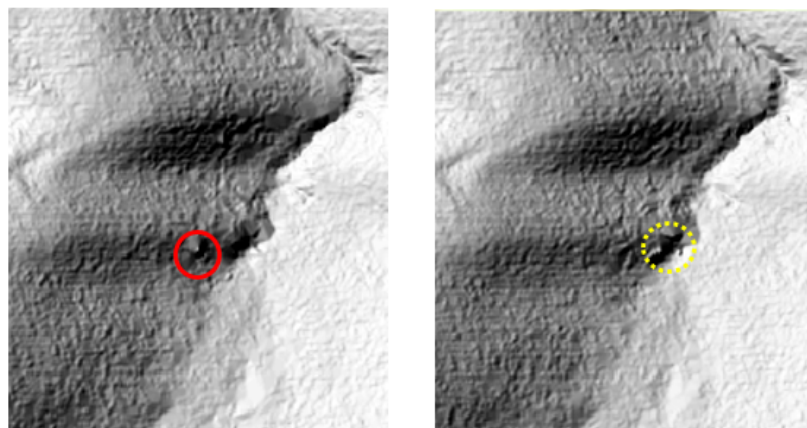
Site 4
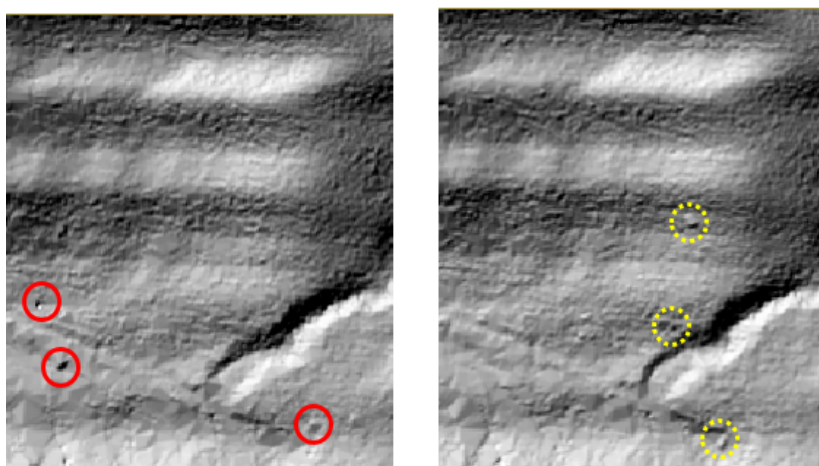
Site 5
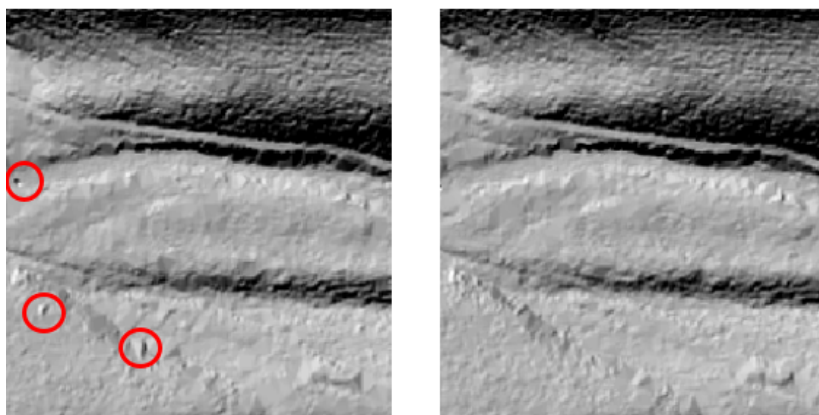
Site 6

Fig. 5.13. Hillshading of six (6) DEM samples ($195{\times}230$ m^2) generated by EM (left) and FMS (right).

basically shows that there is no significant systematic bias existing in our waveform DEM. According to the specification of this NED 1/3" DEM dataset, it was from compilation of the NED 1" DEM, which has a nominal vertical accuracy of 7.0 meters. Other topographic features, including ridges, valleys, gullies are also clearly presented. On the other hand, suspicious striping effect in west-east (perpendicular to the flight) direction is noticed. Such artifacts are caused by the unsynchronized time between the GPS and the laser scanner, which will be discussed and corrected in next chapter.
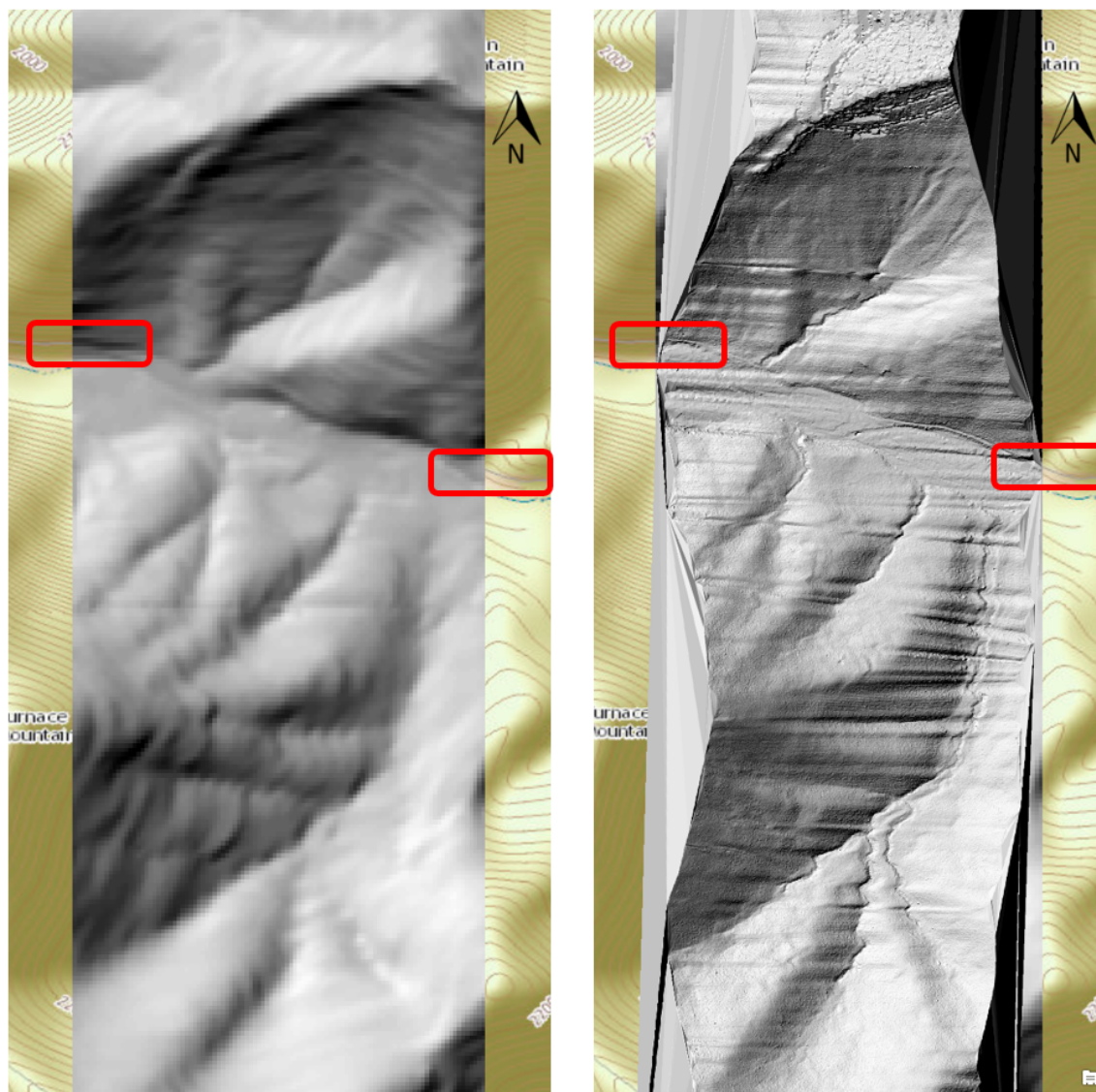
Fig. 5.14. Hillshading generated from NED 1/3" DEM (left) and FMS DEM (right). A road should exist as indicated by the red boxes. Many fine topographic features are also clearly visible in FMS DEM. The background map is USTopo map. The size of this area is about 770 m wide and 2,600 m tall.

6. GEOREFERENCING AND SELF-CALIBRATION

Georeferencing is the process by which the 3-D points in the laser scanner coordinate system are transformed into the 3-D points in the mapping coordinate system. Both the POS measurements and the relative position and orientation between the onboard components of lidar, IMU, and GPS antenna will be utilized in the transformation.

In most cases, the laser scanner and the POS are independent units from different manufacturers. The accuracy of the georeferenced data is dependent on synchronization and calibration of the lidar and POS. During the process of georeferencing, calibration means determination of the exterior orientation described by boresight misalignment angles in roll, pitch, and yaw (Shan and Toth, 2018). Ground control points (GCP), boresight flight plan, and multiple flight strips with overlap are commonly required for the conventional calibration methods.

In this chapter, we first use the POS measurements to directly georeference the lidar data. Then the problem of calibration will be studied. We develop a framework of self-calibration that calibrates the boresight angles and performs precise georeferencing at the same time. The method is based on a single strip of data without GCP or a special flight plan.

6.1   Model

6.1.1   Georeferencing

The purpose of georeferencing is to transform the target's coordinate from the laser scanner's frame to the mapping frame. This process can be described as

$$\mathbf{r}^m_{target}(t_S,\ t_{IMU}) = \mathbf{r}^m_{platform}\left(t_{IMU}\right) + \mathbf{R}^m_H\left(t_{IMU}\right) \cdot \mathbf{R}^H_{IMU}\left(t_{IMU}\right) \cdot \mathbf{R}^{IMU}_S \cdot \mathbf{r}^S_{target}\left(t_S\right) \quad (6.1)$$

where

- $\mathbf{r}_{target}^{m}(t_S,\ t_{IMU})$ and $\mathbf{r}_{target}^{S}(t_S)$ are the coordinates in the mapping frame and the laser scanner's frame, respectively,

- $\mathbf{r}_{platform}^{m}(t_{\text{IMU}})$ is the position of the lidar platform, and

- $\mathbf{R}_{H}^{m}(t_{\text{IMU}})$ and $\mathbf{R}_{IMU}^{\text{H}}(t_{\text{IMU}})$ are the transformation matrix between the different coordinate systems.

In (6.1), there are two sets of variables that need to be resolved in the process of calibration. The first one is the time misalignment $\Delta t = t_S - t_{IMU}$, where t_S and t_{IMU} are the clock time of the laser scanner and the POS unit, respectively. A synchronized system assumes $\Delta t = 0$; otherwise, Δt should be determined during the calibration process. The second set of parameters is the boresight angles ($\delta\omega$, $\delta\phi$, $\delta\kappa$) in the time-invariant matrix $\mathbf{R}_{S}^{IMU}$. In the initial stage of direct georeferencing, these angles are assumed to be known, often either 0 or 90 degrees depending on the specific definition of the onboard coordinate frames.

There are several different coordinate frames in the airborne lidar system. The origin of the entire lidar platform is also called the origin of the body frame. Riegl USA recommends the laser scanner be the reference point of the IMU navigation coordinate frame so the origin of the scanner frame is also the origin of the body frame of the lidar system. Specifically, in our experiment, the x axis of the lidar frame points to the nadir direction of the aircraft, the y axis is the flight direction, and z axis is wing-to-wing direction of the airplane. On the other hand, the x axis of the IMU frame points to the nadir direction of the aircraft, the y axis is the flight direction, and z axis is wing-to-wing direction of the airplane. See Fig. 6.1. for illustration.

From the laser scanner's coordinate system and the IMU coordinate system in Fig. 6.1., the time-invariant conversion matrix between the two coordinate systems, $\mathbf{R}_{S}^{IMU}$, has the form

$$\mathbf{R}_{S}^{IMU} = \mathbf{M}_{y}^{S}\left(\frac{\pi}{2}\right) \cdot \mathbf{M}_{x}^{S}\left(\frac{\pi}{2}\right),\tag{6.2}$$

top view

Flight direction

front view
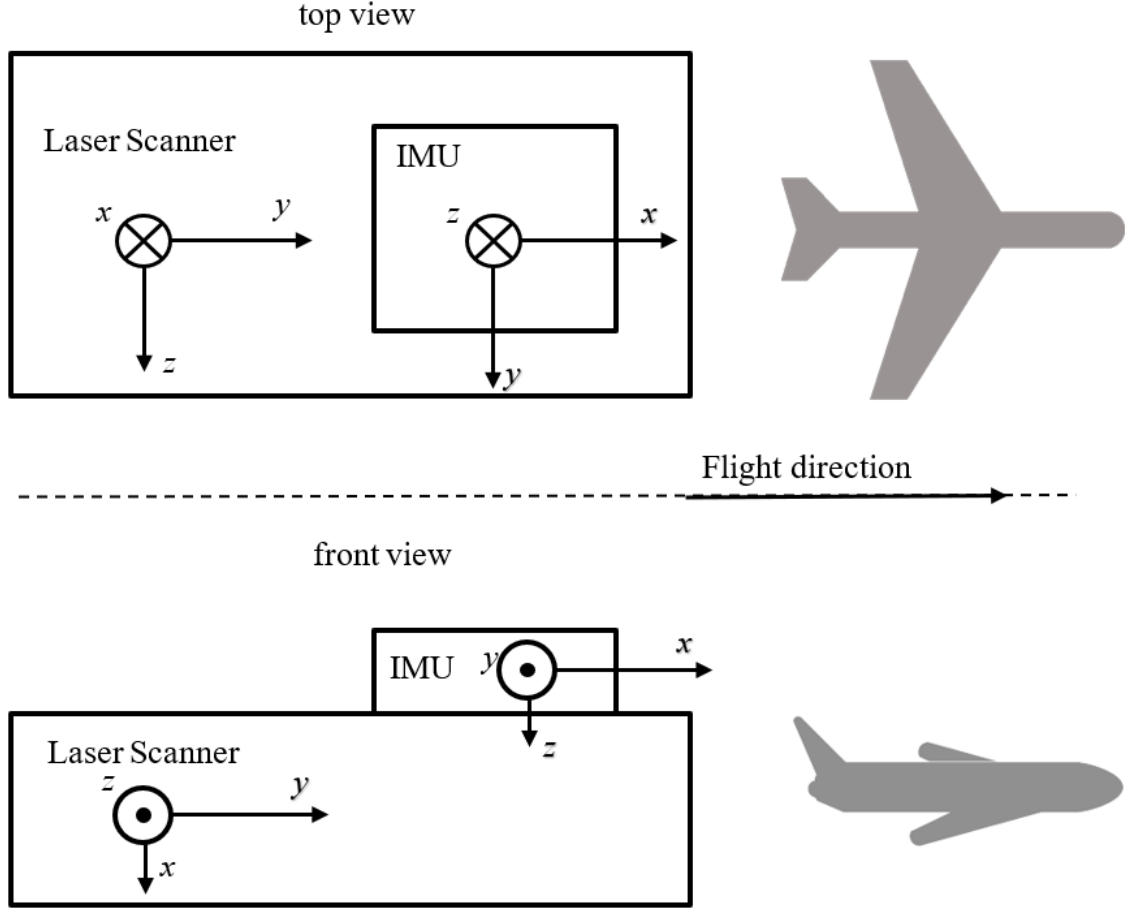
Fig. 6.1. Illustration of the laser scanner's coordinate system and the IMU coordinate system.

where $\mathbf{M}_k^f (\theta)$ represents a rotation in the f frame, along axis k, and with a rotation angle θ, so that

$$\mathbf{M}_y^S \left(\frac{\pi}{2} \right) = \begin{bmatrix} \cos \left(\frac{\pi}{2} \right) & 0 & -\sin \left(\frac{\pi}{2} \right) \\ 0 & 1 & 0 \\ \sin \left(\frac{\pi}{2} \right) & 0 & \cos \left(\frac{\pi}{2} \right) \end{bmatrix} \tag{6.3}$$

$$\mathbf{M}_x^S \left(\frac{\pi}{2} \right) = \begin{bmatrix} 1 & 0 & 0 \\ 0 & \cos \left(\frac{\pi}{2} \right) & \sin \left(\frac{\pi}{2} \right) \\ 0 & -\sin \left(\frac{\pi}{2} \right) & \cos \left(\frac{\pi}{2} \right) \end{bmatrix} \tag{6.4}$$

6.1.2 Self-Calibration with DEM

In practice, the axes of the scanner's coordinate system and the navigation co-ordinate are not parallel. The mounting misalignment angles $\delta\omega$, $\delta\phi$, $\delta\kappa$ (for roll, pitch, and yaw), if available from lab calibration, are used to perform the rotation between these two frames. The rotation matrix for applying the transformation due to the boresight misalignment is as follows:

$$\mathbf{R}_S^{IMU} = \mathbf{M}_x^S\left(\delta\kappa\right) \cdot \mathbf{M}_y^S\left(\frac{\pi}{2} + \delta\phi\right) \cdot \mathbf{M}_x^S\left(\frac{\pi}{2} + \delta\omega\right) \tag{6.5}$$

It is noted that two $\mathbf{M}_x^S\left(\theta\right)$ matrices are applied as the coordinate systems are defined in Fig. 6.1.

Taking the problems of both synchronization and boresight calibration into consideration, the coordinate of the lidar point p is expressed as

$$
\begin{aligned}
\mathbf{r}_{target,\ p}^m &\left(POS_p, WF_p; \theta\right) \\
&= G\left[\left(\mathbf{r}_{platform}^m, \mathbf{R}_H^m, \mathbf{R}_{IMU}^H\right)_p, \mathbf{r}_{target,p}^S ; \left(\Delta t,\ \delta\omega, \delta\phi, \delta\kappa\right)\right] \\
&= \mathbf{r}_{plotform}^m\left(t_{S,p} - \Delta t\right) + \mathbf{R}_H^m\left(t_{S,p} - \Delta t\right) \cdot \\
&\quad \cdot \mathbf{R}_{IMU}^H\left(t_{S,p} - \Delta t\right) \cdot \mathbf{R}_S^{IMU}\left(\Delta\omega,\ \Delta\phi,\ \Delta\kappa\right) \cdot \mathbf{r}_{target,p}^S\left(t_S\right)
\end{aligned}
\tag{6.6}
$$

where $\Delta\omega = \pi/2 + \delta\omega, \Delta\phi = \pi/2 + \delta\phi, \Delta\kappa = \delta\kappa$. t_S is set as the reference time of the lidar system. The georeferencing process $G(\cdot)$ is a one-to-one mapping. It maps each original waveform record, WF_p, and POS record, POS_p, to a unique lidar point $\mathbf{r}_{target,\ p}^m$.

In our work, we propose to use an existing quality ground DEM as the reference. Let $\{\}_N$ denote a set of N lidar points, the objective function is the mean of squared deviation (MSD) between the ground points of lidar and the reference DEM:

$$f_N\left(\theta_G; \theta_g\right) = MSD\left(\left\{r_{target,\ p_{grnd}(\theta_g)}^m\left(\theta_G\right)\right\}_{N_{grnd}(\theta_g)}, \mathrm{DEM}_{ref}\right) \tag{6.7}$$

In (6.7), $\{r_{target,\ p_{grnd}(\theta_g)}^m\left(\theta_G\right)\}_{N_{grnd}(\theta_g)}$ is the set of $N_{grnd}\left(\theta_g\right)$ ground points. They are obtained by applying a waveform filtering in the following way. First, the entire N lidar points $\{r_{target,\ p}^m\left(\theta_g\right)\}_N$ are generated with θ_g. A traditional ground filter, as is

described in Chapter 5, classifies the points as "ground" and "non-ground". Since the georeferencing is one-to-one, the original waveform data $\{\mathbf{r}^S_{target,p}\}_N$ and POS data $\left\{\left(\mathbf{r}^m_{platform}, \mathbf{R}^m_H, \mathbf{R}^H_{IMU}\right)_p\right\}_N$ will also be labelled. Finally, the original waveform and POS data that are labeled as "ground", $\left\{(WF,\ POS)_{p_{grnd}(\theta_g)}\right\}_{N_{grnd}(\theta_g)}$, will be extracted to generate a set of new ground points under θ_G.

With waveform filtering, the coordinates of the ground points and the selection of those points may come from different parameters θ_G and θ_g. When $\theta_g \approx \theta_G$, the filtering results are equivalent, so that

$$\{p_{grnd}(\theta_g)\}_{N_{grnd}(\theta_g)} = \{p_{grnd}(\theta_G)\}_{N_{grnd}(\theta_G)} \tag{6.8}$$

Such assumption doesn't hold if θ_g and θ_G are far away from each other because the geometry and relative position between the lidar points may change significantly and the filtering results vary.

The classification error introduced by the ground filtering will inevitably affect the objective function. Let the true ground points be $\{r^m_{target,\ p_{grnd}}\}_{N_{grnd}}$; the estimated ground points in (6.7) can be expressed as

$$
\begin{aligned}
&\{r^m_{target,\ p_{grnd}(\theta_g)}(\theta_G)\}_{N_{grnd}(\theta_g)} \\
&= \{r^m_{target,\ p_{grnd}}(\theta_G)\}_{N_{grnd}} \\
&\quad - \{r^m_{target,\ p^{\epsilon 1}_{nongrnd}(\theta_g)}(\theta_G)\}_{N_{\epsilon 1}(\theta_g)} + \{r^m_{target,\ p^{\epsilon 2}_{grnd}(\theta_g)}(\theta_G)\}_{N_{\epsilon 2}(\theta_g)}
\end{aligned}
\tag{6.9}
$$

where

- $\{r^m_{target,\ p^{\epsilon 1}_{nongrnd}(\theta_g)}(\theta_G)\}_{N_{\epsilon 1}(\theta_g)}$ is the set of ground points that are mistakenly classified as non-ground points by applying the ground filter.

- $\{r^m_{target,\ p^{\epsilon 2}_{grnd}(\theta_g)}(\theta_G)\}_{N_{\epsilon 2}(\theta_g)}$ is the set of nonground points that are mistakenly classified as ground points by the ground filter.

Both $N_{\epsilon 1}(\theta_g)$ and $N_{\epsilon 2}(\theta_g)$ are variables of θ_g. The optimization strategy should take consideration of the impact of this fact.

6.2 Solution

With the function (6.7), the process of self-calibration can be modeled as an optimization problem of minimizing the objective function $f_N(\theta_G; \theta_g)$:

$$
\begin{aligned}
\theta_G^* &= (\Delta t, \delta\omega, \delta\phi, \delta\kappa)^* \\
&= \underset{\theta_G}{\text{argmin}} \ f_N(\theta_G; \theta_g) \\
&= \underset{\theta_G}{\text{argmin}} \, MSD\left(\{r_{target,\, p_{grnd}(\theta_g)}^m(\theta_G)\}_{N_{grnd}(\theta_g)}, \mathbf{DEM}_{ref}\right)
\end{aligned}
\tag{6.10}
$$

The self-calibration process is the procedure of solving the optimization problem of (6.10). It consists of three steps: initial optimization, synchronization, and boresight calibration. A heuristic optimization will be applied in the initial calibration. After a relatively small searching area around the optimal solution is located by the initial optimization, a fixed set of ground points will be chosen in the objective function. A fine optimization can be then conducted in the subsequent steps.

6.2.1 Heuristic Optimization

In the initial stage of optimization, the initial value θ_0 may be far away from the optimum solution. The ground filtering should be conducted whenever θ changes to avoid the classification errors introduced by the unsynchronized data and the misaligned boresight angles. In such case, the filtering process is equivalent to a conventional ground filter that directly works on the lidar points. The objective function becomes

$$
f_N(\theta_G; \theta_G) = MSD\left(\{r_{target,\, p_{grnd}(\theta_G)}^m(\theta_G)\}_{N_{grnd}(\theta_G)}, DEM_{ref}\right)
\tag{6.11}
$$

A consideration of (6.11) is that the set of the estimated ground points, $N_{grnd}(\theta_G)$ will change as θ_G changes. This will in turn affect the objective function. Therefore, the problem becomes non-convex and cannot be solved by a gradient-based searching algorithm.

We utilize a heuristic optimization method of particle swarm optimization (PSO) (Kennedy, 1995; Golbon-Haghighi, M.H., et al., 2018) to optimize the objective function $f_N(\theta_G; \theta_G)$. The basic idea of the particle swarm optimization can be expressed in the following: first, we randomly generate some initial solution candidates such as $\theta_0 = \{\theta_{0,1}, \theta_{0,2}, \ldots, \theta_{0,M}\}$. We define these candidates as population and an individual candidate as a particle. Next, each candidate will evolve according to

$$\Delta\theta_{i+1,d} = w \cdot \Delta\theta_{i,d} + c_1 \cdot r_1 \cdot (\theta_d^* - \theta_{i,d}) + c_2 \cdot r_2 \cdot (\theta_i^* - \theta_{i,d}) \tag{6.12}$$

$$\theta_{i+1,\,d} = \theta_{i,d} + \Delta\theta_{i+1,\,d} \tag{6.13}$$

where

- $\Delta\theta_{*,d}$ is the particle velocity,
- θ_d^* is the best value that the d-th candidate has achieved so far,
- θ_i^* is the best value that is obtained by any particle in the population,
- c_1 and c_2 are constant nunbers of learning factors, and
- r_1 and r_2 are random numbers between 0 and 1.

The "fitness" of a particle is evaluated according to the objective function $f_N(\theta_G; \theta_G)$. The algorithm converges when the best candidate cannot be further improved within a given number of iterations.

In our problem, one of the challenges of particle swarm optimization is that the cost of calculating $f_N(\theta_G; \theta_G)$ for each candidate θ_G could be very high. As is shown in Chapter 5, it takes up to a few hours to obtain the DEM from the raw waveform data. In particle swarm optimization, the number of candidates in each iteration could be as many as a few dozens, and it may need hundreds of iterations before the algorithm converges. From the aspect of time efficiency, it is unwise and unnecessary to evaluate the objective function with all of the lidar points ($N > 50{,}000{,}000$ in our case). Instead, a subset of the entire data will be selected to quickly find out the region in which the optimal solution may exist.

6.2.2 Convex Optimization

After the initial optimization, a searching range is narrowed down to a relatively small region by particle swarm optimization. In this range, $\{p_{grnd}(\theta_{PSO})\} = \{p_{grnd}(\theta_G)\}$ or

$\{r^m_{target,\, p_{grnd}(\theta_{PSO})}(\theta_G)\}_{N_{grnd}(\theta_{PSO})} = \{r^m_{target,\, p_{grnd}(\theta_G)}(\theta_G)\}_{N_{grnd}(\theta_G)}$, so the objective function becomes

$$f_N(\theta_G; \theta_{PSO}) = MSD\left(\{r^m_{target,\, p_{grnd}(\theta_{PSO})}(\theta_G)\}_{N_{grnd}(\theta_{PSO})}, DEM_{ref}\right) \qquad (6.14)$$

Comparing to (6.11), the objective function in (6.14) is evaluated on a fixed set of points $\{p_{grnd}(\theta_{PSO})\}$. Since $N_{grnd}(\theta_{PSO})$ is not varying with reference to θ_G, the selection of the ground points will be stable. To further guarantee the correct convergence of the objective function, the problem of synchronization and boresight calibration are solved separately.

6.3 Data

6.3.1 IMU Measurements

The GPS and the INS are measured at different sampling rate, and they will be integrated and interpolated. At the same time, the integrated results are converted to the laser frame, i.e. the body frame. The conversion requires the knowledge of the two distances between the origin of the body frame and the IMU frame. Specifically, the distance between the GPS antenna and the laser scanner is defined as the GPS lever arm; the distance between the IMU instrument and the laser scanner is the IMU lever arm. In our work, the lever arm measurement and GPS/INS integration is conducted by the data provider. The part of the trajectory file that corresponds to the acquisition of the laser scan dataset consists of approximately 45,000 trajectory records at a sampling rate of 200 Hz. From Fig. 6.2., we can see that the airplane kept heading north when range data was collected by the scanner and the roll and heading remained similar.
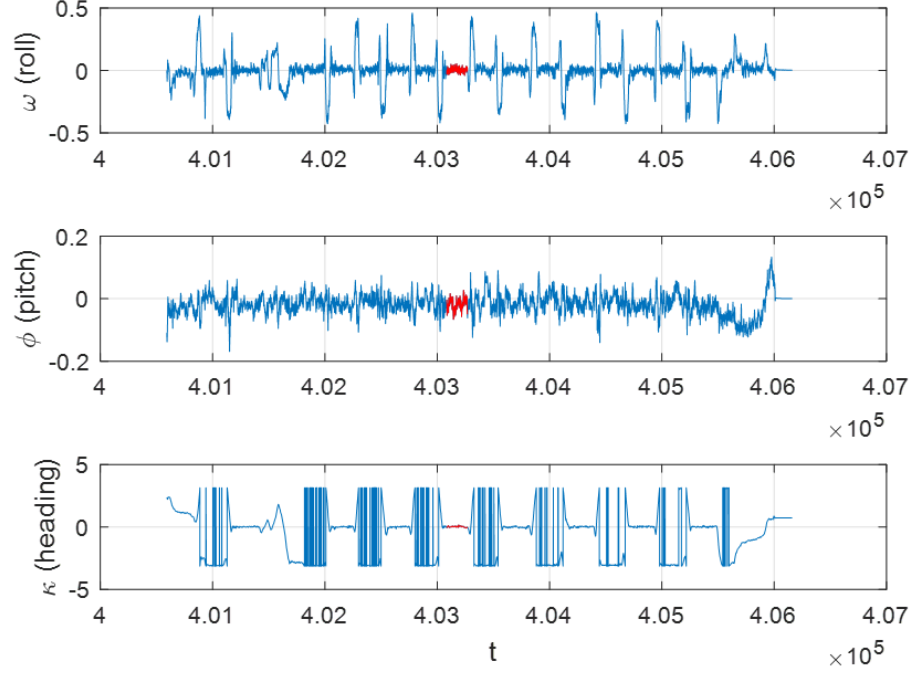
Fig. 6.2. The platform directions shown in t_{IMU} tag. The section where lidar sensor collected data is highlighted in red.

6.3.2 Reference DEMs

We collect three DEMs for our study. The first one is a 5m DEM (NAD 1983 UTM zone 18N) obtained from USGS National Geologic Map Database (NGBMDB); the second one is a 10m DEM (GCS North America 1983/NAVD88 geoid) obtained from NED (National Elevation Dataset); the third one is an ASTER (Advanced Spaceborne Thermal Emission and Reflection Radiometer) GDEM (Global Digital Elevation Model) version 2 with 30m resolution (GCS WGS 1984/EGM96 geoid) from USGS earth explorer. Among them, the highest resolution reference dataset in the study area that was available to us at the time of the study is the DEM with 5m ground sampling distance collected by the USGS for geological studies in the Paine Run watershed (https://ngmdb.usgs.gov/Prodesc/proddesc_70841.htm 10/23/2018).

We conduct a pairwise comparison among the three DEMs. The difference is shown in Fig. 6.3.

Ideally the three DEMs should agree with each other where the random errors/noises are attributed to cell resolution. In Fig. 6.3., however, the differences among them are quite high. This may be explained by the measurement errors, canopy effects, etc. Relatively, the difference between the 5m and 10m DEM is small. We will opt out of the 30m DEM since the canopy effects of ASTER GDEM can be very large.

The height difference of the 5m and 10m references over the study area is shown in Fig. 6.4. In most of the study area, the 10m DEM is lower than 5m DEM. This may be caused by the canopy effect. However, such phenomenon reverses in the southwestern corner, where the two sides of a ridge have opposite DEM difference (highlighted in purple circle).
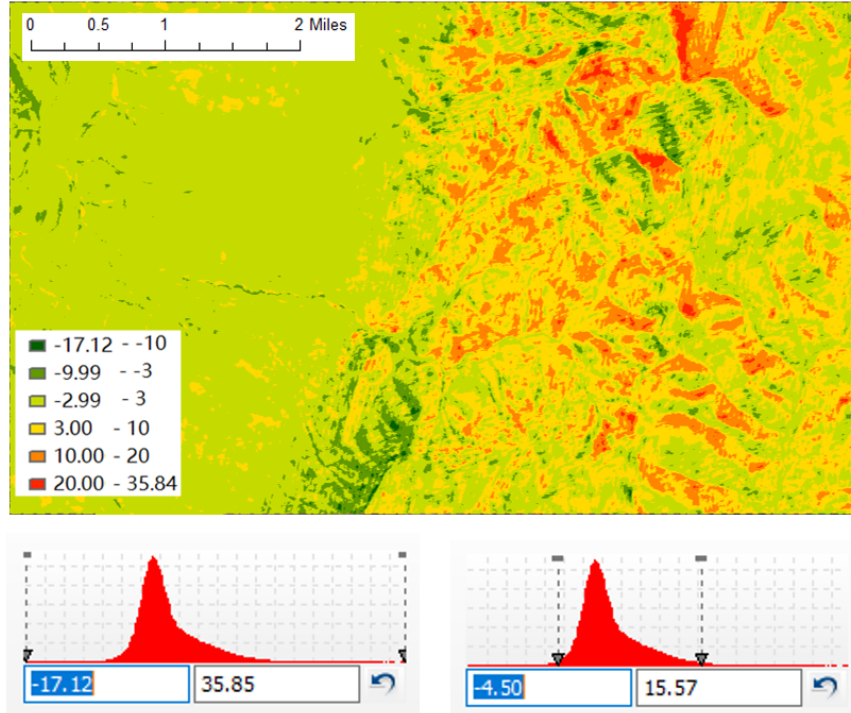
(a) $DEM_{5m} - DEM_{10m}$
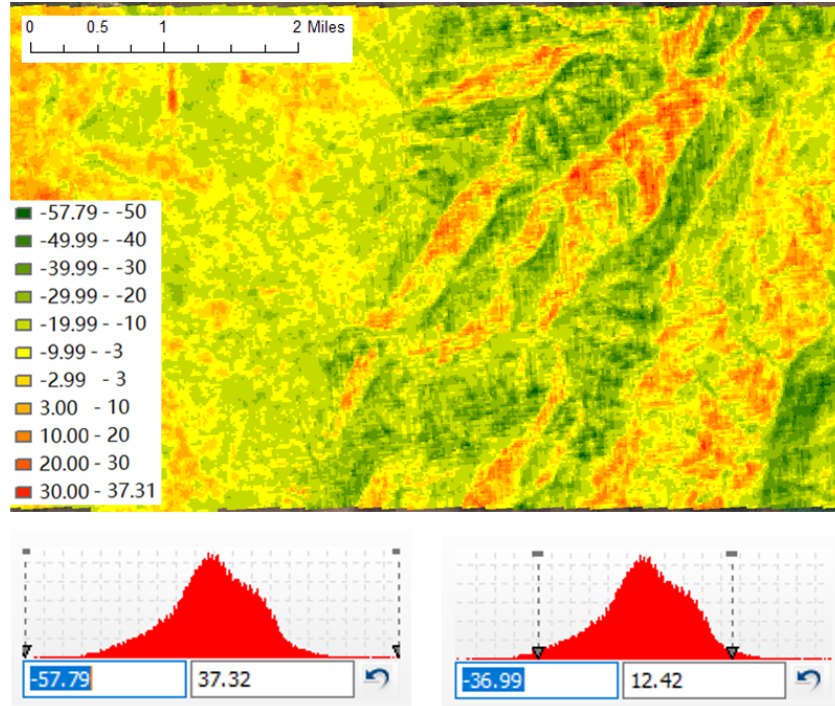
(b) $DEM_{5m} - DEM_{30m}$
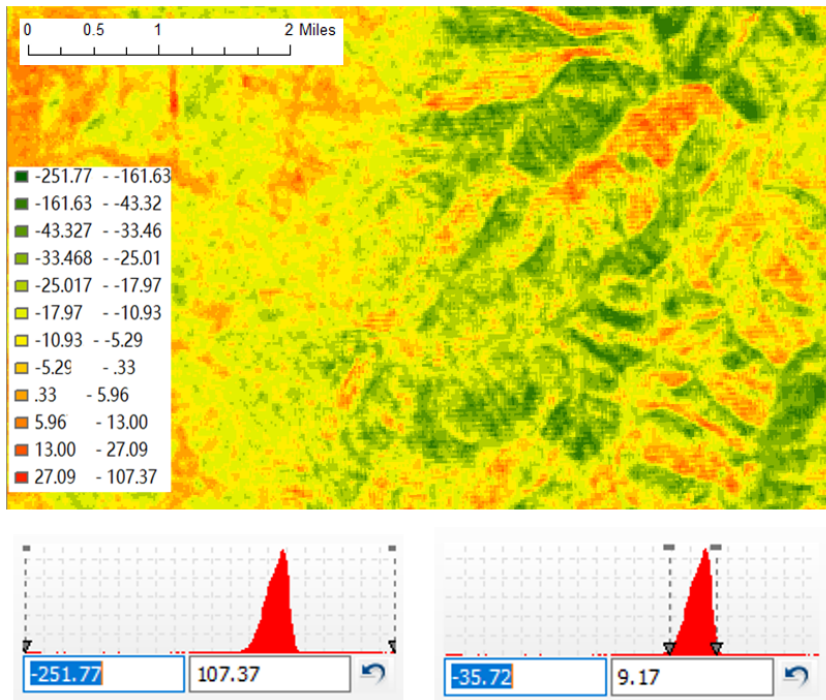
(c) $DEM_{10m} - DEM_{30m}$

Fig. 6.3. Comparison of all the three reference DEMs (m).
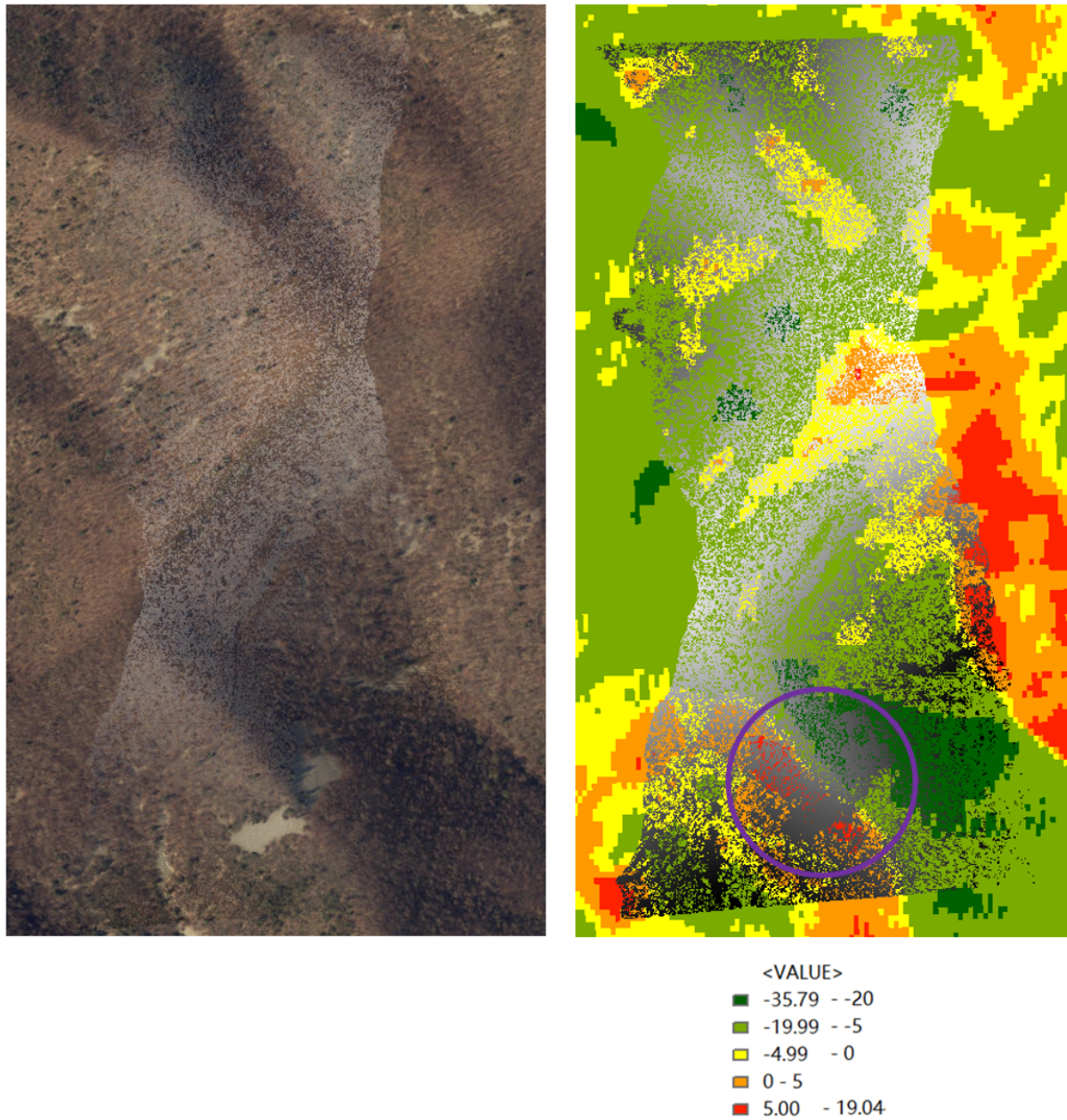
Fig. 6.4. (Left) The study area shown in the World Imagery of Esri; (Right) The difference (m) of the 5m and 10m reference DEMs: $DEM_{10m} - DEM_{5m}$. In both images, the area covered by lidar points is marked as gray.
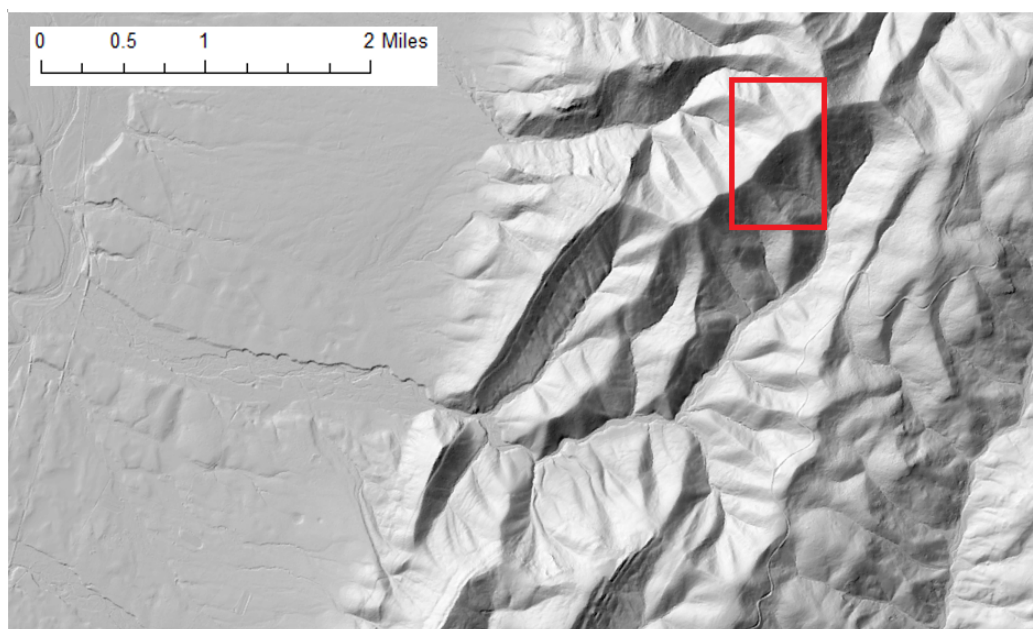
(a) 5m DEM
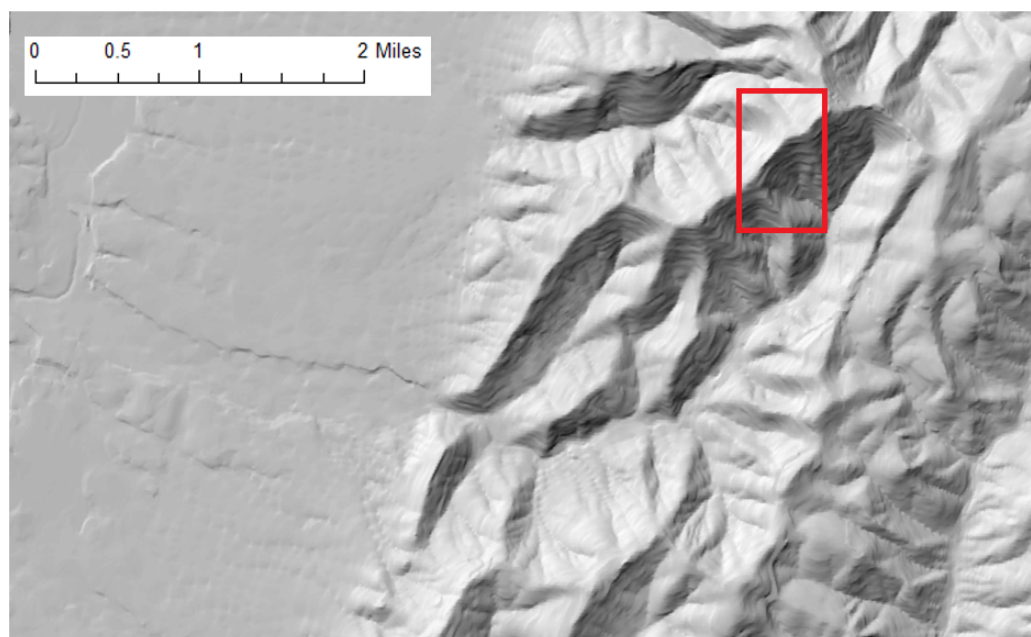
(b) 10m DEM
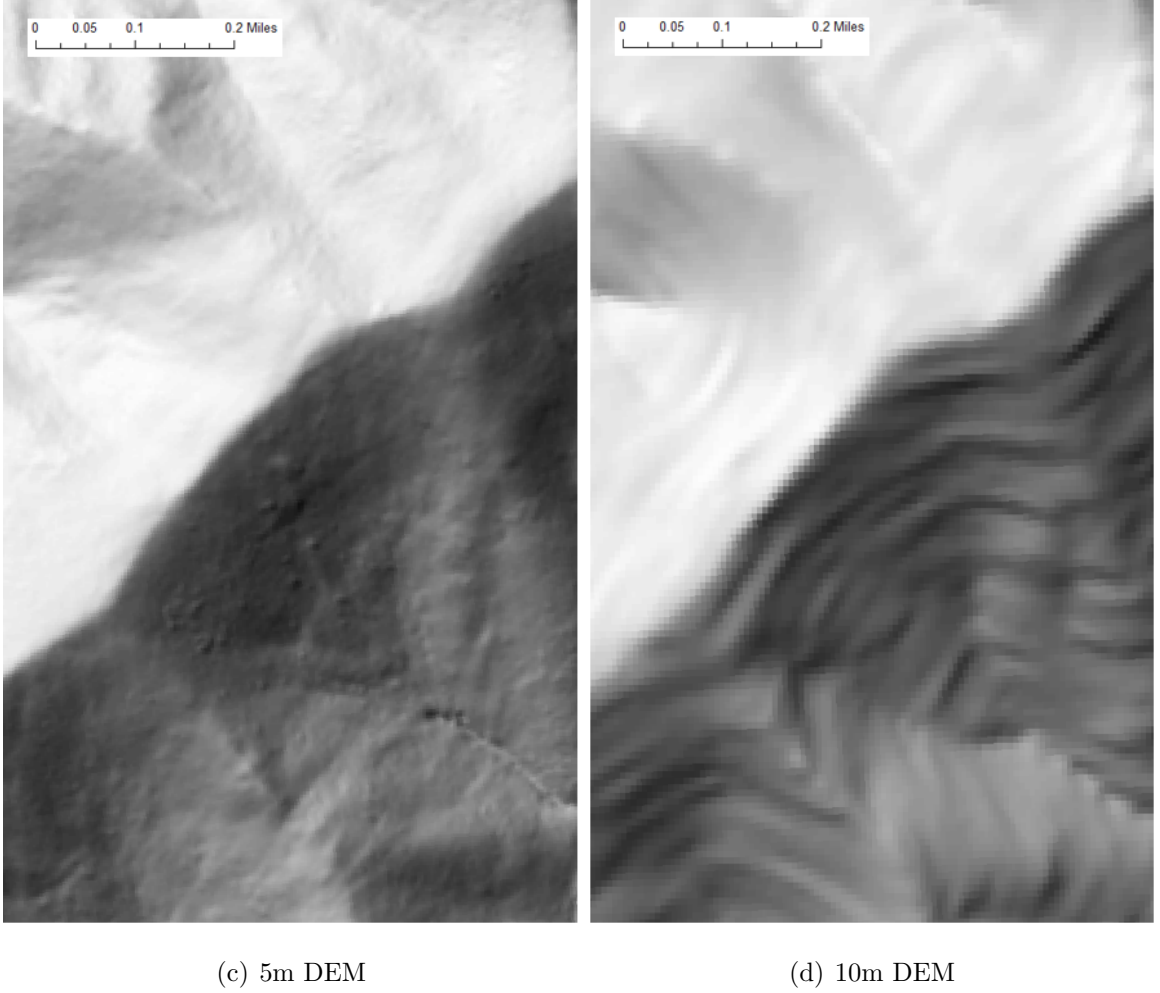
(c) 5m DEM   (d) 10m DEM

Fig. 6.5. Hillshaded reference DEMs: (a) 5m DEM; (b) 10m DEM; (c) the study area in the 5m DEM; (d) the study area in the 10m DEM.

6.4 Experiment

6.4.1 Direct Georeferencing

In direct georeferencing, the laser scanner and the IMU are assumed to be well aligned so that $[\Delta\omega_0,\ \Delta\phi_0, \Delta\kappa_0] = [90°,\ 90°,\ 0°]$. Also, the system is assumed to be synchronized as $\Delta t_0 = 0$s. Under these assumptions, we have $\theta_0 = [\Delta t_0,\ \Delta\omega_0,\ \Delta\phi_0,$

Table 6.1.
Results of particle swarm optimization

Reference DEM		5m DEM	10m DEM
Optimization results	Δt_1	14.8471s	14.9224s
	$\Delta\omega_1$	91.8591°	89.2209°
	$\Delta\phi_1$	88.5384°	89.8452°
	$\Delta\kappa_1$	-0.8713°	1.7304°

$\Delta\kappa_0] = [0s, 90°, 90°, 0°]$ as is shown in Fig. 6.6. The generated point cloud under θ_0 is compared to the 5m reference DEM.

There is a significant difference between the lidar DEM and the reference DEM. The mean difference of 91.16m is very uncommon even for the case that the boresight misalignment is considered, so it is necessary to calibrate both the boresight and the time misalignment according to the objective function described in previous section.

6.4.2   Heuristic Optimization

First, we sample 90,000 points from the data over the study area. An initial estimation of the parameters will be obtained by minimizing the objective function of $f_{90000}(\theta_G; \theta_G)$.

As is shown in Fig. 6.7., we selected three strips of data as the sample points. Each strip includes 30,000 points. They are: points 1-30,000; points 450,001-480,000; points 900,001-930,000. We then run particle swarm optimization with both 5m and 10m reference DEMs. The difference between the lidar DEM and both reference DEMs are calculated. The results are summarized in Table 6.1., Fig. 6.8., and Fig. 6.9.

After the initial optimization, the hillshaded DEM is significantly improved as the horizontal strips become much less obvious, as is shown in Fig. 6.8(a) and Fig.
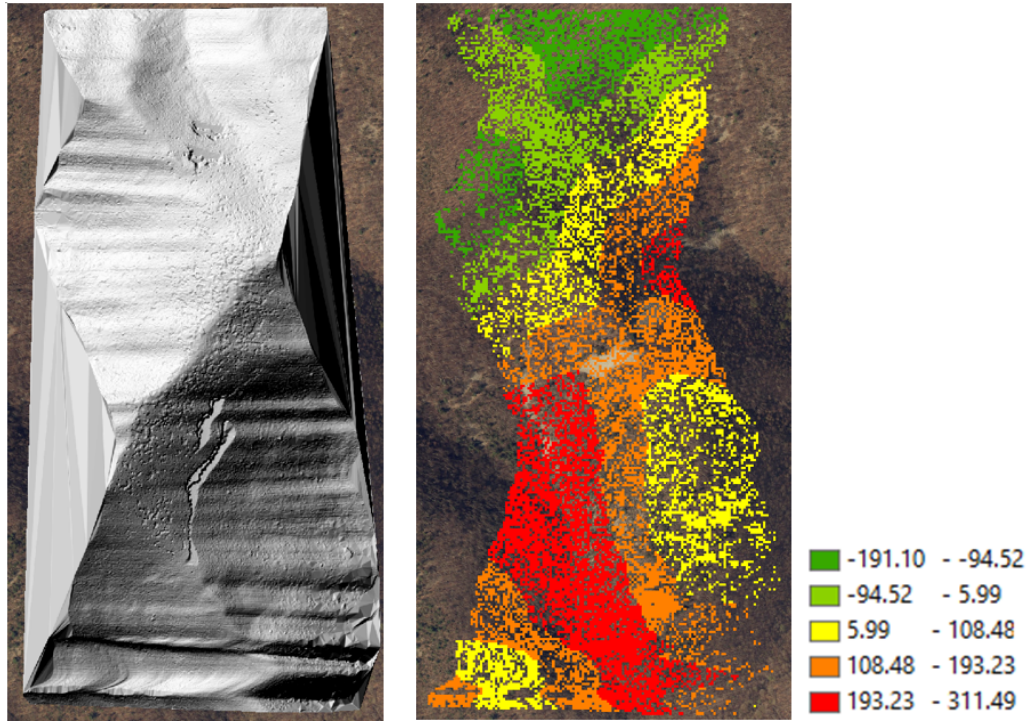
(a) The hillshaded DEM_{lidar}.

(b) $DEM_{lidar} - DEM_{5m}$
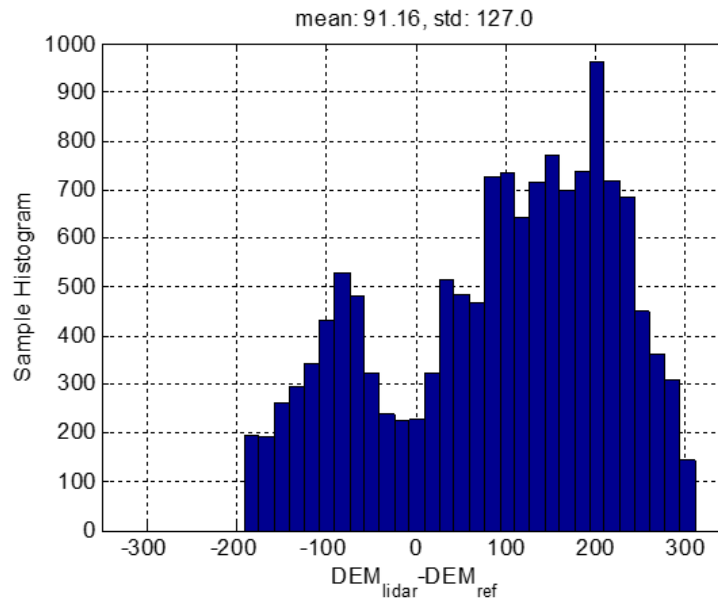
(c) The histogram of the DEM difference

Fig. 6.6. DEM differences (m) between the lidar points and the reference. The lidar data is generated with the initial guess of θ_0.
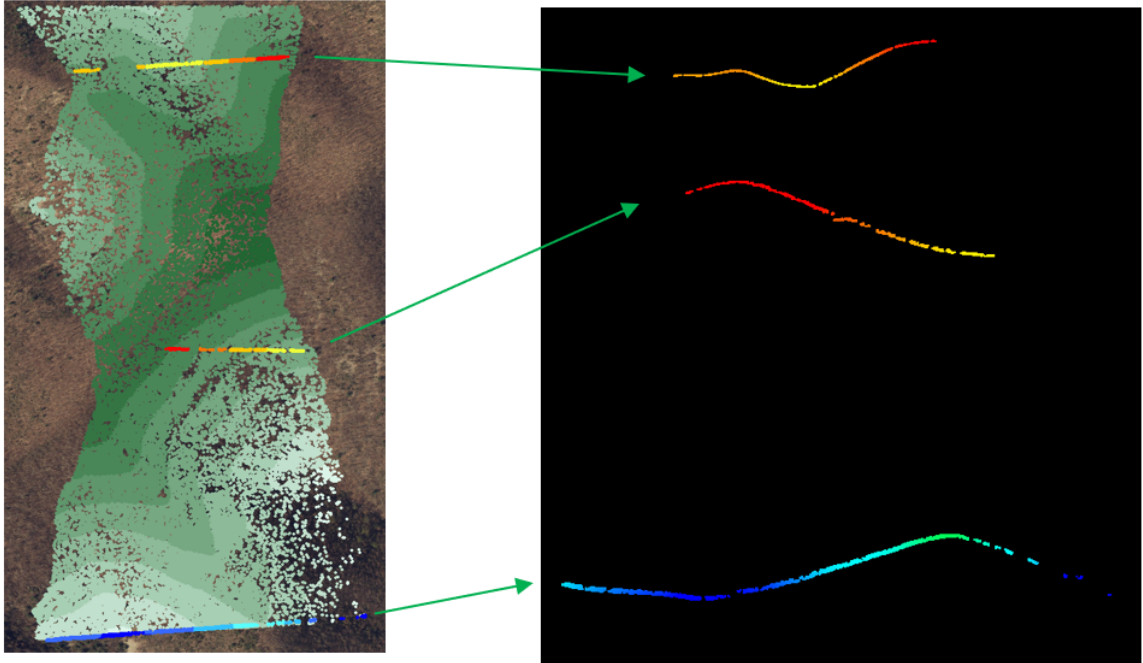
Fig. 6.7. The sampled 90,000 points used in the initial optimization.

6.9(a). From the view of DEM differences, the 5m DEM matches the lidar point clouds better. This can be reflected from both the maximum and minimum DEM differences, as is shown in Fig. 6.8(b) and Fig. 6.9(b), and the mean difference, as is shown in Fig. 6.8(c) and Fig. 6.9(c). In contrast, the DEM differences between the lidar DEM and the 10m reference DEM has the mean of 9.130m, which is ten times higher than the mean difference of 0.884m between the lidar DEM and the 5m reference DEM. In the next steps of optimization, we will exclusively use the 5m DEM as the reference.

Comparing Fig. 6.6. and Fig. 6.9., we observe the mean difference between the 5m reference DEM and the lidar DEM decreases from 91.16m to 0.86m. It means that most errors in the direct georeferencing are removed by particle swarm optimization. The result shows that the estimated time misalignment is greater than 14.84 seconds and the estimated boresight angles are around 1 to 2 degrees deviated from the
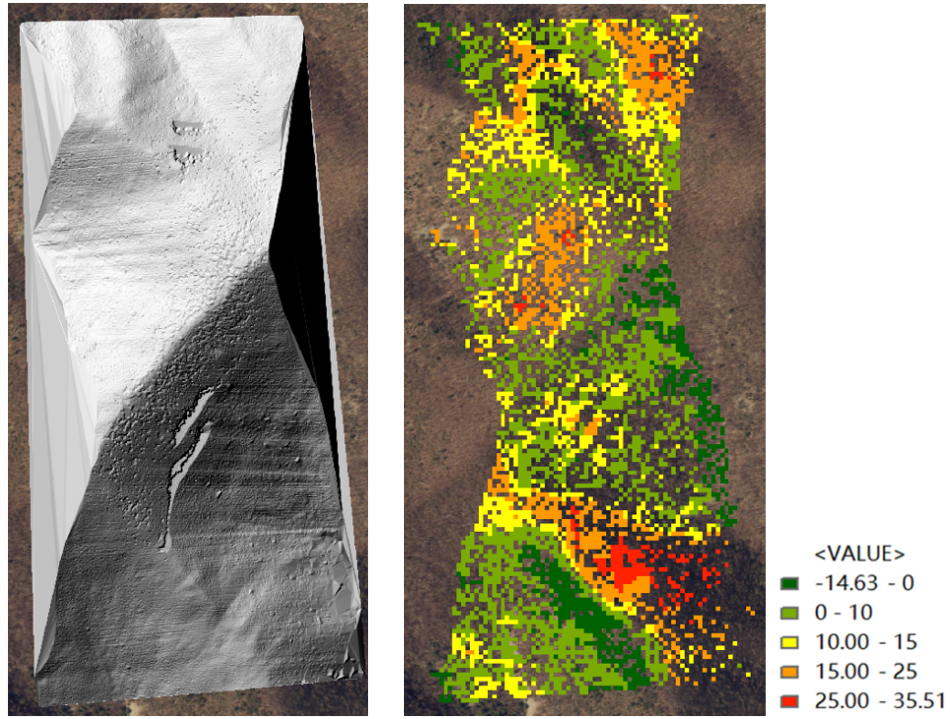
(a) The hillshaded DEM_{lidar} (b) $DEM_{lidar} - DEM_{10m}$
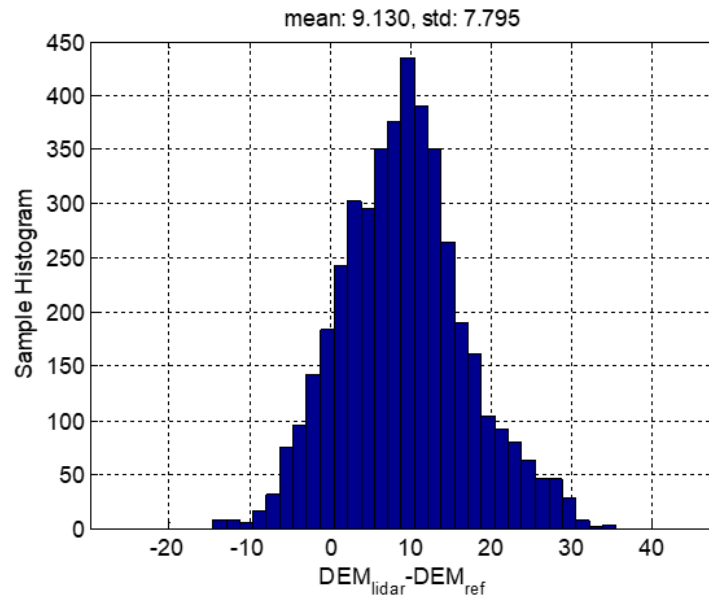
(c) The histogram of the DEM difference

Fig. 6.8. Particle swarm optimization result with 10m DEM reference (in meters).
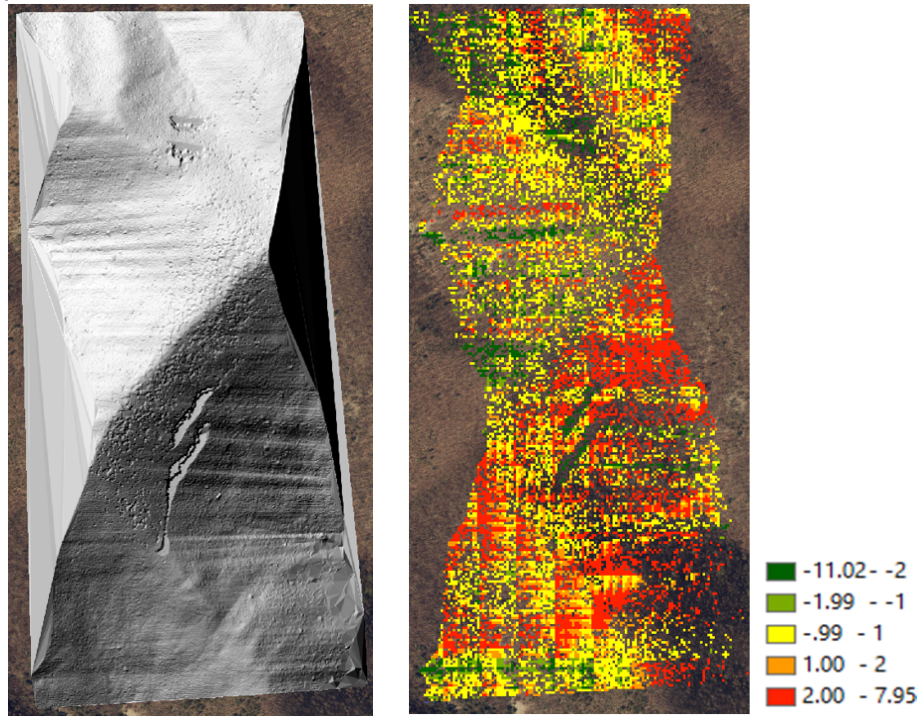
(a) The hillshaded DEM_{lidar}

(b) $DEM_{lidar} - DEM_{5m}$
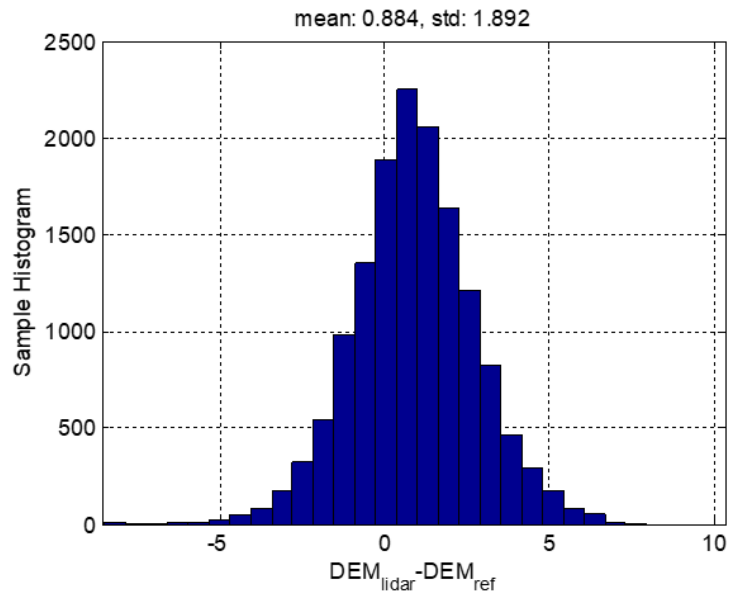
(c) The histogram of the DEM difference

Fig. 6.9. Particle swarm optimization results with 5m DEM reference (in meters).

initial guess. We conclude that the main error before optimization during the direct georeferencing comes from the unsynchronized clocks between the laser scanner and POS.

The particle swarm optimization result could be further improved for the following reasons: (1) the particle swarm optimization uses a series of random numbers in the search process. It is a good strategy to avoid the local minimal trap, but it cannot guarantee that the output result is the global optimal; (2) the performance of the solution is restricted by the number of the lidar points; (3) since the objective function is $f_N(\theta_G; \theta_G)$, the ground filtering process is embedded in each iteration. In the study area, the forest area has dense leaves so that many lidar signals cannot penetrate the canopy and reach the ground. Errors are inevitable in the filtered ground. Furthermore, such errors fluctuate as $N_{grnd}(\theta_G)$ changes so that the results of parameter estimation are affected.

6.4.3 Synchronization

With the result of the initial optimization, we obtained the solution θ_1 as the first approximation to the global optimal solution. The following search process will be conducted in a relatively small neighborhood on the objective function $f_N(\theta_G; \theta_1)$. As is discussed in Section 6.1.3, the result of waveform filtering is applied to select the ground points so that the selection of the ground points is no longer a variable of θ_G. Hence, a convex optimization such quasi-Newton algorithm can be utilized to find out the local minimal around the result of particle swarm optimization.

In the process of synchronization, we fix the boresight angles to be $[\Delta\omega_0, \ \Delta\phi_0, \Delta\kappa_0]$ and conduct the BFGS quasi-Newton algorithm (Broyden, C. G, 1970; Fletcher, R., 1970; Goldfarb, D., 1970; Shanno, D. F., 1970) with different initial values of Δt_0. We ran 11 experiments by changing the initial value from 14.50 to 15.50 seconds with an increment of 0.10 seconds. The results are summarized in Table 6.2.

Table 6.2.
Optimization result of time calibration

Experiment #	Initial value Δt_0	Converged value Δt_2
1	14.50	14.9990
2	14.60	14.9991
3	14.70	14.9989
4	14.80	14.9988
5	14.90	15.0605
6	15.00	14.9990
7	15.10	14.9991
8	15.20	15.0605
9	15.30	14.9991
10	15.40	14.9989
11	15.50	14.9991

Regardless of the initial value, the time misalignment Δt always converges to 15 seconds. We conclude that Δt_2=15 seconds is the stable solution of our synchronization process. On the other hand, the leap seconds of civil time Coordinated Universal Time (UTC) on the data collection day is 15 seconds. It means the two data use a different system: the GPS/IMU units use a GPS time while the scanner uses UTC time. And this has not been considered when deriving the trajectory. We then set Δt= 15.0 second and conduct the further optimization for boresight angles.

6.4.4 Boresight Calibration

After the synchronization, the problem of self-calibration is reduced to a problem of boresight optimization on $f_N \left((\Delta \omega, \Delta \phi, \Delta \kappa)_G; \theta_1, \Delta t_2 \right)$ for a given set of ground points $\{ p_{grnd} (\theta_1) \}_{N_{grnd}(\theta_1)}$. When selecting the number of ground points, we strive

for balance between the time consumption and the fact that the lidar points should be adequate to reflect the ground shape. In our experiment, we choose one tenth of all the ground points in the optimization, so that $N_{grnd}(\theta_1)$ =25,637.

With the initial value $[\Delta\omega_0,\ \Delta\phi_0, \Delta\kappa_0] = [90°,\ 90°,\ 0°]$ and the calibrated time $\Delta t_2 = 15s$, the distribution of the points and their distance to the reference DEM is shown in Fig. 6.10. In the figure, both the color and the radius of each point is coded by the difference between the lidar estimated height and the reference height. We can see the height difference is not evenly distributed: most of the lidar ground points are higher than the reference DEM in the upper half map and lower than the reference DEM in the lower half map. The histogram of the height difference is shown in Fig. 6.11. It represents two peaks, one is positive and one negative, which can happen if the system is not well calibrated and the quality of the ground filtering is not satisfying.
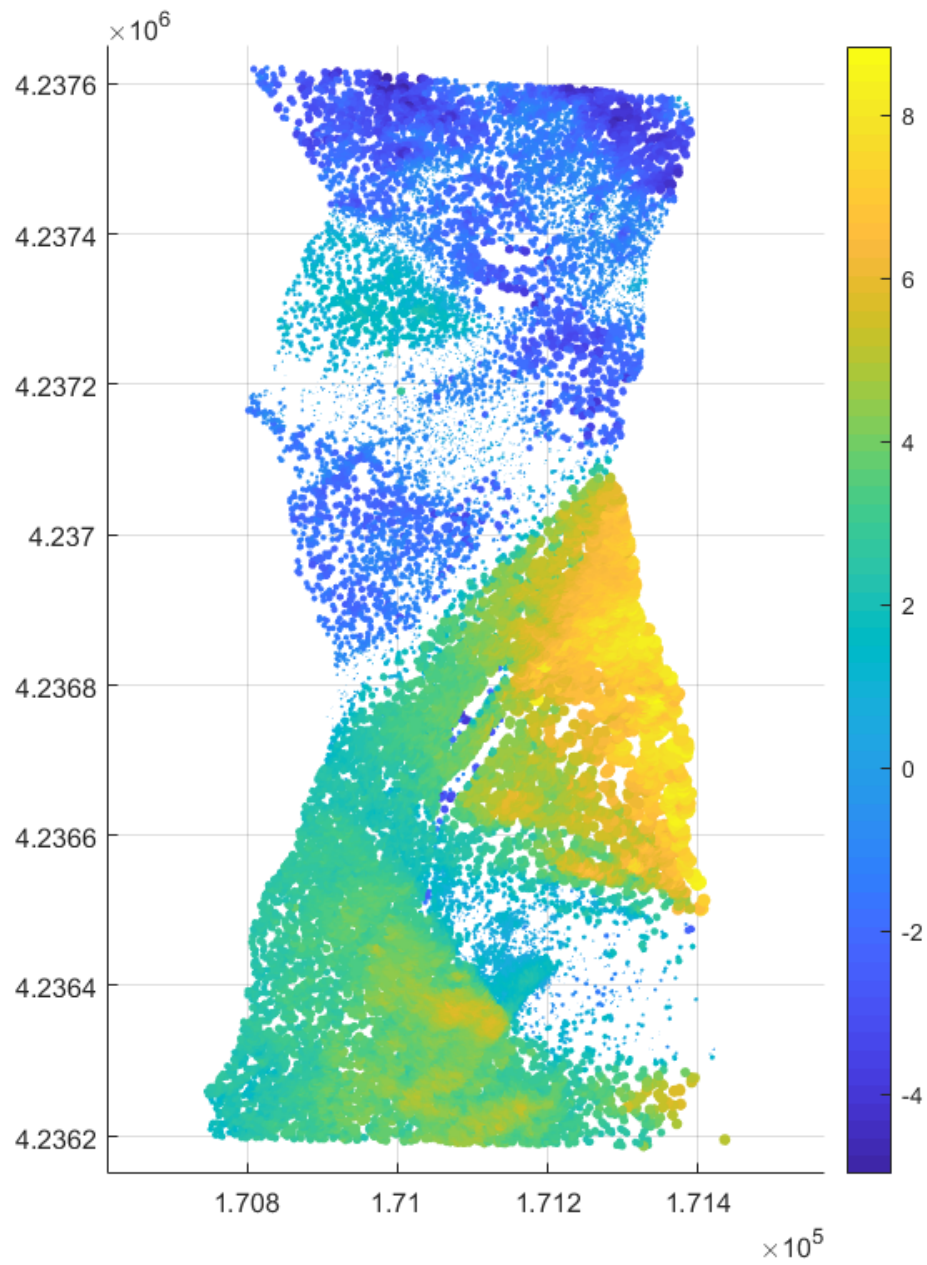
Fig. 6.10. The 25,637 ground points that are included in the optimization for boresight calibration (m).

Fig. 6.11. The histogram of height (m) difference between the 25,637 ground points and the reference DEM. The lidar estimated heights are obtained after the time synchronization is calibrated.

With the boresight angles obtained from the initial optimization$[\Delta\omega_1, \Delta\phi_1, \Delta\kappa_1] =$ $[91.8591°, \ 88.5384°, \ -0.8713°]$ and the calibrated time $\Delta t_2 = 15$s, the distribution of the points and their distance to the reference DEM is shown in Fig. 6.12. The histogram of the height difference is shown in Fig. 6.13. From both the 2-D distribution and the histogram, the height difference is still not evenly distributed.
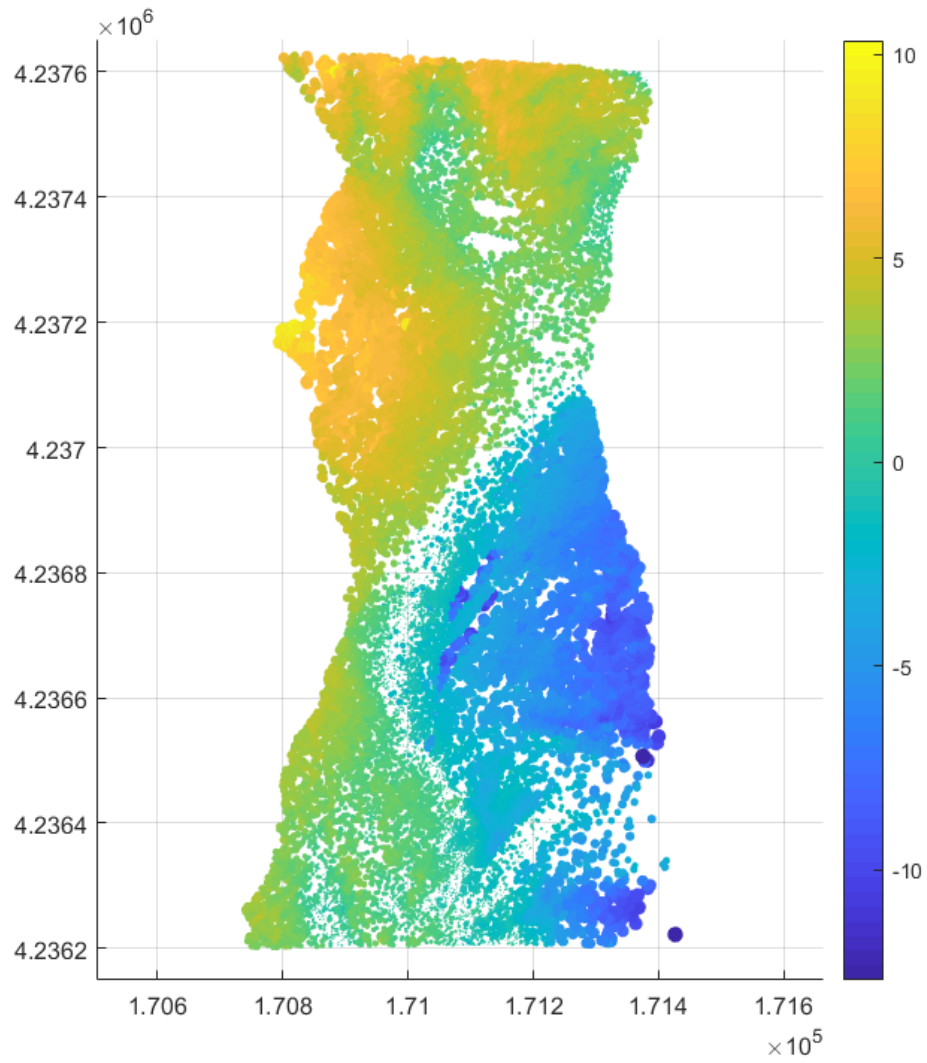
Fig. 6.12. The 25,637 ground points after the calibration of time synchronization and the initial optimization of boresight angles (m).
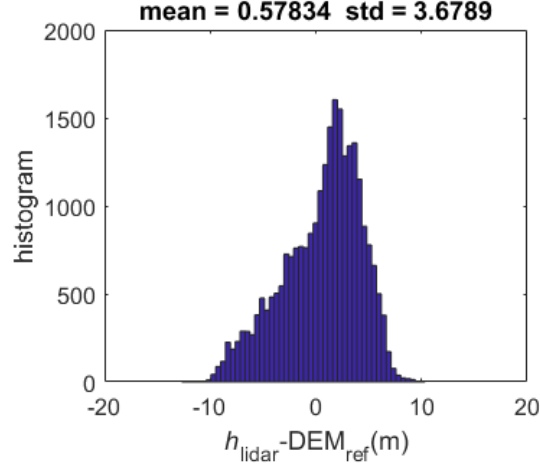
Fig. 6.13. The histogram of height (m) difference between the 25,637 ground points and the reference DEM after the calibration of time synchronization and the initial optimization of boresight angles.

For multiple initial values, we run the quasi-Newton algorithm for the boresight calibration. Some results are summarized in Table 6.3.

Table 6.3.
Optimization result of boresight calibration.

Initial value (°)			Converged value (°)			$\sqrt{MSD}$(m)
90	90	0	90.8804	89.0024	-0.1561	1.0303
90	90	-5	90.8804	89.0024	-0.1561	1.0303
90	90	5	90.8804	89.0024	-0.1561	1.0303
85	90	0	90.8804	89.0024	-0.1561	1.0303
95	90	0	90.8804	89.0024	-0.1561	1.0303
90	85	0	90.8804	89.0024	-0.1561	1.0303
90	95	0	90.8804	89.0024	-0.1561	1.0303

The experiments are repeated 1,000 times with the random initial values in the range of $\{[\Delta\omega, \Delta\phi, \Delta\kappa] : \Delta\omega \in [85°, 95°], \Delta\phi \in [85°, 95°], \Delta\kappa \in [-5°, 5°]\}$. When the initial offset is no greater than 5° from [90°, 90°, 0°], the algorithm converged

to [90.8804°, 89.0024°, −0.1561°], which is the stable solution of our algorithm. Fig. 6.14. shows the difference between the 25,637 lidar ground points and the reference DEM is overall evenly distributed. The histogram in Fig. 6.15. shows that the mean of the height difference is reduced to 0.8462m with the standard deviation of 0.5876m.

With the calibrated parameter $\theta^* = [15s,\ 90.8804°,\ 89.0024°,\ −0.1561°]$, the final point cloud and digital elevation model are generated. After the calibration, the west-east linear undulations that appear in Fig. 6.6(a), Fig. 6.8(a) and Fig. 6.9(a) are removed, as is shown in the hillshaded DEM of Fig. 6.16(a). Fig. 6.16(b) shows that the height difference between the lidar DEM and the reference DEM is quite evenly distributed over the study area. The histogram of the height differences is plotted in Fig. 6.16(c). Compared to the initial optimization results, the mean is reduced from 0.884m to 0.866m, and the standard deviation is reduced from 1.892m to 1.375m. The DEM difference of 0.866m could possibly be caused by the errors of the ground filtering or the GPS/INS measurement and integration. Comprehensive comparison and more convincing evaluation based on additional independent data remains to be a future effort.

6.5   Summary

Conventionally, boresight calibration is conducted either by comparing lidar points with known ground control points or the co-registration of multiple lidar strips. It becomes challenging when no exact correspondence for ground control points exists. Furthermore, such conventional calibration often requires large amounts of regularly shaped objects, which may be absent in many cases. The self-calibration method proposed in this work makes use of the publicly accessible DEM as control over the entire study area. Compared to the conventional method, the new method has minimum requirements on the flights and ground control over the study area. As such, our method provides a single strip, GCP free solutions to the boresight misalignment calibration.
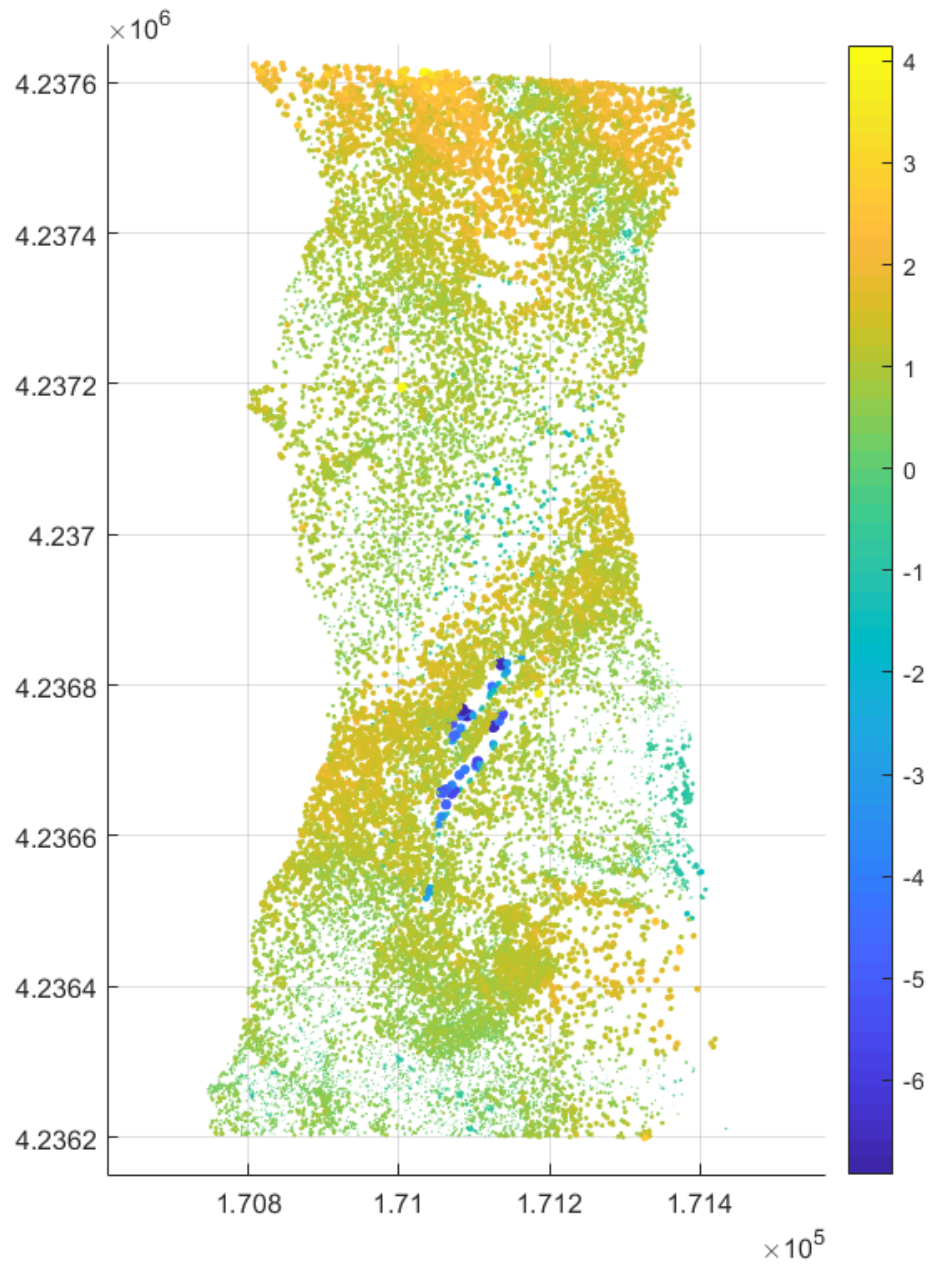
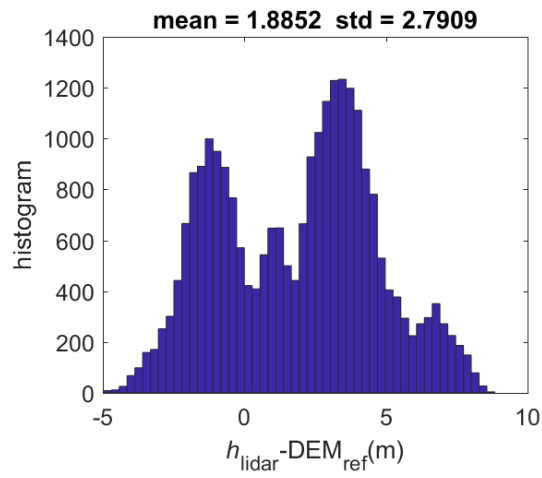Fig. 6.14. The height difference (m) of the 25,637 points georeferenced with the optimized boresight angles.
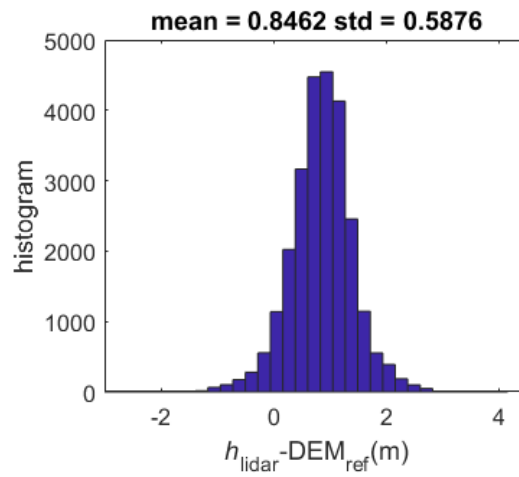
Fig. 6.15. The histogram of height (m) difference between the 25,637 ground points and the reference DEM after the boresight is calibrated.
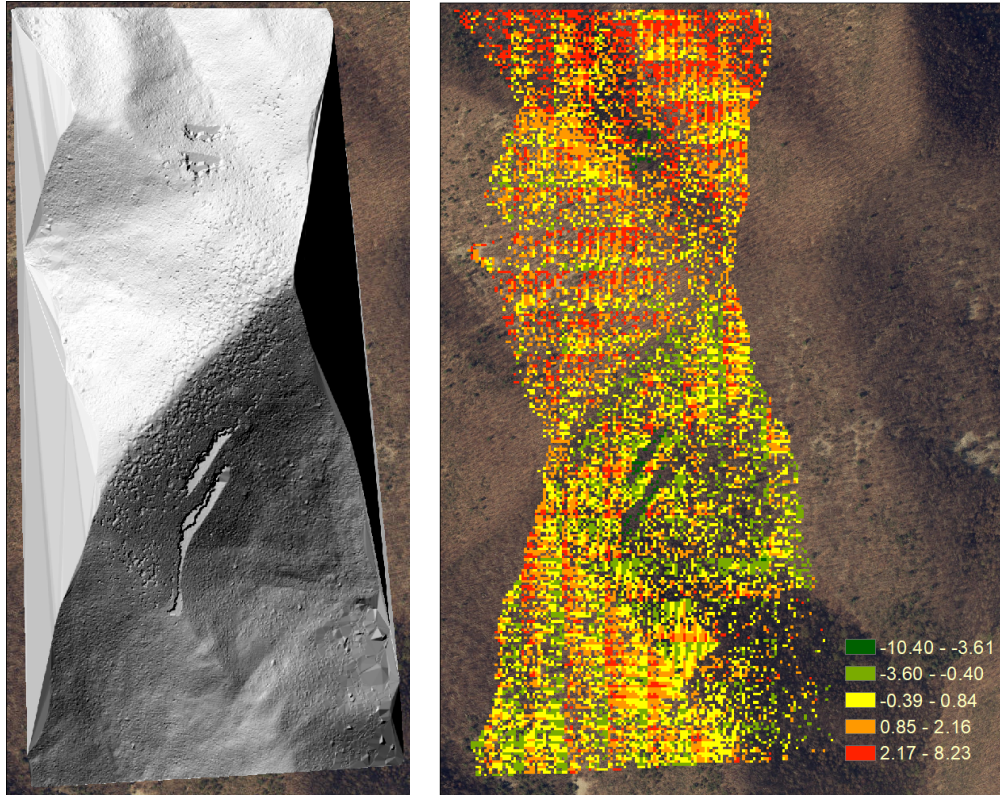
(a) The hillshaded DEM_{lidar}.

(b) $DEM_{lidar} - DEM_{5m}$
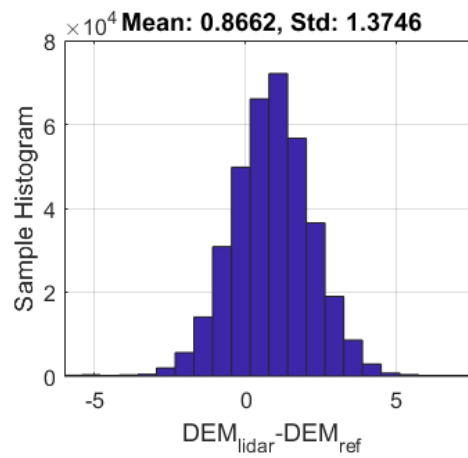
(c) The histogram of the DEM difference

Fig. 6.16. DEM difference (m) after self-calibration.

The robustness of the new approach is verified from the experiments. For both time synchronization and boresight misalignment, a stable result can be obtained regardless of the initial values of optimization.

The new method consists of two steps to assure a correct and stable solution. In the first step, we use heuristic optimization to find a good initial solution. The second step involves fine optimization conducted in a small neighborhood of the global optimal solution. This two-step strategy is developed to address the specific problem encountered in our experiments where the time synchronization is far from the common value of $\Delta t = 0$. In our example, the heuristic optimization technique, particle swarm optimization, is utilized. In many other cases, the time synchronization is not as severe as in our case or the system may already be synchronized so that $\theta_G \approx \theta_g$ and $\{p_{grnd}(\theta_g)\} = \{p_{grnd}(\theta_G)\}$. In such cases, the ground filtering in each iteration and the particle swarm optimization may be skipped.

7. CONCLUSION

This thesis studied the geospatial processing of the airborne full waveform lidar data, which is both comprehensive and thorough. We developed new methodologies on the two main steps of full waveform data processing. Our contribution is twofold. For the range measurements, we introduced a nonparametric mixture model that can fit the real lidar signals better than the conventional Gaussian mixture model. We also developed a fuzzy mean shift algorithm to decompose the lidar waveforms. Compared to the conventional methods such as EM, the new approach is not only faster, able to generate more details, but also more robust because the range measurements are not affected by the process of noise filtering. For calibraing the boresight angles, we took advantage of the abundant information of the full waveform data and developed a self-calibration method based on a reference DEM. The new self-calibration approach works without the need of multiple flight strips and planner objects. The boresight calibration can be conducted with a single strip over dense forest area.

7.1 Waveform Decomposition

We introduced a nonparametric mixture model to describe asymmetric lidar waveform components. Compared with the traditional GMM, the nonparameter mixture model successfully models a variety of waveform components, regardless of whether they are Gaussian or non-Gaussian and symmetric or asymmetric. As a general approach to waveform decomposition, the proposed fuzzy mean shift essentially is a density-based data clustering approach, which does not assume that waveforms follow any functional or parametric distribution. Unlike many existing practices, the FMS algorithm does not need peak detection prior to decomposition and can simultaneously determine the number of waveform components during the decomposition

process. Furthermore, the point density of the decomposed waveforms largely relies on one single parameter, i.e., the kernel bandwidth, for which three to four waveform sampling intervals has been shown suitable in our work.

Our tests over a dense forest area have validated the noticeable asymmetry of the returned waveforms and demonstrated satisfactory performance of the proposed FMS method. A detailed DEM with minimum artifacts can be produced through the subsequent filtering. Compared with the conventional EM method under an optimal implementation, the FMS approach is about three times faster, whereas the resultant DEM is very similar and tends to have fewer artifacts. We not only develop a novel theoretical model and general solution to the waveform decomposition problem but practically provide a promising satisfactory approach to terrain generation under heavy canopy. This is useful for studies in geomorphology, hydrology, and other Earth science subjects.

7.2 Self-Calibration

We developed a novel self-calibration method which requires no ground control points, no planner objects, and no overlap flight strips. The boresight angles can be estimated with a single flight strip over the forest area. Compared to the conventional boresight calibration method, which is conducted either by comparing the lidar points with the known ground control points or the coregistration of multiple lidar strips, our approach significantly reduces the cost of boresight calibration. With the reduced cost, the boresight calibration can be conducted routinely and more frequently, so that it potentially makes the lidar measurement results more reliable and more precise.

Other advantages of the new self-calibration method include: (1) it synchronizes the time clocks after the lidar data is delivered. Before our work, the soft synchronization was rarely reported. (2) it calibrates the boresight misalignment without ground control points and boresight flight plan. The restriction of the self-calibration

approach has the least limitation among all the existing methods. (3) it solves the problems of synchronization and boresight calibration when they both exhibit.

The uniqueness of our self-calibration method is the use of the waveform filtering and publicly accessible DEM, which takes advantage of the development of both hardware manufacturers and professional geomatics community. With the growing adoption of full waveform lidar and the increasing availability of high resolution, high quality DEMs, more broad applications and more reliable results from the new self-calibration method can be expected.

7.3   Future Work

Future studies can be carried out in a few topics. They may include: optimal kernel selection, bandwidth selection, and alternative fuzzy clustering algorithms. There is also a need to comprehensively evaluate the proposed waveform decomposition approach. To be specific, further studies may look into the benefit of the consideration of asymmetry and the adoption of nonparametric mixture model in urban areas. For vegetation, forestry, and bathymetry studies, further exploration is needed to examine the ability of the FMS method to extract near-ground returns under low vegetation and dense canopy for subsequent DEM construction.

The decomposed waveform components can be further utilized for vegetation classification, biomass estimation, and single tree detection. Unlike the conventional GMM, the decomposed waveforms may not necessarily be Gaussian or symmetric under the nonparametric modeling. Asymmetry, revealed by the nonparametric approach, is a unique property that GMM-based methods lack and do not directly provide. Waveform signature, including the skewness property, may be examined in terms of different terrain features or objects.

More interesting results are expected from the extension of self-calibration. For example, the lidar data can be divided into many sections according to the acquisition time. The boresight angles can be estimated for each section, so the behavior of the

boresight drift can be studied. In addition, blocks of multiple flight strips may also be evaluated as comparison to the developed self-calibration method.

REFERENCES

REFERENCES

Akaike, H. (1974). A new look at the statistical model identification. IEEE transactions on automatic control, 19(6), 716-723.

Anderson, K., Hancock, S., Disney, M., & Gaston, K. J. (2016). Is waveform worth it? A comparison of LiDAR approaches for vegetation and landscape characterization. Remote Sensing in Ecology and Conservation, 2(1), 5-15.

Axelsson, P. (2000). DEM generation from laser scanner data using adaptive TIN models. International Archives of Photogrammetry and Remote Sensing, 33(4), 110-117.

Azadbakht, M., Fraser, C. S., & Khoshelham, K. (2016). A sparsity-based regularization approach for deconvolution of full-waveform airborne lidar data. Remote Sensing, 8(8), 648.

Bender, D., Schikora, M., Sturm, J., & Cremers, D. (2013). A graph based bundle adjustment for ins-camera calibration. International Archives of the Photogrammetry, Remote Sensing and Spatial Information Sciences, 1, W2.

Ben-Hur, A., Horn, D., Siegelmann, H. T., & Vapnik, V. (2001). Support vector clustering. Journal of machine learning research, 2(Dec), 125-137.

Bretar, F., Chauve, A., Mallet, C., & Jutzi, B. (2008, July). Managing full waveform LIDAR data: A challenging task for the forthcoming years. In XXI congress (pp. part-B).

Broyden, C. G. (1970). The convergence of a class of double-rank minimization algorithms 1. general considerations. IMA Journal of Applied Mathematics, 6(1), 76-90.

Bye, I. J., North, P. R. J., Los, S. O., Kljun, N., Rosette, J. A. B., Hopkinson, C., Chasmer, L., & Mahoney, C. (2017). Estimating forest canopy parameters from satellite waveform LiDAR by inversion of the FLIGHT three-dimensional radiative transfer model. Remote sensing of environment, 188, 177-189.

Casella, G., & Berger, R. L. (2001). Statistical Inference, 2nd Edition. Cengage Learning.

Chan, T.O. (2011). Feature-Based Boresight Self-Calibration of a Mobile Mapping System. Master Thesis, University of Calgary, Calgary, AB, Canada.

Chauve, A., Mallet, C., Bretar, F., Durrieu, S., Deseilligny, M., & Puech, W. (2007). Processing Full-Waveform LiDAR Data: Modelling Raw Signals, ISPRS Workshop on Laser Scanning 2007 and SilviLaser 2007, Espoo, Sept. 12-14, 2007. pp. 102-107.

Dempster, A. P., Laird, N. M., & Rubin, D. B. (1977). Maximum likelihood from incomplete data via the EM algorithm. Journal of the royal statistical society. Series B (methodological), 1-38.

Dhillon, I. S., Guan, Y., & Kulis, B. (2004, August). Kernel k-means: spectral clustering and normalized cuts. In Proceedings of the tenth ACM SIGKDD international conference on Knowledge discovery and data mining (pp. 551-556). ACM.

Fletcher, R. (1970). A new approach to variable metric algorithms. The computer journal, 13(3), 317-322.

Fowler, A., & Kadatskiy, V. (2010). Multiple Sensor Platforms. A special joint symposium of ISPRS Technical Commission IV & AutoCarto in conjunction with ASPRS/CaGIS 2010 Fall Specialty Conference, Orlando, Florida

Fukunaga, K., & Hostetler, L. (1975). The estimation of the gradient of a density function, with applications in pattern recognition. IEEE Transactions on information theory, 21(1), 32-40.

Golbon-Haghighi, M. H., Saeidi-Manesh, H., Zhang, G., & Zhang, Y. (2018). Pattern Synthesis for the Cylindrical Polarimetric Phased Array Radar (CPPAR). Progress In Electromagnetics Research, 66, 87-98.

Goldfarb, D. (1970). A family of variable-metric methods derived by variational means. Mathematics of computation, 24(109), 23-26.

Hancock, S., Armston, J., Li, Z., Gaulton, R., Lewis, P., Disney, M., ... & Gaston, K. J. (2015). Waveform lidar over vegetation: An evaluation of inversion methods for estimating return energy. Remote Sensing of Environment, 164, 208-224.

Hartzell, P. J., Glennie, C. L., & Finnegan, D. C. (2015). Empirical waveform decomposition and radiometric calibration of a terrestrial full-waveform laser scanner. IEEE Transactions on Geoscience and Remote Sensing, 53(1), 162-172.

Hebel, M., & Stilla, U. (2012). Simultaneous calibration of ALS systems and alignment of multiview LiDAR scans of urban areas. IEEE Transactions on Geoscience and Remote Sensing, 50(6), 2364-2379.

Hernandez-Marin, S., Wallace, A. M., & Gibson, G. J. (2007). Bayesian analysis of lidar signals with multiple returns. IEEE Transactions on Pattern Analysis and Machine Intelligence, 29(12), 2170-2180.

Hofton, M. A., Minster, J. B., & Blair, J. B. (2000). Decomposition of laser altimeter waveforms. IEEE Transactions on geoscience and remote sensing, 38(4), 1989-1996.

Hovi, A., Korhonen, L., Vauhkonen, J., & Korpela, I. (2016). LiDAR waveform features for tree species classification and their sensitivity to tree-and acquisition related parameters. Remote sensing of environment, 173, 224-237.

Jung, J., & Crawford, M. M. (2008, July). A two-stage approach for decomposition of ICESat waveforms. In IGARSS 2008-2008 IEEE International Geoscience and Remote Sensing Symposium (Vol. 3, pp. III-680). IEEE.

Kenney, J. (1995). Particle swarm optimization. In Proc. IEEE International Conference on Neural Networks, 1995 (pp. 1942-1948).

Krichel, N. J., McCarthy, A., & Buller, G. S. (2010). Resolving range ambiguity in a photon counting depth imager operating at kilometer distances. Optics express, 18(9), 9192-9206.

Langridge, R. M., Ries, W. F., Farrier, T., Barth, N. C., Khajavi, N., & De Pascale, G. P. (2014). Developing sub 5-m LiDAR DEMs for forested sections of the Alpine and Hope faults, South Island, New Zealand: Implications for structural interpretations. Journal of Structural Geology, 64, 53-66.

Li, Q., Ural, S., Anderson, J., & Shan, J. (2014, July). Minimum description length constrained LiDAR waveform decomposition. In Geoscience and Remote Sensing Symposium (IGARSS), 2014 IEEE International (pp. 165-168). IEEE.

Li, Q., Degnan, J., Barrett, T., & Shan, J. (2016). First evaluation on single photon-sensitive lidar data. Photogramm. Eng. Remote Sens, 82, 455-463.

Li, Q., Ural, S., Anderson, J., & Shan, J. (2016). A Fuzzy Mean-Shift Approach to Lidar Waveform Decomposition. IEEE Transactions on Geoscience and Remote Sensing, 54(12), 7112-7121.

Lin, Z., Kaneda, H., Mukoyama, S., Asada, N., & Chiba, T. (2013). Detection of subtle tectonicgeomorphic features in densely forested mountains by very high-resolution airborne LiDAR survey. Geomorphology, 182, 104-115.

Liu, X. (2008). Airborne LiDAR for DEM generation: some critical issues. Progress in Physical Geography, 32(1), 31-49.

Mallet, C., & Bretar, F. (2009). Full-waveform topographic lidar: State-of-the-art. ISPRS Journal of photogrammetry and remote sensing, 64(1), 1-16.

Mallet, C., Lafarge, F., Roux, M., Soergel, U., Bretar, F., & Heipke, C. (2010). A marked point process for modeling lidar waveforms. IEEE Transactions on Image Processing, 19(12), 3204-3221.

Meng, X., Currit, N., & Zhao, K. (2010). Ground filtering algorithms for airborne LiDAR data: A review of critical issues. Remote Sensing, 2(3), 833-860.

Milonni, Peter W., & Eberly, Joseph H. (2010). Laser Physics, John Wiley & Sons, Inc.

Montes-Hugo, M. A., Bailly, J. S., Baghdadi, N., & Bouhdaoui, A. (2014, July). Modeling the effects of surface and bottom geometries on LiDAR bathymetric waveforms. In Geoscience and Remote Sensing Symposium (IGARSS), 2014 IEEE International (pp. 2706-2708). IEEE.

Mücke, W., Deák, B., Schroiff, A., Hollaus, M., & Pfeifer, N. (2013). Detection of fallen trees in forested areas using small footprint airborne laser scanning data. Canadian Journal of Remote Sensing, 39(sup1), S32-S40.

Mücke, W., Hollaus, M., Pfeifer, N., Schroiff, A., & Deàk, B. (2013). Comparison of discrete and full-waveform ALS features for dead wood detection. ISPRS Ann. Photogramm. Remote Sens. Spat. Inform. Sci, 11-13.

Page-Jones, P.M. (2003). Notes on the RSGB Observations of the HF Ambient Noise Floor, Radio Society of Great Britain. (http://rsgb.org/main/files/2012/12/ EMC_RSGB_HF_Ambient_Noise_Floor_2003.pdf)

Pan, Z., Glennie, C., Hartzell, P., Fernandez-Diaz, J. C., Legleiter, C., & Overstreet, B. (2015). Performance assessment of high resolution airborne full waveform LiDAR for shallow river bathymetry. Remote Sensing, 7(5), 5133-5159.

Parrish, C. E., & Nowak, R. D. (2009). Improved approach to lidar airport obstruction surveying using full-waveform data. Journal of Surveying Engineering, 135(2), 72-82.

Parrish, C. E., Jeong, I., Nowak, R. D., & Smith, R. B. (2011). Empirical comparison of full-waveform lidar algorithms. Photogrammetric Engineering & Remote Sensing, 77(8), 825-838.

Parrish, C. E., Rogers, J. N., & Calder, B. R. (2014). Assessment of waveform features for lidar uncertainty modeling in a coastal salt marsh environment. IEEE Geoscience and Remote Sensing Letters, 11(2), 569-573.

Pirotti, F. (2011). Analysis of full-waveform LiDAR data for forestry applications: a review of investigations and methods. iForest-Biogeosciences and Forestry, 4(3), 100.

Pirottia, F., Guarnieria, A., & Vettorea, A. (2012). Waveform Analysis for the Extraction of Post-Fire Vegetation Characteristics. ISPRS-International Archives of the Photogrammetry, Remote Sensing and Spatial Information Sciences, 523-527.

Popescu, S. C., Zhao, K., Neuenschwander, A., & Lin, C. (2011). Satellite lidar vs. small footprint airborne lidar: Comparing the accuracy of aboveground biomass estimates and forest structure metrics at footprint level. Remote Sensing of Environment, 115(11), 2786-2797.

Qin, Y., Yao, W., Vu, T. T., Li, S., Niu, Z., & Ban, Y. (2015). Characterizing radiometric attributes of point cloud using a normalized reflective factor derived from small footprint LiDAR waveform. IEEE J. Sel. Top. Appl. Earth Obs. Remote Sens., 8(2), 740-749.

Reitberger, J., Schnrr, C., Krzystek, P., & Stilla, U. (2009). 3D segmentation of single trees exploiting full waveform LIDAR data. ISPRS Journal of Photogrammetry and Remote Sensing, 64(6), 561-574.

Rentsch, M., & Krzystek, P. (2012). Lidar strip adjustment with automatically reconstructed roof shapes. The Photogrammetric Record, 27(139), 272-292.

Rieger, P., & Ullrich, A. (2011, October). Resolving range ambiguities in high-repetition rate airborne lidar applications. In Electro-Optical Remote Sensing, Photonic Technologies, and Applications V (Vol. 8186, p. 81860A). International Society for Optics and Photonics.

Rieger, P. (2014). Range ambiguity resolution technique applying pulse-position modulation in time-of-flight scanning lidar applications. Optical engineering, 53(6), 061614.

Rissanen, J. (1983). A universal prior for integers and estimation by minimum description length. The Annals of statistics, 416-431.

Schwarz, G. (1978). Estimating the dimension of a model. The annals of statistics, 6(2), 461-464.

Shan, J., & Toth, C. (2018). Topographic Laser Ranging and Scanning: Principles and Processing, 2nd Edition. CRC Press.

Shanno, D. F. (1970). Conditioning of quasi-Newton methods for function minimization. Mathematics of computation, 24(111), 647-656.

Sheather, S. J., & Jones, M. C. (1991). A reliable data-based bandwidth selection method for kernel density estimation. Journal of the Royal Statistical Society. Series B (Methodological), 683-690.

Shen, X., Li, Q. Q., Wu, G., & Zhu, J. (2017). Decomposition of LiDAR waveforms by B-spline-based modeling. ISPRS Journal of Photogrammetry and Remote Sensing, 128, 182-191.

Shi, J., & Malik, J. (2000). Normalized cuts and image segmentation. IEEE Transactions on pattern analysis and machine intelligence, 22(8), 888-905.

Sitar, M. (2015). Lidar Technology Breakthrough Yields 25% Increase in Collection Efficiency. LiDAR News eMagazine, Vol5, No4.

Skaloud, J., & Lichti, D. (2006). Rigorous approach to bore-sight self-calibration in airborne laser scanning. ISPRS journal of photogrammetry and remote sensing, 61(1), 47-59.

Słota, M. (2014). Advanced processing techniques and Classification of full-waveform airborne laser scanning data. Geomatics and Environmental Engineering, 8.

Stoker, J. M., Abdullah, Q. A., Nayegandhi, A., & Winehouse, J. (2016). Evaluation of single photon and Geiger mode Lidar for the 3D Elevation Program. Remote Sensing, 8(9), 767.

Sumnall, M. J., Hill, R. A., & Hinsley, S. A. (2016). Comparison of small-footprint discrete return and full waveform airborne LiDAR data for estimating multiple forest variables. Remote sensing of environment, 173, 214-223.

Tran, G., Nguyen, D., Milenkovic, M., & Pfeifer, N. (2015). Potential of full waveform airborne laser scanning data for urban area classification-Transfer of classification approaches between missions. The International Archives of Photogrammetry, Remote Sensing and Spatial Information Sciences, 40(7), 1317.

Vallet, J., & Skaloud, J. (2004). Development and experiences with a fully-digital handheld mapping system operated from a helicopter. International Archives of the Photogrammetry, Remote Sensing and Spatial Information Sciences, 35, 1-6.

Vlassis, N., & Likas, A. (2002). A greedy EM algorithm for Gaussian mixture learning. Neural processing letters, 15(1), 77-87.

Wagner, W., Ullrich, A., Ducic, V., Melzer, T., & Studnicka, N. (2006). Gaussian decomposition and calibration of a novel small-footprint full-waveform digitising airborne laser scanner. ISPRS journal of Photogrammetry and Remote Sensing, 60(2), 100-112.

Wagner, W., Roncat, A., Melzer, T., & Ullrich, A. (2007). Waveform analysis techniques in airborne laser scanning. International Archives of Photogrammetry and Remote Sensing, 36(3), 413-418.

Wang, B., Song, S., Gong, W., Chen, Z., Lin, X., Cheng, X., Li, F., & Shi, S. (2017). Optimization Decomposition Method of Full-waveform LiDAR. Acta Geodaetica et Cartographica Sinica, 46(11), 1859-1867.

Wang, C. K. (2012). Exploring weak and overlapped returns of a lidar waveform with a wavelet-based echo detector. Int. Arch. Photogramm. Remote Sens. Spatial Inf. Sci, 39, B7.

Wang, C., Tang, F., Li, L., Li, G., Cheng, F., & Xi, X. (2013). Wavelet analysis for ICESat/GLAS waveform decomposition and its application in average tree height estimation. IEEE Geoscience and Remote Sensing Letters, 10(1), 115-119.

Wang, C., Li, Q., Liu, Y., Wu, G., Liu, P., & Ding, X. (2015). A comparison of waveform processing algorithms for single-wavelength LiDAR bathymetry. ISPRS Journal of Photogrammetry and Remote Sensing, 101, 22-35.

Wehr, A., & Lohr, U. (1999). Airborne laser scanningan introduction and overview. ISPRS Journal of photogrammetry and remote sensing, 54(2-3), 68-82.

Wu, J., Van Aardt, J. A. N., & Asner, G. P. (2011). A comparison of signal deconvolution algorithms based on small-footprint LiDAR waveform simulation. IEEE Transactions on Geoscience and Remote Sensing, 49(6), 2402-2414.

Xu, F., Li, F., & Wang, Y. (2016). Modified LevenbergMarquardt-Based Optimization Method for LiDAR Waveform Decomposition. IEEE Geoscience and Remote Sensing Letters, 13(4), 530-534.

Zhao, X., Zhao, J., Zhang, H., & Zhou, F. (2018). Remote Sensing of Suspended Sediment Concentrations Based on the Waveform Decomposition of Airborne LiDAR Bathymetry. Remote Sensing, 10(2), 247.

Zhou, T., & Popescu, S. C. (2017). Bayesian decomposition of full waveform LiDAR data with uncertainty analysis. Remote Sensing of Environment, 200, 43-62.

Zhou, T., Popescu, S. C., Krause, K., Sheridan, R. D., & Putman, E. (2017). GoldA novel deconvolution algorithm with optimization for waveform LiDAR processing. ISPRS Journal of Photogrammetry and Remote Sensing, 129, 131-150.

VITA

VITA

Qinghua Li

Graduate School, Purdue University

Qinghua Li is a dual-degree graduate student at the Lyles School of Civil Engineering and the School of Electrical and Computer Engineering, Purdue University. Before entering Purdue University, Qinghua Li worked and studied at the Department of Electronic Engineering of City University of Hong Kong and The Chinese University of Hong Kong. Qinghua Li received M.S. and B.S. degrees from the School of Electronic Engineering, Xidian University, China.

Academic Experience at Purdue University

- 2018, Research Assistant, Center on Religion and Chinese Society

  - Working on Mapping Chinese Spiritual Capital and conducting big data analysis on social media of Weibo.

  - Independent development of Qpyder, a Python crawler that automatically downloads data from Weibo.

  - Independent development of MapMaker, a python package that automatically generates large volume of high-quality maps.

- 2018, 2016, Research Volunteer, Civil Engineering

  - Evaluation of an adaptive terrestrial laser scanner. A paper was submitted to the *Remote Sensing* (first author).

  - Comparative study on a single photon-sensitive lidar. A paper was published on *Photogrammetric Engineering and Remote Sensing (PE&RS)*.

- 2017, Hourly Student Assistant, Civil Engineering

  - Working on the CORE3D (Creation of Operationally Realistic 3D Environment) project sponsored by the Intelligence Advanced Research Projects Activity (IARPA). Developed a hybrid algorithm for building extraction.

- 2015-2017, Research Assistant, Purdue Libraries

  - Interdisciplinary study on water sustainability. Data mining with geo-tagged tweets. Data visualization. The work was presented in the SWAAG-AAG (Applied Geography Conference) joint meeting in 2015 and published in 2016.

  - Topic modeling and visualization on GIS-related papers in Scopus database. A hieratical LDA was developed in this work.

- 2012-2014, Research Assistant, Civil Engineering

  - PhD project funded by the U.S. Army Research Office.

  - The work on waveform decomposition was published on *IEEE Transactions on Geoscience and Remote Sensing* (first author).

  - The work on self-calibration was presented in the Imaging & Geospatial Technology Forum (IGTF, ASPRS annual conference), 2017.

Courses Attended

AAE590	Remote Sensing System Design II
CE597	Digital Photogrammetric Systems
CE597	GPS Positioning
CE597	Hyperspectral remote sensing
CE597	Geographic Information Systems
CE597	Multi- and Hyperspectral Remote Sensing
CE697	SAR Interferometry
CS530	Introduction to Scientific visualization
CS573	Data Mining
CS578	Statistical Machine Learning

CS580	Algorithm Design Analysis and Implementation
CS662	Pattern Recognition and Decision Making Processes
CS690	Deep Learning *
EAS657	Geophysical Inverse Theory
ECON610	Game Theory *
ECON671	Econometrics I *
ECON672	Econometrics II *
ECON673	Time Series Econometrics *
ECON674	Microeconometrics *
ECON690	Theory Bayesian Econometrics *
ECON690	Applied Bayesian Econometrics *
ECE538	Digital Signal Processing I
ECE552	Introduction To Lasers
ECE600	Random Variables and Signals
ECE641	Digital Image Processing II
MA511	Linear Algebra with Applications
STAT529	Applied Bayesian Decision Theory *
STAT532	Elements of Stochastic Processes
STAT598	Introduction To Computational Statistics
BUS36902	Dynamic Programming/Markov Decision Processes * †
BUS37904	Advanced Quantitative Marketing * †
GSB41913	Bayesian Econometrics * †

---

*Attended without registration

†Attended at University of Chicago

PUBLICATIONS

PUBLICATIONS

Lidar Remote Sensing:

Li, Q., Ural, S., & Shan, J. (2018, August). A Comparative Study on Airborne Lidar Waveform Decomposition Methods. In 2018 10th IAPR Workshop on Pattern Recognition in Remote Sensing (PRRS) (pp. 1-6). IEEE.

Li, Q., Ural, S., Anderson, J., & Shan, J. (2016). A Fuzzy Mean-Shift Approach to Lidar Waveform Decomposition. IEEE Transactions on Geoscience and Remote Sensing, 54(12), 7112-7121.

Li, Q., Degnan, J., Barrett, T., & Shan, J. (2016). First evaluation on single photon-sensitive lidar data. Photogramm. Eng. Remote Sens, 82, 455-463.

Li, Q., Ural, S., & Shan, J. (2016, July). Decomposing LiDAR waveforms with nonparametric classification methods. In Geoscience and Remote Sensing Symposium (IGARSS), 2016 IEEE International (pp. 5573-5576). IEEE.

Li, Q., Ural, S., Anderson, J., & Shan, J. (2014, July). Minimum description length constrained LiDAR waveform decomposition. In Geoscience and Remote Sensing Symposium (IGARSS), 2014 IEEE International (pp. 165-168). IEEE.

Social Media Data Mining:

Li, Y., **Li, Q.**, & Shan, J. (2017). Discover patterns and mobility of Twitter usersA study of four US college cities. ISPRS International Journal of Geo-Information, 6(2), 42.

Kong, N., **Li, Q.**, Sangwan, N., Kulzick, R., Matei, S., & Ariyur, K. (2016). An Interdisciplinary Approach for a Water Sustainability Study. Papers in Applied Geography, 2(2), 189-200.